2013

Simulation based characterization and performance enhancement of heterogeneous polymer solar cells

Hari Krishna Kodali
Iowa State University

Simulation based characterization and performance enhancement of heterogeneous polymer solar cells

by

Hari Krishna Kodali

A dissertation submitted to the graduate faculty

in partial fulfillment of the requirements for the degree of

DOCTOR OF PHILOSOPHY

Major: Mechanical Engineering

Program of Study Committee:

Baskar Ganapathysubramanian, Major Professor

Sumit Chaudhary

Valery Levitas

Shankar Subramaniam

Jue Yan

Iowa State University

Ames, Iowa

2013

TABLE OF CONTENTS

LIST OF TABLES

LIST OF FIGURES

ACKNOWLEDGEMENTS

I would like to take this opportunity to express my thanks to those who helped me with various aspects of conducting research and the writing of the journal papers included in this thesis. First and foremost, Dr. Baskar Ganapathysubramanian for his guidance, patience and support throughout this research and the writing of papers for publication. His enthusiasm, insights and words of encouragement have often inspired me and renewed my hopes for completing my graduate education. I would also like to thank Dr. Sumit Chaudhary for his efforts, contributions and discussions in our collaborative research work. I would additionally like to thank Dr. Olga Wodo for her patience and many hours of fruitful discussions which helped immensely with my research.

CHAPTER 1. GENERAL INTRODUCTION

1.1 Introduction

Dwindling reserves of conventional energy sources – like crude oil and coal – have been a major source of international conflict in past few decades. In addition, large-scale pollution and subsequent climate change is a prominent cause of deterioration of human health and loss of infrastructure in many countries. Moreover, recent disasters due to leakage from nuclear power plants in Japan has prompted some countries to phase out nuclear power. This has indeed increased the importance of nonrenewable energy sources like solar, wind, hydropower and biothermal and according to International Energy Agency, these energy sources are likely to overtake natural gas as second largest power source by the year 2016 [8].

Solar radiation is a hugely under utilized source of energy. Photovoltaics based on inorganic material like silicon and germanium have made great strides in tapping this source of energy by direct conversion of radiation to electricity. But there high manufacturing cost have not allowed replacement of conventional energy sources for large scale power generation. Organic solar cells based on blend of electron donating conjugate polymers and electron accepting fullerene materials have potential to be a *disruptive technology* within the solar cell market. This is due to the numerous advantages of organic solar cells over their inorganic counterparts, like, mechanical flexibility and low weight, large-area fabrication using roll-to-roll processing at low temperatures, compatibility with flexible substrates, high optical absorption, easy tunability by chemical doping, semitransparency and low environmental impact during manufacturing and operations.

Issues like low power conversion efficiency and durability still prevent commercial success of organic polymer based photovoltaic devices. The problem of low power conversion efficiency

is examined in this thesis.

There are various approaches taken by the research community for improvement of efficiency of organic photovoltaics. **(1)** Development of new donor and acceptor materials which to lower band gap and hence increased photon absorption. Materials with higher charge mobilities would also result in increased performance. **(2)** Topology improvement for light entrapment using V-shaped panel arrangement or textured substrate platform to increased photon absorption due to multiple passes. **(3)** Electrode surface patterning to again increase photon absorption and charge collection. **(4)** Morphology improvement to increase charge generation and transport

The focus of this thesis on computational investigation of the strategy to OSC performance enhancement through morphology improvement. A computational approach has the advantage of efficient and parallel interrogation of large number of morphologies by capturing the physics of charge generation and transport in OSCs. Although OSC simulation using continuum models based on excitonic drift-diffusion equations for heterogeneous microstructure have been considered earlier [9, 10, 11, 12, 13], we develop an efficient and scalable framework for simulation of OSC device physics equations in dimensionally independent manner and fulfilling the objectives stated as research objectives in the next section.

1.2 Summary of research objectives

(1) Computational framework is able to use images of realistic morphologies obtained from TEM, SEM or AFM measurements.

(2) Able to visualize the distribution of exciton densities, charge densities, potential and current densities in three dimensional heterogeneous morphology.

(3) Able to differentiate devices based on performance with different morphologies.

(4) Quantify the sensitivity of final electrode current density to material properties (electron/hole mobility, dielectric constant), device thickness and illumination intensity for (a) Bulk-heterojunction, (b) Sawtooth, and (c) Bilayer morphologies.

(5) Investigate if a device with sawtooth morphology is optimum of high efficiency.

(6) Able to provide numerical support to experimental investigation of (1) Effect of OSC spin-casting based fabrication spin rate on recombination due to additional trap levels [14] and (2) Effect of ferroelectric dipoles on charge separation in OSC [15].

1.3 Thesis Organization

This thesis is organized into six chapters. First chapter is for general introduction and last chapter lists general conclusions. Rest of the chapters – chapter two to five – comprise of three published and one preprint journal papers with one chapter for each paper.

CHAPTER 2. A COMPUTATIONAL FRAMEWORK TO INVESTIGATE CHARGE TRANSPORT IN HETEROGENEOUS ORGANIC PHOTOVOLTAIC DEVICES

A paper published in *Computer Methods in Applied Mechanics and Engineering*

Hari K. Kodali and Baskar Ganapathysubramanian

Abstract

Low cost per watt and mechanical flexibility of organic solar cells (OSC) make it a promising alternative to traditional inorganic solar cells. Recently, conjugated polymer based organic solar cells with efficiency of 8.13% [16] have been reported. Experimental results suggest that the distribution of the donor and acceptor constituents in the morphology is a key factor in determining the efficiency of such devices. A computational framework that can effectively explore that correlation between morphology and performance would greatly accelerate the development of high efficiency organic photovoltaic devices.

In this paper, we develop a scalable computational framework to understand the correlation between nanoscale morphology and performance of OSC. We focus on the *charge transport mechanism* while considering one-stage interfacial charge generation process. Steady state drift-diffusion equations are used for modeling these devices. We discuss the numerical challenges associated with a finite element based simulation of OSC with spatial variation in material properties and large charge density gradients. The effect of microstructure on the distribution of charge densities and electrostatic potential is investigated. The prominent effect of feature size and interface area on the current-voltage characteristics is illustrated using realistic microstructures. We showcase the framework by interrogating fully 3D heterogeneous

microstructures.

2.1 Introduction

Dwindling resources, climate change and accidents leading to large-scale pollution with conventional energy sources have made clean and renewable energy sources all the more relevant. Solar radiation is an abundant and largely under utilized source of energy. Solar cells based on inorganic materials like silicon and germanium have made great strides in tapping this energy, but their inherently high manufacturing cost render this form of energy prohibitive for widespread use. The possibility of flexible, large-area fabrication makes conjugated polymer based organic solar cell (OSC) devices highly attractive for ubiquitous solar-electric conversion [17]. OSC technology incorporates the advantages of facile fabrication suitable for roll-to-roll processing, compatibility with flexible substrates, high optical absorption, low-temperature processing, and easy tunability by chemical doping [18]. Additionally, the optical properties of polymer films are relatively tolerant to defects in the bulk, making them suitable for rapid deployment and large area applications. These properties - flexibility, rapid production, biodegradability - make organic solar cells a power source of great promise. This versatility enables organic solar cells to be used on a large scale like walls of buildings, transparent window panels, automobile exteriors, or with small everyday use objects like garments, umbrellas, and handbags [19].

Solvent-based thin-film deposition technologies [20] (e.g. spin coating, drop casting, doctor blading) are the most common organic photovoltaic fabrication techniques. These techniques usually involve preparing dilute solutions of electron-donor polymers (like P3HT, poly(3-hexylthiophene)) and electron-accepting polymers (like PCBM, [6,6]-phenyl-C61 butyric acid methyl ester) in a volatile solvent. After some form of coating onto a substrate, the solvent evaporates, leaving a system consisting of only two components. An initially homogeneous mixture subsequently undergoes spinodal decomposition and separates into electron-acceptor rich regions and electron-donor rich regions [21]. Depending on the specifics of polymer blend and processing conditions (spin coating time [22, 23] , annealing time [24, 25] , solvent type [26, 27]), different morphologies are typically formed (Figure. 2.1).

Figure 2.1: Cross-sectional morphology for rrP3HT:PCBM system imaged using TEM[6]. Dimensions are 1200nm×100nm. The white regions represent the photo active polymer (rrP3HT), while the black regions represent the conducting fullerene (PCBM).

This is in contrast to inorganic solar cells (ISC) which are made by sandwiching together an electron rich (n-type) material and hole rich (p-type) material which require expensive manufacturing techniques like vacuum deposition. Unlike ISC which have a bilayer structure and hence only one interface for free charge creation, OSC has a plethora of inter penetrating donor-acceptor interfaces, the so-called Bulk-Heterojunction (BHJ). This structure results in high optical absorption [28] .

The past decade has witnessed considerable improvement in efficiencies in organic solar cells (from efficiencies below 3% [29] to currently the highest reported efficiency 8.13% [16] obtained in laboratory conditions). This improvement was made possible primarily through new materials development [30, 31, 32], and device designs [33, 34, 35]. Recent experimental evidence suggests that tailoring the morphology of the thin film will have significant effect on the final performance of the device [36, 26, 37, 38]. In particular, efficiency gains have been obtained by affecting the microstructure using additives [39, 40], annealing [28] at a temperature above the glass transition of the polymer and by making use of solvents with higher boiling point [29] during processing. There is a lot of room for progress to standardize a process of morphology improvement in terms of optimizing the spatial arrangement of the constituents. Experimentally determining and rank ordering two different morphologies – resulting from different processing parameters – is expensive. A computational framework which can *efficiently interrogate the microstructure by capturing the physics of charge generation and transport in organic solar cells* would be immensely helpful in understanding the effect of morphology on performance. This is the pressing motivation for the current work.

The physics of current generation in OSC can be divided into two stages. **Stage 1 - Charge Generation**: Absorption of light resulting in generation and subsequent diffusion of tightly

coupled electron-hole pairs known as excitons towards donor-acceptor interface. These excitons then separate at the interface to form electrons in the acceptor region and holes in the donor region.

Stage 2 - Charge Transport: Movement of electrons and holes towards the cathode and anode respectively. The tortuous structure of the pathways (see Figure. 2.1) makes transport of the generated charges towards the electrodes a complex process.

This work focuses on quantifying the effect of morphology on charge transport, i.e. Stage 2 detailed above. We utilize a charge transport model (based on the drift-diffusion equations [41]) capable of distinguishing between the properties of devices with different morphologies. This is achieved by using spatially varying material properties according to the composition of the blend at each point and by limiting the generation (i.e. Stage 1) and recombination process to a thin region around the donor-acceptor interface. The computational efficiency of this model allows us to perform large scale simulations in a high throughput fashion[1]. Other contributions of the present study include the following:

(1) Using realistic morphologies obtained from TEM, SEM or AFM measurements to extract morphological information in contrast to the regular morphologies studied previously [10, 11, 12, 13]; **(2)** the first three dimensional analysis of charge transport in heterogeneous realistic microstructure. **(3)** formulation of an accurate current-calculation strategy based on transformation of the charge densities to fermi-level variables; **(4)** implementing a parallel, scalable framework that enables scalable analysis of large scale devices; **(5)** deploying the framework using a modular structure that makes it easier to incorporate new mobility, generation and recombination models; and **(6)** we showcase results which illustrate the effects of realistic morphologies on the distribution of charge densities, potential and current density distributions. Comparative analysis across morphologies having different features further emphasize the role of morphology on charge transport and device performance.

[1]There are equations that model Stage 1 [9, 10, 11, 12, 13] (i.e the exciton generation and diffusion process), in addition to the charge transport equations in the drift-diffusion model. These sets of equations have been used to provide valuable insight into the two stage process for simple morphologies. We focus our attention on computationally solving Stage 2 for complex heterogeneous microstructures. A framework for solving the coupled Stage 1 and Stage 2 system is presented in a forthcoming publication. [42]

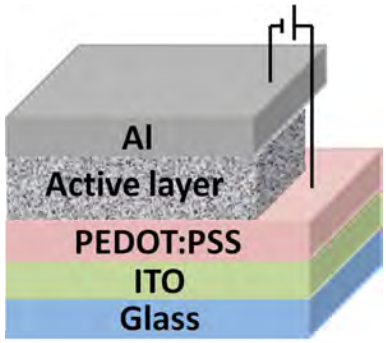

Figure 2.2: Schematic of the cross-section of a typical organic solar cell device along the thickness.

2.2 Problem definition

2.2.1 Device morphology

The physical domain of interest is the active layer of an organic solar cell (Figure. 3.2). The active layer is a thin layer comprising of an electron donating conjugated polymer and an electron accepting fullerene-derivative. Figure. 2.1 shows a typical structure of the active layer as observed under transmission electron microscope by Moon et al [6]. White region denotes Regio-regular poly(3-hexylthiophene) (rrP3HT or polymer) and black region is [6,6]-phenyl-C61 butyric acid methyl ester (PCBM or fullerene). The top and bottom boundaries are connected to electrodes to extract current. One of the electrodes is transparent to the visible region of electromagnetic radiation spectrum, while the other is reflecting. Often, Indium Tin Oxide (ITO) covered with a conducting polymer like poly(3,4-ethylenedioxythiophene): poly(styrenesulfonate) (PEDOT:PSS) is used as transparent anode and Aluminum as reflecting cathode.

2.2.2 Device Physics: Stage 1 and Stage 2

Stage 1: The radiation reaching the active layer through the transparent electrode is absorbed by the electron donating polymer. The absorption of photons leads to formation of tightly bound electron-hole pairs known as excitons [28] (Figure. 3.3(A)). The excitons need

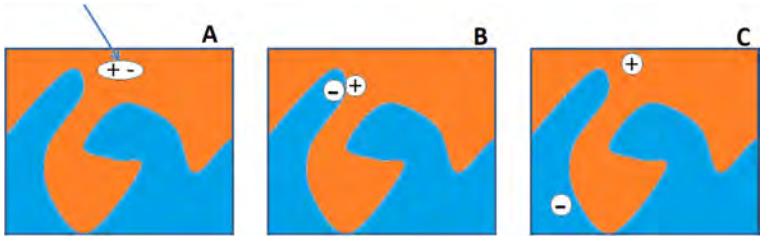

Figure 2.3: Device operation. A. Photon absorption/exciton generation. B. Exciton diffusion and polaron formation. C. Polaron dissociation and free charge creation

to diffuse through the donor to reach the donor-acceptor interface before decaying (lifetime of $\sim$ 0.5 nanoseconds [43]). At the interface, [44] the excitons dissociate into free electrons and holes. As shown in Figure. 3.3(B), the dissociation of excitons involves transfer of electrons to the acceptor at the donor-acceptor interface.

Stage 2: Electron transfer at donor-acceptor interface is followed by transport of electrons and holes towards their respective electrodes. As shown in Figure. 3.3(C), after exciton dissociation the electrons travel through the electron accepting fullerene and the holes through the electron donating polymer.

2.2.3 Device Model for Stage 2

There are two classes of models that can be used to interrogate heterogeneous semiconductor devices (1) Microscopic models, and (2) Continuum models.

Microscopic models based on Monte Carlo simulations [45, 46, 47] can accurately describe the effect of morphology on charge generation, recombination and transport. It is also simple to incorporate new physics (like quantum effects) with Monte Carlo methods. They have been used with great utility in understanding the effects of various sub-processes in semiconductor analysis [48, 49]. However, these methods have some drawbacks. Specifically, these methods are computationally very expensive to use for three dimensional simulations and high throughput analysis (for morphology characterization). Furthermore, long range nature of coulomb interaction limits the use of Monte Carlo simulations [12] for full device scales.

On the other hand, continuum models based on the classical drift-diffusion equations, pro-

vide a computationally efficient alternative to microscopic models. Continuum models can also incorporate recombination, exciton generation and creation of free charges, which are unique to OSC device operation (though not as easily as into Monte Carlo based models). Continuum models with heterogeneous microstucture have been considered by Barker et al. [9], Buxton and Clarke [10], Martin et al. [11], Williams et al. [12] and Ganesan et al. [13]. The drift-diffusion model is derived from the Boltzmann transport equation by replacing actual carrier distribution function with equilibrium distribution function assuming the charge carrier temperature to be constant throughout the device [50][2].

The effect of morphology of the active layer of an organic solar cell device is incorporated into the drift-diffusion model by using spatially varying material properties based on the spatial distribution of constituent materials. These properties (charge carrier mobilities and dielectric constant) effect the transport of charges through the active layer. A simple charge generation model (for Stage 1) is used [3].

The equations describing the charge transport processes in a heterogeneous organic solar cell are given below. The three fields of interest are the electron density n, hole density p and the electrostatic potential ϕ.

$$\nabla \cdot (\epsilon \nabla \phi) = q(n - p) \tag{2.1}$$

$$\nabla \cdot \mathbf{J_n} = qU \tag{2.2}$$

$$\nabla \cdot \mathbf{J_p} = -qU \tag{2.3}$$

$$\mathbf{J_n} = -qn\mu_n \nabla \phi + qD_n \nabla n \tag{2.4}$$

$$\mathbf{J_p} = -qp\mu_p \nabla \phi - qD_p \nabla p \tag{2.5}$$

where Eq. 2.1 describes the effect of space charges on the electrostatic potential ϕ in the

[2]This model breaks down under high electric field and when the device dimension (distance between the electrodes) is short compared to the carrier mean-free path ($\sim$ 5-8 nm for P3HT [43]). Carriers accelerate under high electric field, and scattering is not sufficiently strong to bring the carrier temperature back to lattice temperature. A short high-field region causes the distribution function to become highly asymmetric which cannot be approximated by equilibrium distribution function. Typical thickness of the active layer of an OSC device is around 100 nm, which is much larger than the carrier mean-free path. The range of interest for the externally applied potential, in order to characterize the device, is from zero volts to the open circuit voltage. Thus, the device dimensions and operating conditions for OSC devices permit the use of drift-diffusion model.

[3] The charge generation and recombination is confined to a thin region of thickness 2δ around the donor-acceptor interface. The value of δ is taken as 10 nm, which is the approximate value of exciton dissociation length [41]

device. Eqs. (2.2), (2.3) are known as the current continuity equations. $\mathbf{J_n}$ and $\mathbf{J_p}$ are the current densities for electrons and holes respectively. The electric field dependence of charge carrier mobilities μ_i ($i = n$ or p) is taken into account by using the Frenkel-Poole form $\mu_i = \mu_{i0} \exp(E/E_{i0})$ [51] , where μ_{i0} are the zero field mobilities and E_{i0} the Frenkel-Poole field parameter for electron and holes respectively. The carrier diffusion coefficients D_i are assumed to obey the Einstein relation [52] $D_i = \mu_i V_t$, where the thermal voltage $V_t = k_B T/q$, k_B is the Boltzmann constant and T the temperature. q denotes elementary charge and U is the net generation rate given by

$$U = -PG + (1 - P)R \tag{2.6}$$
$$R = \gamma(np - n_{int}^2)$$

where P is the probability of electron-hole pair dissociation. The generation rate of electron-hole pairs is denoted by G and their recombination rate by R which is dependent on charge densities of electron n and holes p. γ is the recombination strength which is discussed Appendix A. n_{int} is the intrinsic carrier density of electrons and holes given by $n_{int} = \sqrt{N_C N_V} exp(-E_{gap}/2V_t)$. $N_{C|V}$ denotes the effective density of states of conduction and valence band. E_{gap} is the band gap.

Remark 1: Divergence of total current J Adding Eqns. 2.2 and 2.3 gives $\nabla \cdot (\mathbf{J_n} + \mathbf{J_p})$=0, or $\nabla \cdot \mathbf{J}$=0, where $\mathbf{J}$ denotes total current. Hence the divergence of the total current at any location in the domain has to be zero. This condition is not imposed explicitly. *It is an emergent property which is used to check the validity of the numerical solution.*

Boundary conditions One of the electrodes is assumed to line up with the conduction band and the other with the valence band. Hence, for these Ohmic boundaries[53, 54], the boundary conditions for the charge densities is given by

$$n(C) = N_C$$
$$p(C) = N_V exp(\frac{-E_{gap}}{V_t}) \tag{2.7}$$

for the electrode lined up with conduction band and

$$n(V) = N_C exp(\frac{-E_{gap}}{V_t})$$
$$p(V) = N_V \tag{2.8}$$

for the electrode aligned with valence band. The built-in potential V_{bi} is given by the difference in the work functions of the two electrodes, given by $qV_{bi} = \varphi_{an} - \varphi_{cat}$, where φ_{an} and φ_{cat} are the work functions for the anode and the cathode. As the electrodes are assumed to line up with the conduction and valence bands, i.e. the LUMO of acceptor and HOMO of donor respectively, $V_{bi} = E_{gap}$. Hence, the electrostatic potential at the electrodes is given by

$$\phi_C - \phi_V = E_{gap} - V_a \tag{2.9}$$

where V_a is the applied voltage.

Remark 2: Current-Voltage plot The electron and hole current density vectors (equations 2.4 and 2.5) are calculated using the values of n, p and ϕ obtained by solving the drift-diffusion equations (2.1-2.3). The integral of the normal component of $\mathbf{J_n}$,$\mathbf{J_p}$ at the electrodes is computed to obtain the average current density available from the device. The current density depends on the boundary condition for potential calculated from the applied voltage. The values of current density obtained for a range of applied voltages – from zero volts to open circuit voltage – is plotted. This current-voltage plot is finally used to characterize the device by calculating the fill-factor and power conversion efficiency. Fill-factor is obtained by taking the ratio of maximum power and the product of short-circuit current and open-circuit voltage.

Remark 3: The boundary conditions as well as the charge recombination model are modularly implemented. This allows subsequent changes to investigate different boundary conditions (Schottky type) and recombination models to be easily made.

2.3 Computational method

This section details the computational approach and challenges in solving Eqns. 2.1-2.3.

2.3.1 Non-dimensionalized equations

It is common practice to use normalized units to avoid numerical overflow/underflow and to make the algorithms more efficient. This is significant in this problem because of approximately 20 orders of magnitude variation in the charge distributions (n, and p), and domain size in nanometers which leads to overflow and underflow errors. Using the scaling strategy of Markowich [55], with the scaling factors given in Table 2.1, the basic equations transform into the following.

$$\hat{\nabla} \cdot (\lambda^2 \hat{\nabla} \hat{\phi}) = (\hat{n} - \hat{p}) \tag{2.10}$$

$$\hat{\nabla} \cdot (-\hat{\mu_n} \hat{n} \hat{\nabla} \hat{\phi} + \hat{\mu_n} \hat{\nabla} \hat{n}) = \hat{U} \tag{2.11}$$

$$\hat{\nabla} \cdot (\hat{\mu_p} \hat{p} \hat{\nabla} \hat{\phi} + \hat{\mu_p} \hat{\nabla} \hat{p}) = \hat{U} \tag{2.12}$$

where the [$\hat{}$] indicates that the variable is scaled. For notational convenience, [$\hat{}$] will be dropped in all further use of these equations. The Debye length λ is

$$\lambda^2 = \frac{\epsilon \phi_0}{x_0^2 q N_C} \tag{2.13}$$

which gives the minimum resolution needed to resolve charge variations in space [52].

Quantity	Scaling factor symbol	Value of scaling factor
x	x_0	Maximum length scale
ϕ	V_t	$\frac{k_B T}{q}$
n,p	N_C	N_C
D_n, D_p	D_0	$\max(D_n, D_p)$
μ_n, μ_p	μ_0	D_0/ϕ_0
U	U_0	$D_0 C_0 / x_0^2$

Table 2.1: Scaling factors used to non-dimensionalize the drift-diffusion equations

Finite element formulation The presence of significant drift(convective) term in the current-continuity equations is handled using Streamline Upwind Petrov Galerkin (SUPG)

formulation [56].

In a spatial domain, Ω, find $\phi, n, p \in H^1(\Omega)$, $\phi = \phi_D$, $n = n_D$, $p = p_D$ on $\partial\Omega_D$ such that

$$\int_\Omega \left(\nabla \cdot (\lambda^2 \nabla\phi) - (n - p)\right) w_\phi d\Omega = 0 \tag{2.14}$$

$$\int_\Omega \left(\nabla \cdot \mathbf{J_n} - U\right) w_n d\Omega = 0 \tag{2.15}$$

$$\int_\Omega \left(\nabla \cdot \mathbf{J_p} - U\right) w_p d\Omega = 0 \tag{2.16}$$

for all $w_\phi, w_n, w_p \in H_0^1(\Omega)$. ϕ_D, n_D and p_D represent the Dirichlet boundary values for the potential ϕ and charge densities n and p, respectively. On the remainder of the domain boundary $\partial\Omega/\partial\Omega_D$, zero flux (Neumann) conditions for $\nabla\phi$, $\mathbf{J_n}$ and $\mathbf{J_p}$ are (implicitly) applied.

This results in a Galerkin form given as: Find ϕ^h, n^h, p^h, satisfying the essential boundary conditions such that

$$\int_\Omega \left(-\lambda^2 \nabla\phi^h \cdot \nabla w_\phi^h - (n^h - p^h) w_\phi^h\right) d\Omega = 0 \tag{2.17}$$

$$\int_\Omega \left(n^h \nabla\phi^h \cdot \nabla w_n^h - \nabla n^h \cdot \nabla w_n^h\right) d\Omega$$

$$-\sum_e \int_{\Omega_e} \left(\nabla \cdot \mathbf{J_n} - U\right) [\tau_n \nabla\phi^h \cdot \nabla w_n^h] d\Omega = \int_\Omega \frac{U}{\mu_n} w_n^h d\Omega \tag{2.18}$$

$$\int_\Omega \left(p^h \nabla\phi^h \cdot \nabla w_p^h + \nabla p^h \cdot \nabla w_p^h\right) d\Omega$$

$$+\sum_e \int_{\Omega_e} \left(\nabla \cdot \mathbf{J_p} - U\right) [\tau_p \nabla\phi^h \cdot \nabla w_p^h] d\Omega = \int_\Omega -\frac{U}{\mu_p} w_p^h d\Omega \tag{2.19}$$

where ϕ^h, n^h and p^h are the Galerkin approximations to the electrostatic potential, electron density and hole density respectively. τ_n and τ_p are the stabilization parameters for the electron and hole continuity equations respectively. These stabilization parameters are given by:

$$\tau_n = \tau_p = \begin{cases} \frac{h^2}{12} & 0 \leq \| \nabla\phi \| h/2 \leq 3 \\ \frac{h}{2\|\nabla\phi\|} & 3 \geq \| \nabla\phi \| h/2 \end{cases} \tag{2.20}$$

Here, h is the 'element length' computed using the expression $h = 2(\sum_{a=1}^{n_{en}} |\mathbf{s} \cdot \nabla N_a^e|)^{-1}$, where n_{en} is the number of nodes in the element, $\mathbf{s}$ is the unit vector in the direction of local velocity and N_a^e is the basis function associated with the local node a. The discretized equations (3.20-3.22) generates a coupled system of non-linear algebraic equations.

Remark 4: Finite element method with SUPG over exponential basis function It is worth noting that drift-diffusion equations have been solved in two dimensions using Scharfetter-Gummel method for both inorganic [52] and organic [10] solar cells with finite difference method. In addition, exponential fitting finite element discretization have been used for simulating organic [57, 58, 59, 60] solar cell devices. Finite element method with exponential basis functions provides a natural extension of the classical Scharfetter-Gummel difference scheme [61, 62]. However, Sharma et. al. [63] argue that a flux-directed numerical dissipation term which is a variant of streamline upwind Petrov-Galerkin class of methods is potentially more accurate than Scharfetter-Gummel method for two or three dimensional simulations.

Remark 5: A note about the boundary conditions Assuming a flat device with top and bottom boundaries in contact with the electrodes, the device lengths in the two horizontal directions much larger than the vertical direction. The top and bottom are Dirichlet boundaries as the values of charge densities and electrostatic potential is specified there. Periodic boundary conditions are used at the other surfaces.

2.3.2 Clustering motivated by an analytical solution to the 1D drift diffusion equation

The 1D drift-diffusion equations with simplifying assumptions can be exactly solved to get analytical results for charge and current densities (refer to appendix A.10 for details). These equations still retain many of the characteristics of the original equations, like large drift component and huge charge density gradients near the electrodes. This analytical result enabled exact error calculation for various numerical schemes and also allowed us to study grid convergence. Analysis revealed that the current density varied very steeply close to the electrodes. This suggested a clustering of mesh points close to the electrode boundaries using

$$y_c = h\frac{(\beta+1)[(\beta+1)/(\beta-1)]^{(2\xi-1)} - \beta + 1}{2\{1 + [(\beta+1)/(\beta-1)^{(2\xi-1)}\}} \tag{2.21}$$

where, $\xi = y/L_y$ and $1 < \beta < \infty$. As β approaches 1, more grid points are clustered near y = 0 and y = 1. Extensive numerical simulations revealed a value of $\beta = 0.002$ to be optimum for

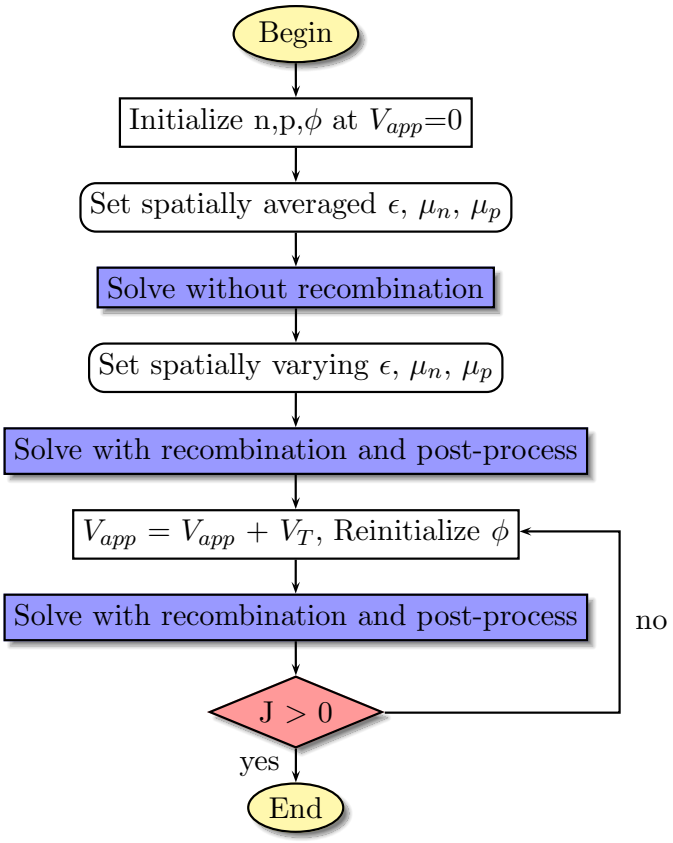

Figure 2.4: Flow diagram of the method of continuation.

the simulations.

2.3.3 Method of continuation

The highly coupled and non-linear nature of the drift-diffusion equations necessitates a good initial guess and subsequent solution strategy for convergence of Newton's method. We utilize a method of continuation involving a series of steps to solve the problem (Figure. 2.4). A 'step' denotes solution of drift-diffusion equations at a specific value of applied voltage.

For the first step, a constant electric field at equilibrium ($V_{app} = 0$) and zero charge densities is used as initial guess. Then the equations are solved for n, p and ϕ neglecting recombination and using spatially averaged material properties (ϵ, μ_n and μ_p) . Subsequently, the effect of morphology is incorporated by using the material properties of the polymer and fullerene

separately, instead of using the spatially averaged values. At the beginning of each step, the initial guess for the electric field is set to a constant value instead of using the solution from preceding step. This enables the Newton's method solver to have a convergence criteria based on relative tolerance. The value of the applied voltage is incremented by V_T at each step to construct the J-vs-V curve. This is continued until the current density (J) at the electrodes becomes negative.

2.3.4 A new formulation for post-processing charge density to compute current density

Post-processing for current from the calculated values of potential and charge densities present a significant challenge. For example, the electron current $\mathbf{J_n} = -q\mu_n \nabla\phi n + qD_n \nabla n$ involves derivatives of the potential and density which cannot be calculated to satisfactory accuracy with first order methods. A second order accurate method for derivative calculation at the boundaries introduced by Carey [63] slightly mitigates this problem but still requires large number of grid points in regions of large density variation. Assuming an exponential variation of densities, as introduced by Scharfetter and Gummel [61], leads to significant reduction in the number of grid points required. But this method is not readily extensible to find the current density vector in two or three dimensions.

We propose a technique wherein, only for the current density calculation, the charge densities are replaced by quasi-Fermi level variables given as

$$\Phi_n = V - V_t \log(n/n_{int}) \tag{2.22}$$
$$\Phi_p = V + V_t \log(p/n_{int})$$

where, $\Phi_{n|p}$ are the electron—hole Fermi level variables. Using these variables the expressions for electron and hole current densities reduce to

$$\mathbf{J_n} = -qn\mu_n \nabla\Phi_n \tag{2.23}$$
$$\mathbf{J_p} = -qp\mu_p \nabla\Phi_p$$

In these expressions, instead of the derivatives of charge densities we have the derivatives of Fermi levels which can be calculated accurately even with first order methods. This is due to

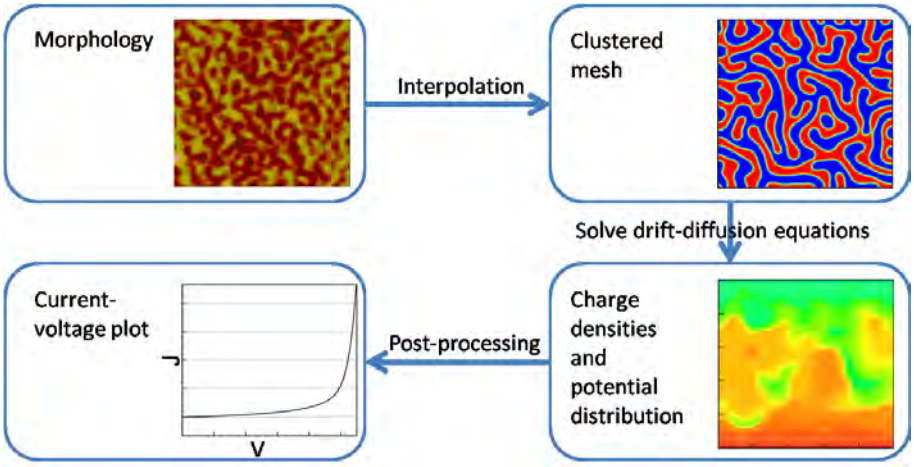

Figure 2.5: Flow chart of the framework

using the logarithm of charge carriers in the expressions for Fermi level variables, which scales down gradients considerably. The derivatives at nodal points of the computational mesh are obtained by using least-squared interpolation of the derivative values at the integration points.

The values of current density obtained at electrode boundaries may vary across the boundary, based on the distribution of the constituents. Hence, the current densities are integrated over the electrode boundary surface and the resultant value is divided by the area of the surface. This gives the average current across the electrodes.

2.3.5 The computational framework

Figure. 2.5 gives an overview of the key steps involved in the framework. Given microstructural description of the device, the morphological details are interpolated onto a computational mesh. This mesh is used by the drift-diffusion equation solver to obtain the charge density and potential distribution in the device. The current-voltage characteristic curve is post-processed from the results. The drift-diffusion equation solver module is implemented in C++ using an in-house parallelized finite element library called FEMLib which is based on PETSC [64]. Partitioning the computational mesh among the computer processors of a cluster is achieved using ParMETIS [65]. The non-linear problem is solved utilizing the 'Scalable Nonlinear Equation Solver' (SNES) module of the PETSC library. The linear system at each iteration of the

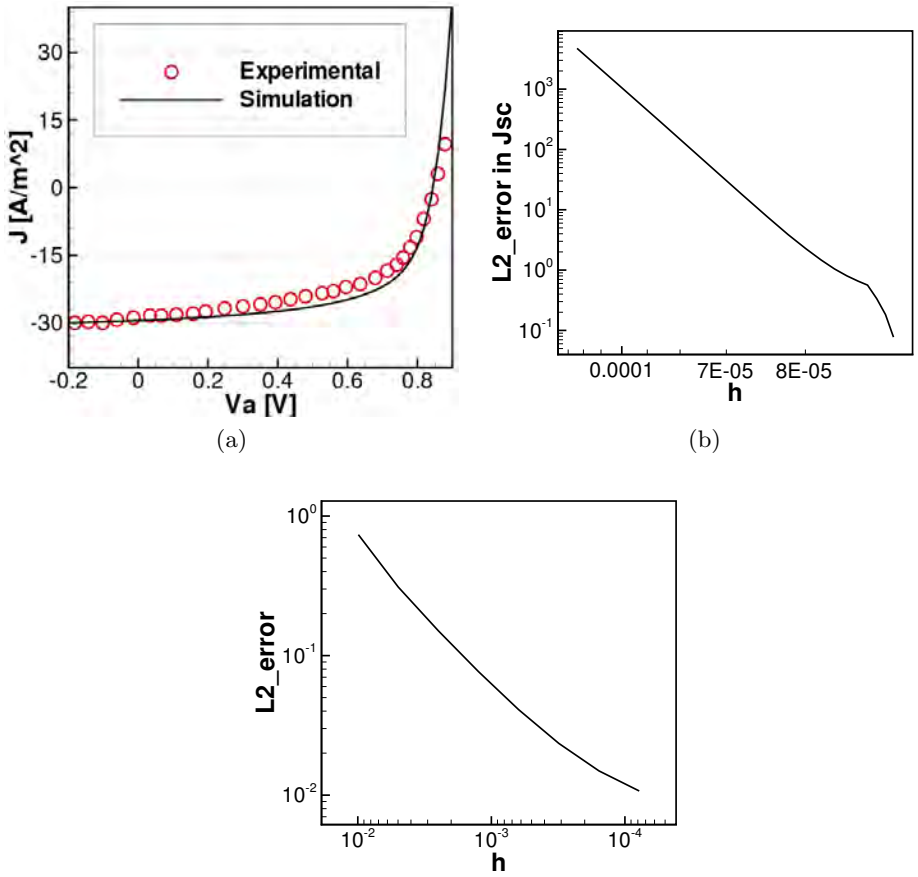

(a) (b)

(c)

Figure 2.6: a) Current voltage characteristic curve, b) Grid convergence plot of L_2 error in J_{sc} for OC_1C_{10}-PPV-PCBM, and c) L_2 error of $J_n + J_p$ for the simplified 1D problem, where analytical solution exists.

non-linear problem is solved using MUMPS [66] library.

2.4 Results and discussion

2.4.1 Validation of the framework

The framework can be used for one, two and three dimensional simulations with either homogeneous or heterogeneous microstructure assumption. To validate our framework, we consider a device with thickness of 120 nm fabricated using PPV-PCBM donor-acceptor blend. The material properties and charge generation and decay rates were obtained from literature

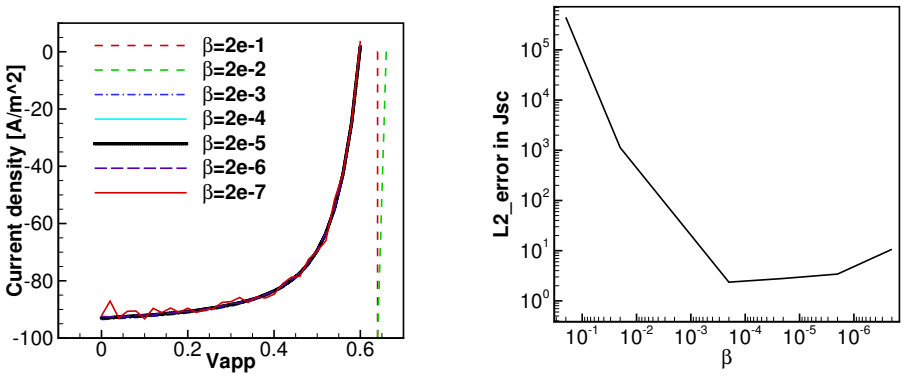

(a) (b)

Figure 2.7: Effect of using different values of clustering parameter β.

[41]. Computations were carried out with a mesh containing 800 elements along the thickness, with clustering ($\beta = 0.002$). A close match was observed between the current-voltage curves obtained from simulation and experiment (Figure. 2.6(a)). Furthermore, the numerical implementation was verified by plotting the grid convergence of error in total current-density values. The error was calculated by taking the difference in the value of short circuit current density obtained with sufficiently refined mesh (1000 mesh points in this case) and with other mesh element sizes (Figure. 2.6(b)). In addition, we also utilized the simplified problem where an analytical solution exists to check convergance. Figure. 2.6(c) shows the grid convergence of error obtained from the difference in numerical and analytical value of total current, $J_n + J_p$. The analytical value of $J_n + J_p$ is obtained for the drift-diffusion equations while assuming linear electrostatic potential ϕ in a 1-D domain with homogeneous material properties (see appendix A.10 for details).

2.4.2 Clustering

The level of clustering of mesh points at the electrode boundaries is critical to obtain accurate solution for current densities. Figure. 2.7(a) shows the current-voltage characteristic curves plotted at different levels of clustering, which is dependent on the parameter β. For low level of clustering which corresponds to larger values of β, the current-voltage plot is incorrect

as it consists of large oscillations. As the clustering is gradually increased by reducing β, the current-voltage plot converges. Small oscillations start to appear with further reduction in β indicating presence of an optimum value for the clustering parameter.

L^2 norm of the difference between short circuit current density at reference value of β and other values of β is plotted against β (Figure. 2.7(b)). This plot shows point of minimum error for β in the range 10^{-3} to 10^{-4}. All subsequent simulations use structured meshes clustered towards the electrode boundaries.

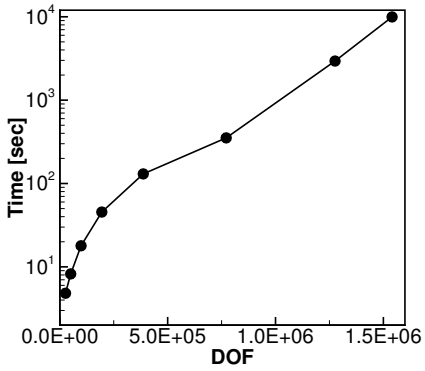

Figure 2.8: Timing with fixed number (eight) of processors

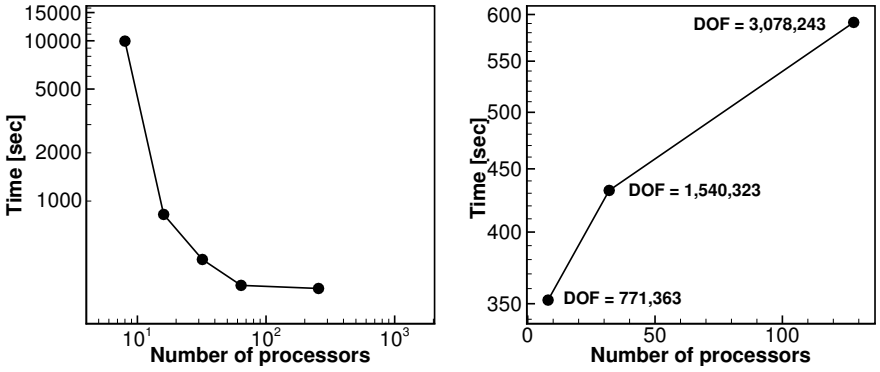

(a) (b)

Figure 2.9: a) Strong scalability (DOF∼1.5 million) b) Weak scalability (fixed problem size per processor)

2.4.3 Scalability of the framework

Numerical solution of finely resolved devices with heterogeneous morphology involves large degrees of freedom. It becomes especially evident when determining the external quantum efficiency by calculating the current density at various values of applied electrostatic potentials. This necessitates an efficient parallel implementation of the framework. We show the scalability tests performed with various numbers of computer cores and problem sizes. The problem considered was a two dimensional device with heterogeneous morphology (with properties associated with a P3HT-PCBM based organic solar cell). The time of execution was measured at short circuit conditions. The solver involved solution of three nonlinear coupled equations solved using Newton's method.

Scalability study was done on the National Center for Supercomputing Applications (NCSA)-ABE cluster which is part of the TeraGrid infrastructure in USA. Figure. 2.8 shows the timing measurements done on a single computer node with eight cores for increasing problem sizes. The problem size is changed by varying the number of elements in x direction while keeping the number of elements in y direction constant at 800. There is a jump in the amount of time observed for a total degree of freedom (DOF) $\sim$ 1.2 million. This, along with weak scalability shown in Figure. 3.4 b), indicated the approximate problem size per processor for efficient simulation. Figure. 3.4 a) shows the strong scaling analysis plot.

2.4.4 Effect of regular morphologies

Once the framework was validated, we use it to study the effect of bilayer and multilayer morphologies in vertical and horizontal configuration (regular morphologies) on device performance. This is similar to the investigation done by Ganesan et. al. [13] to study the effect of anisotropic mobility on the current-voltage plot. In this study, we assume an isotropic carrier mobility in order to isolate the effect of morphology on charge transport. This is shown by the current density plots in Figure. 2.10, 2.13 and 2.14. The distribution of the x and y components of current densities for vertical configurations are presented in Figure. 2.10 and 2.13. Only y-component of current density is shown for horizontal configuration as the values

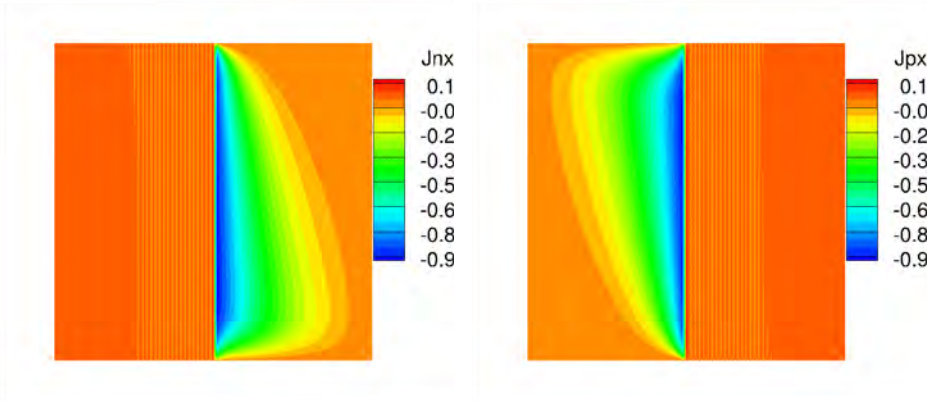

(a) Jn, 2 stripes

(b) Jp, 2 stripes

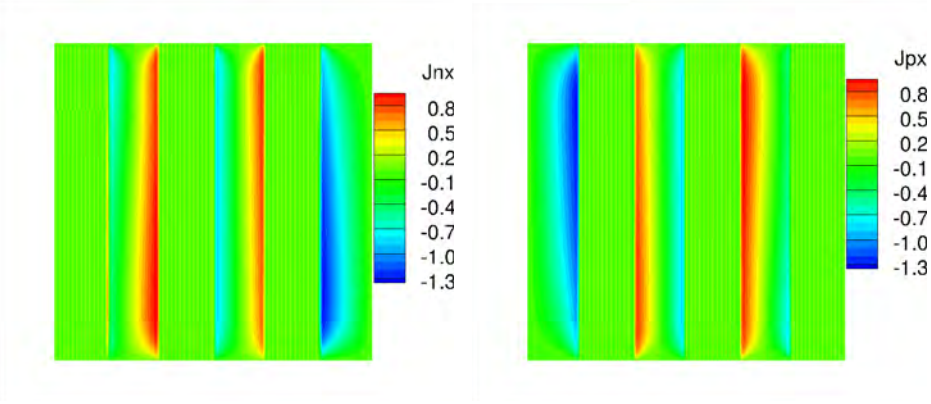

(c) Jn, 6 stripes

(d) Jp, 6 stripes

Figure 2.10: X-component of current density for vertical stripes microstructure

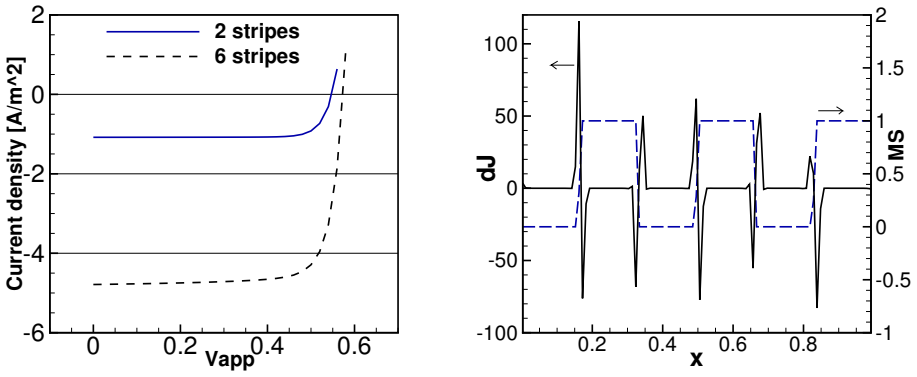

(a) (b)

Figure 2.11: a) Current-voltage plot b) $\nabla \cdot J$ along horizontal center line for vertical 6 stripes morphology

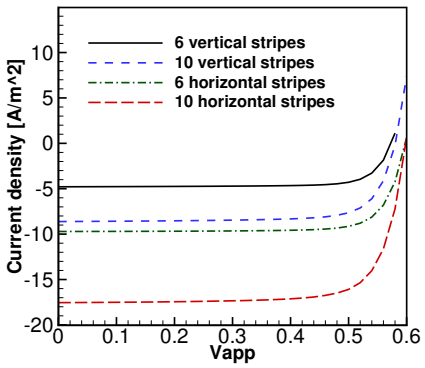

Figure 2.12: Current-voltage plot comparison for horizontal and vertical striped morphologies

for x-component are negligible. The horizontal configuration essentially represents a one dimensional device as there are no variation in x-direction. The morphologies were simulated on a mesh of size 100×800.

Figure. 2.10(a) and 2.10(b) shows the x-component of electron and hole current densities respectively for a vertical bilayer device and Figure. 2.10(c) and 2.10(d) shows that for a six layered device. The electrodes are placed at the top and bottom boundaries. The electrons are generated in the acceptor side of the vertical interface and holes in the donor side. The flow of electron and hole currents from interface to the respective electrodes, as can be inferred from the figure, is due to the electrostatic potential and the boundary conditions for charge densities at the electrodes.

A comparison of the current-voltage characteristic plots for the vertical configuration with 2 stripes and 6 stripes (Figure. 2.11(a)) shows the increase in short-circuit current and open-circuit voltage and hence the power conversion efficiency for multi-layered case. Figure. 2.11 (b) shows the plot of divergence of total current across the horizontal center line of the vertical configuration with 6 stripes. It is zero, as expected, away from the interface, while a jump is observed at the interface which corresponds to change in the nature of current from electrons to holes (see Remark 1).

Figure. 2.13 shows the y-component of the current densities for vertical bilayer and six layered devices. Figure. 2.14 shows the same for horizontal bilayer and six layered devices. Unlike the case of horizontal stripe morphologies, the current densities at the electrodes are not constant for vertically striped morphologies. Hence although the current density close to the interface at the electrodes is larger for vertical case, the total current available at the electrode – obtained by integrating over the electrode boundary – is larger for the horizontal case (see Figure. 2.12) [4].

Following observations can be made based on the visualization of the flow of charges generated at interface to electrode boundaries as shown in Figure. 2.10, 2.13 and 2.14. (1) Restriction of electron current to the acceptor region and of hole current to the donor region is captured.

[4]This would not be the case if anisotropy of charge carrier mobilities is considered, which would give larger current for vertical configuration.

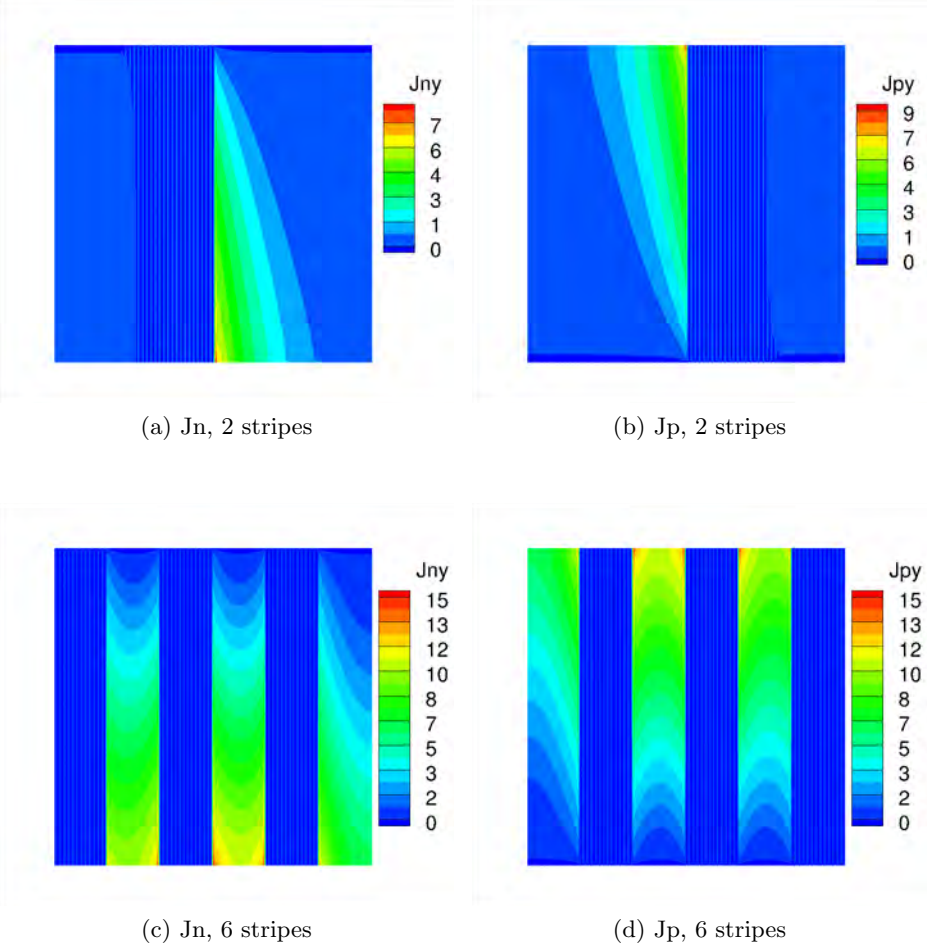

(a) Jn, 2 stripes

(b) Jp, 2 stripes

(c) Jn, 6 stripes

(d) Jp, 6 stripes

Figure 2.13: Y-component of current density for vertical stripes microstructure

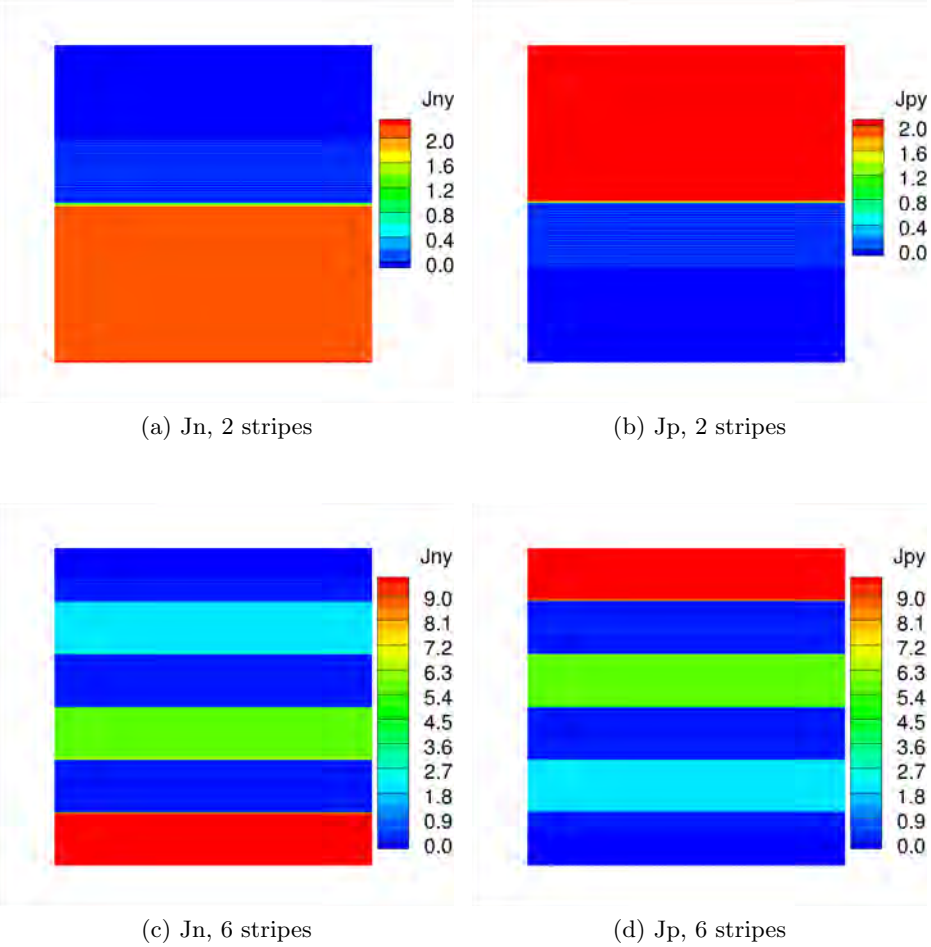

(a) Jn, 2 stripes

(b) Jp, 2 stripes

(c) Jn, 6 stripes

(d) Jp, 6 stripes

Figure 2.14: Y-component of current density for horizontal stripes microstructure

Figure 2.15: TEM image of a cross-section of active layer

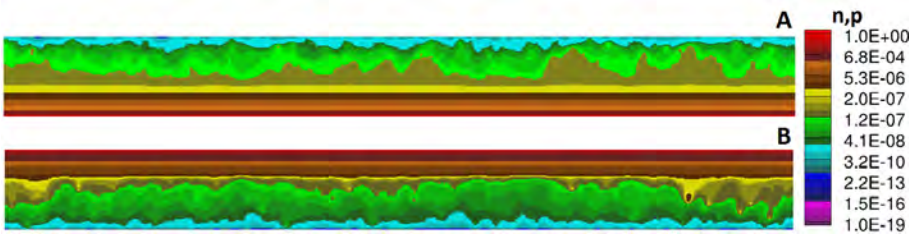

Figure 2.16: a) Electron density b) Hole density

(2) The amount of current collected at the electrode boundary depends on the surface area of acceptor at cathode and that of donor at anode boundary while limited by the minimum of the two.

2.4.5 Real device simulation

After investigating regular morphologies we consider a real morphology as observed in the active layer of OSC devices. In this section we demonstrate the use of our computational framework as a stereological microscope for virtual interrogation of real device microstructures. A computational investigation of this nature on real morphology has not been undertaken previously. Figure. 2.15(a) shows the binary image for a real microstructure of P3HT-PCBM

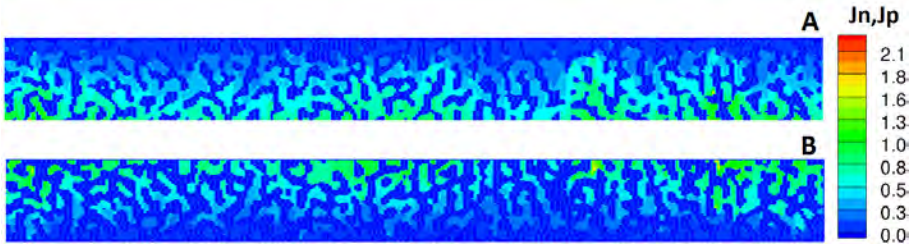

Figure 2.17: a) Electron current density b) Hole current density

blend obtained experimentally [67] using Transmission Electron Microscope. The region shown here is the vertical cross-section of the active layer of thickness 100nm. The top and bottom sides are connected to the anode and cathode respectively.

This image is read by the framework and the microstructure information interpolated onto the computational mesh. The scaled dimensions of the device are 10×1. Electron mobility ($2 \times 10^{-7} m^2/Vs$) and hole mobility ($1.5 \times 10^{-28} m^2/Vs$) are used in acceptor rich regions. Donor rich regions have an electron mobility of $2 \times 10^{-7} m^2/Vs$ and hole mobility of $1.5 \times 10^{-28} m^2/Vs$. The values of dielectric constant in acceptor in 3.9 while that in donor is 3. Interface width on the non-dimensionalized device is taken as 0.01. The charge generation rate away from the interface is taken as zero, while a constant value of 6×10^{27} is used for generation rate at interface throughout the device. A decay rate (k_f) of $1.2 \times 10^4 s^{-1}$ and electron-hole pair distance (a) of $2.5 \times 10^{-9} nm$ is used to calculate the probability of polaron dissociation in the interface region.

The charge density and potential distribution is calculated at short-circuit condition. Without the effect of the microstructure the contours for charge densities would show no variation in horizontal direction. But, as shown, there is a clear effect of the morphology on the distribution of charge carriers (Figure. 2.16(a) and 2.16(b)). Finally, electron current density and hole current density are obtained by post-processing the results for charge density and potential (Figure. 2.17(a) and 2.17(b)). The current densities being vector quantities, have components in x and y directions. Here, only the y-components are shown as the values of x-components of current densities is comparatively very small. Figure. 2.17(a) shows the distribution of the y-component of electron density in the acceptor region. The acceptor rich regions close to cathode show maximum values of electron current which reduces gradually as we move towards anode boundary. Similarly hole current density is maximum in the donor rich regions close to anode Figure. (2.17(b)). This emphasizes flow of electron generated at interface through the acceptor towards the cathode which is the bottom boundary and that of hole through donor towards anode.

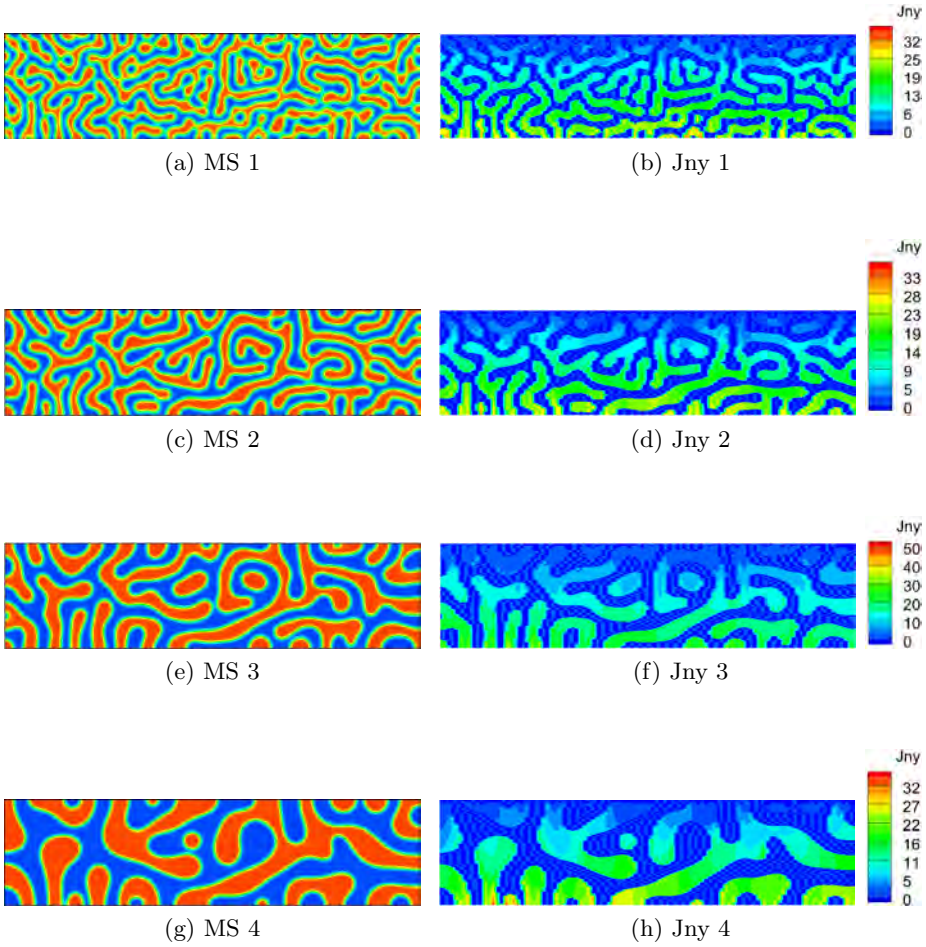

(a) MS 1 (b) Jny 1

(c) MS 2 (d) Jny 2

(e) MS 3 (f) Jny 3

(g) MS 4 (h) Jny 4

Figure 2.18: Microstructures with different feature sizes. The second column shows the distribution of y-component of electron current at short-circuit condition.

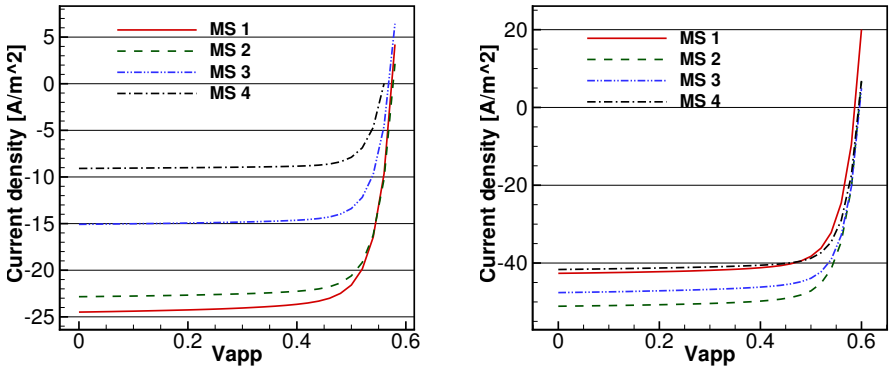

Figure 2.19: Comparison of current-voltage characteristic curves for the microstructures. a) Same value of charge generation rate at every interface. b) Same value of overall generation rate of the device.

2.4.6 Effect of microstructure on current-voltage curves

To delineate the effect of morphological properties like feature size, we show the current density distribution and current-voltage plots calculated for four device morphologies (Figure. 2.18) [5]. The effect of variation in the feature size and distribution (Figure. 2.18) on the electrical properties has been captured in Figure. 2.19 and we explain it below.

First we consider a constant generation rate per unit length at interfaces throughout the device for all four morphologies. Hence a device with large interface area would have more overall generation rate. Figure. 2.19(a) shows the current-voltage characteristic curves for this case. As the total interface area[6] decreases from MS 1 (14.3%), MS 2 (11.2%), MS 3 (7.9%) to MS 4 (5.4%), the magnitude of the short-circuit current density decreases due to decrease in total charge generation rate over the device. A constant generation rate per unit length is however not a very good approximation of the physics. Smaller feature size would result in more charge generation as there are more interfaces available. On the other hand larger feature size makes it easier for the charges to travel towards the electrodes than the highly winding

[5]These microstructures are solutions to the morphology evolution problem solved using the Cahn-Hilliard equations, corresponding to a blend ratio of 1:1 between polymer and fullerene with material parameter χ=2.2. For more details please refer [21]

[6]The values in the brackets indicate the fraction of the total area that is covered by the interface

pathways –with dead ends and bottlenecks– provided by blends with smaller feature size. We do not observe effect of charge transport in case a) as the charge generation effect is dominant.

To isolate the effects of charge transport, the value of *total generation rate over the device* is maintained constant for the four morphologies. This would eliminate the effect of generation rate on the device morphology and show only the effect of charge transport. Figure. 2.19(b) shows the current-voltage characteristic curves for this case. Here, the relative variation in the short-circuit current density values is lower when compared to case (a). Also, the current-voltage plots do not show the regular trend for the four devices as observed in case (a). The short-circuit current for MS 1 is lowest in case (b) instead of highest as in case (a). This is due to reduced charge transport caused by increased number of dead ends and bottlenecks.

2.4.7 Three dimensional simulation

We finally demonstrate the application of the framework to investigate the effect of three dimensional heterogeneous morphology on the distribution of current density. To our best knowledge, this is the first time that three dimensional simulations of realistic morphologies have been performed.

Two device morphologies fabricated with different P3HT:PCBM blend ratios are analyzed in this study[7]. The blend ratio's of the two morphologies are $1:2$ and $1:3$. The devices (and their morphologies) are visualized in Figure. 2.20(b) (1:2 blend ratio), and Figure. 2.21(b) (1:3 blend ratio). Notice that the morphology fabricated using a $1:2$ blend ratio has a very interpenetrated structure, with the P3HT:PCBM interface forming a percolating structure across the domain. In contrast, the morphology fabricated using the $1:3$ blend ratio is very globular, with the P3HT forming isolated spheroidal particles in a PCBM matrix. These morphologies are chosen to elucidate the effect of percolating interfaces on enhanced charge transport and hence the device efficiency.

The cathode and anode planes are shown in Figure. 2.20(b) and Figure. 2.21(b). For ease of visualization, the cathode side view of the microstructures are shown in Figures. 2.20(a)

[7]These morphologies were obtained from solutions of the unsteady Cahn-Hilliard equations for different blend ratios [21]

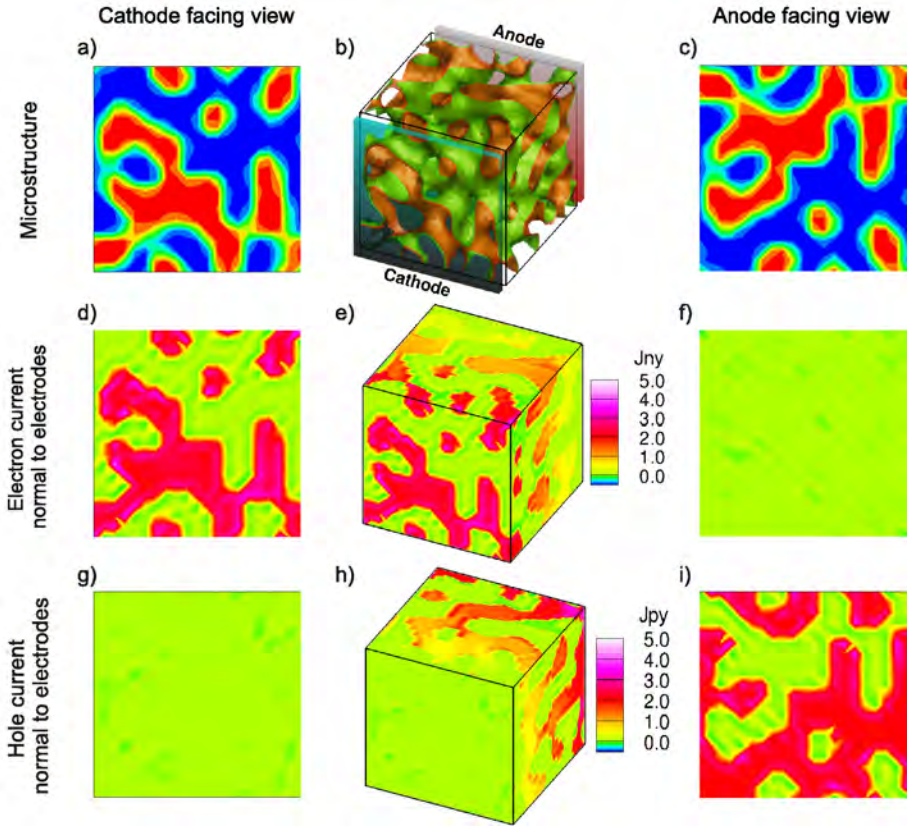

Figure 2.20: Electron and hole current distributions for a device fabricated using a polymer:fullerene blend ratio of 1:2. Row 1 displays various views of the microstructure. Row 2 displays various views of the electron current density and Row 3 displays various views of the hole current density

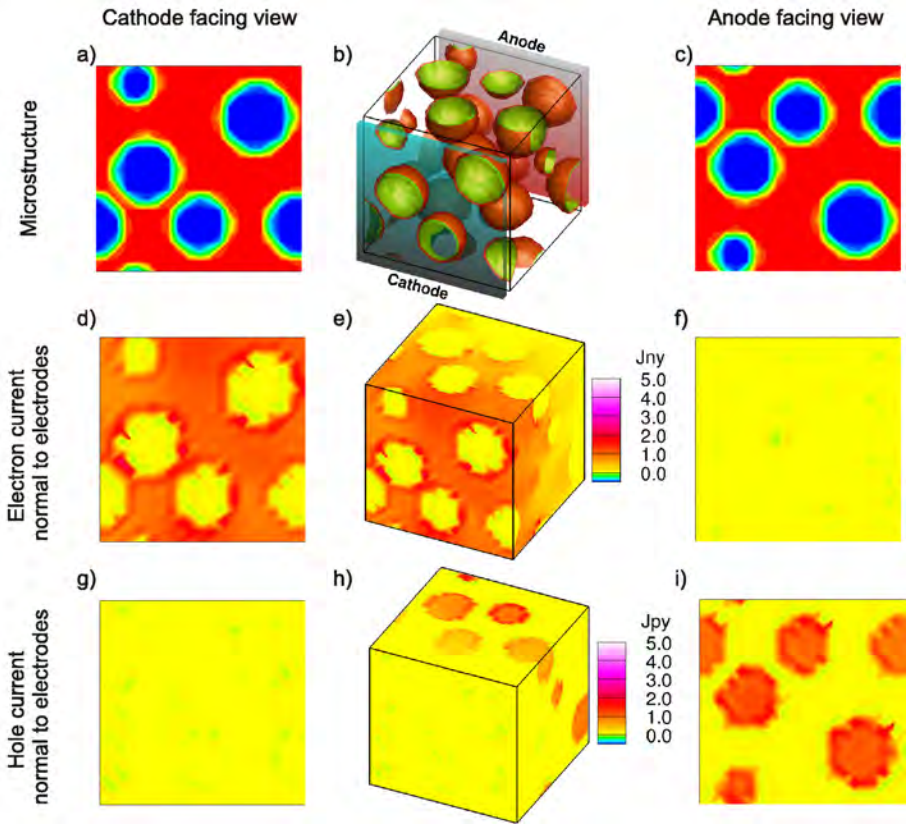

Figure 2.21: Electron and hole current distributions for a device fabricated using a polymer:fullerene blend ratio of 1:3. Row 1 displays various views of the microstructure. Row 2 displays various views of the electron current density and Row 3 displays various views of the hole current density

and 2.21(a) while the anode side view of the microstructures are shown in Figures. 2.20(c) and 2.21(c). A constant generation rate at the donor:acceptor (P3HT:PCBM) interface throughout the device is applied and the charge distributions and hole and electron current densities are computed. The morphologies were simulated on a mesh of size $30 \times 800 \times 30$.

Figure. 2.20(e) plots contours of the component of electron current density normal to electrodes (J_{ny}) while Figure. 2.20(h) plots contours of the component of hole current density to electrodes (J_{py}). A gradual increase in J_{ny} from anode to cathode can be seen in Figure. 2.20(e) with maximum value of J_{ny} observed at the cross-section of acceptor in contact with cathode (red regions in Figure. 2.20(d)). A reverse trend is observed for J_{py} which is maximum where the donor is in contact with anode (red regions in Figure. 2.20(i)). Note also that the electron current at the cathode (Figure. 2.20(d)) closely mimics the microstructure at the cathode (Figure. 2.20(a)), while the hole current at the anode (Figure. 2.20(i)) mimics the microstructure at the anode (Figure. 2.20(c)).

Similarly, Figure. 2.21 shows results for a device with donor:acceptor blend ratio of 1:3. The major difference between Figure. 2.20 and Figure. 2.21 is the significant reduction in the total current density of both electron and holes generated (both figures are plotted to the same scale). This is primarily due to the difference in morphologies (interpenetrating vs spheroidal) that affects charge transport. Equal fractions of donor and acceptor material in the blend give rise to a three dimensional percolating network of interfaces whereas a blend ratio of 1:3 gives rise to a structure where the acceptor material is matrix like with globules of donor material dispersed in it. The morphology with 1:3 blend ratio shows lower values of electrode current at short circuit conditions. This is in agreement with the experimental [68] observation of best efficiencies for P3HT:PCBM blend weight ratio of 1:1 to 1:2.

2.5 Conclusions and future work

We showcase an efficient framework for quick virtual interrogation of real microstructures obtained either from experiments or simulation. A computationally efficient model is proposed, which is capable of distinguishing the charge transport properties of devices with different morphologies. A novel post-processing technique based on transformation of charge densities to

fermi-level variables is introduced for accurate current calculation. Computational strategies including grid clustering and continued Newton's method have been shown to improved convergence the nonlinear problem. A parallel implementation of the framework is show-cased and results from scalability study are shown.

We investigated the effect of feature size and heterogeneous microstructures on the charge transport mechanism of thin film organic solar cells. Additionally, plots of charge density and current density distribution help visualize and interpret the effect of morphology on device performance. The framework was successfully tested to distinguish between the current-voltage characteristic plots of devices with different microstructures. In particular, the electrical properties of a real device morphology obtained using TEM measurement are presented. Additionally, (for the first time) charge transport through realistic heterogeneous 3D morphologies are analyzed which quantitatively elucidate the importance of an interpenetrating morphology for higher device efficiencies.

Future work consists of augmenting this charge transport framework to include exciton generation and diffusion [42]. Other avenues of work include (a) predicting 3D optimal morphologies for maximized charge generation and transport, and (b) investigating the effects of dispersed ferro-electric, quantum dots and magnetic particles in the thin film on charge transport.

Acknowledgments

This research was supported in part by the National Science Foundation through TeraGrid resources provided by TACC under grant number TG-CTS110007. BG was supported in part by NSF PHY-0941576, and NSF-1149365.

CHAPTER 3. COMPUTER SIMULATION OF HETEROGENEOUS POLYMER PHOTOVOLTAIC DEVICES

A paper published in *Modelling and Simulation in Materials Science and Engineering*

Hari K. Kodali and Baskar Ganapathysubramanian

Abstract

Polymer based photovoltaic devices have the potential for widespread usage due to their low cost-per-watt and mechanical flexibility. Efficiencies close to 8.3% [16] have been achieved recently in conjugated polymer based organic solar cells. These devices were fabricated using solvent-based processing of electron-donating and electron-accepting materials into the so-called bulk heterojunction (BHJ) architecture. Experimental evidence suggests that a key property determining the power-conversion efficiency of such devices is the final morphological distribution of the donor and acceptor constituents. In order to understand the role of morphology on device performance, we develop a scalable computational framework that efficiently interrogates organic solar cells to investigate relationships between the morphology at the nano-scale with the device performance.

In this work, we extend the Buxton and Clarke (2007) [3] model to simulate realistic devices with complex active layer morphologies using a dimensionally independent, scalable, finite element method. We incorporate all stages involved in current generation, namely 1) exciton generation and diffusion, 2) charge generation, and 3) charge transport in a modular fashion.The numerical challenges encountered during interrogation of realistic microstructures are detailed. We compare each stage of the photovoltaic process for two microstructures – a bulk heterojunction morphology and an idealized sawtooth morphology. The results are presented

for both two and three dimensional structures.

3.1 Introduction

The utility of cheap sources of renewable energy in a world faced with dwindling conventional energy sources and climate change is indisputable. Solar radiation is one of the most promising and long term sources of renewable energy. Traditional inorganic solar cells have made significant progress in harnessing this energy, but their high manufacturing cost still prohibits widespread usage. In contrast, organic solar cells (OSC) permit large-area fabrication (by incorporating facile manufacturing suitable for roll-to-roll processing) which potentially gives a much cheaper source of photoelectric conversion [17]. In addition, compatibility with flexible substrates, high optical absorption and easy tunability by chemical doping [18] make OSC devices even more attractive for versatile applications at large (solar farms, exterior walls of buildings) as well as small (garments, umbrellas, handbags [19]) scales.

In recent years, we have witnessed significant improvement in efficiencies (from below 3% [29] to the current highest reported value of 8.13% [16] obtained under laboratory conditions). New materials development [30, 31, 32], and device designs [33, 34, 35] are largely responsible for this improvement. Tailoring the morphology of the active layer will have significant effect on the final performance of the device, as suggested by experimental evidence [36, 26, 37, 38]. For instance, efficiency gains have been reported by changing the morphology using a higher boiling point solvent [29] during processing, annealing [28] at a temperature above the glass transition of the polymer and by making use of additives [39, 40]. Still, compared to inorganic devices, polymer devices have very low efficiency which can be significantly improved by tuning the morphology [28].

High-throughput experiments to test (and tune) devices with various morphologies is time consuming, resource intensive and prohibitively expensive. A computational framework which can *efficiently interrogate the microstructure by capturing the physics of charge generation and transport in organic solar cells* will be immensely helpful in understanding the effect of morphology on performance, thus allowing the design of high efficiency solar cells. Broadly, there are two classes of computational models used to interrogate heterogeneous semiconductor

devices: (1) microscopic and (2) continuum models.

Microscopic models (Monte Carlo technique and derivatives) [45, 46, 47] have been used successfully to determine the effect of morphology on generation, recombination and transport of excitons and charges. These methods have been used to delineate and understand the various sub-processes in semiconductor analysis [48, 49]. However, these methods have some significant drawbacks. In particular, the computational cost involved with three dimensional simulations and high throughput analysis (for morphology characterization) is prohibitive. In addition, long range nature of Coulomb interaction limits the use of microscopic models [12] when full device simulations are needed.

Continuum models provide a computationally efficient alternative to microscopic models. Continuum models based on excitonic drift-diffusion equations for heterogeneous microstucture have been considered by Barker et al. [9], Buxton and Clarke [10], Martin et al. [11], Williams et al. [12] and Ganesan et al. [13]. The excitonic drift-diffusion model is obtained by adding an additional exciton diffusion equation to the standard current-continuity and Poisson equations, i.e. the standard drift-diffusion model. The drift-diffusion model is derived from the Boltzmann transport equation by replacing actual carrier distribution function with equilibrium distribution function assuming the charge carrier temperature to be constant throughout the device [50].[1] We note that the utility of the continuum model hinges on the accurate representation of dissociation, recombination processes and mobilities. However, a scalable and efficient implementation of the continuum model will allow rapid classification and approximate rank ordering necessary for high-throughput analysis.[2] In addition a continuum model will facilitate investigation of various long range interactions and testing of different models for the sub-processes.

[1] This model breaks down under high electric field and when the device dimension (distance between the electrodes) is short compared to the carrier mean-free path ($\sim$ 5-8 nm for donor material [43]). Carriers accelerate under high electric field, and scattering is not sufficiently strong to bring the carrier temperature back to lattice temperature. A short high-field region causes the distribution function to become highly asymmetric which cannot be approximated by equilibrium distribution function. Typical thickness of the active layer of an OSC device is around 100 nm, which is much larger than the carrier mean-free path. The range of interest for the externally applied potential, in order to characterize the device, is from zero volts to the open circuit voltage. Thus, the device dimensions and operating conditions for OSC devices permit the use of drift-diffusion model.

[2] The most promising candidate morphologies from such high-throughput analysis can subsequently be subjected to more rigorous interrogation, thus significantly cutting down on computational overhead.

Our contributions in this paper are the following: **(1)** We extend the excitonic drift-diffusion model which was successfully applied to organic semiconductor devices with regular microstructures [9, 10, 11, 12, 13]. **(2)** We implement a parallelized finite element framework to efficiently interrogate device scale morphologies. **(3)** Investigate electrical properties of realistic interpenetrating heterogeneous microstructures. **(4)** Characterize effects of interfacial area on each stage of current generation process. **(5)** Perform a stage-by-stage comparison of a percolating and an idealized sawtooth microstructure.

3.2 Problem definition

3.2.1 Device morphology

Fig. 3.2 shows a typical configuration of an organic solar cell. The active layer comprised of a blend of donor and acceptor materials forms the domain under consideration. Fig. 3.1 shows the structure of the active layer as seen under a transmission electron microscope [6] [3]. The top and bottom boundaries are connected to electrodes. Typically the anode is transparent to the visible region of radiation spectrum, while the metallic cathode is reflective.[4]

Figure 3.1: Morphology of the active layer for a typical donor-acceptor system imaged using TEM [6]. Dimensions are 1200nm×100nm.

3.2.2 Device Physics

The active layer of OSC devices (Fig. 3.2) consists of a blend of electron donor and electron acceptor materials. The current generation process in OSC can be broadly divided into three stages. *Stage 1 - Exciton generation and diffusion*: Absorption of light resulting in generation

[3]The white region denotes Regio-regular poly(3-hexylthiophene) (rrP3HT or polymer) and black region is [6,6]-phenyl-C61 butyric acid methyl ester (PCBM or fullerene).

[4]Indium Tin Oxide (ITO) covered with a conducting polymer like poly(3,4-ethylenedioxythiophene): poly(styrenesulfonate) (PEDOT:PSS) and Aluminum are examples of transparent anode and reflecting cathode, respectively.

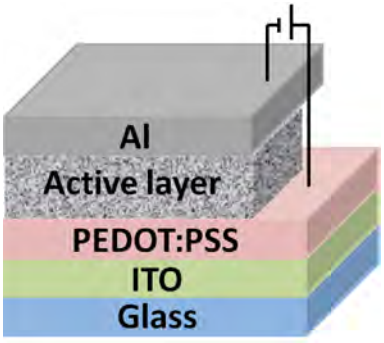

Figure 3.2: Schematic of the cross-section of a typical organic solar cell device along the thickness.

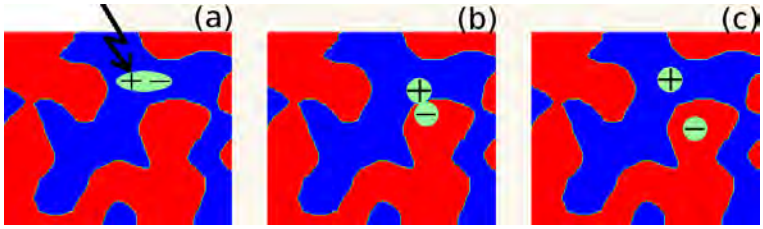

Figure 3.3: Device operation. (a) Photon absorption/exciton generation. (b) Exciton diffusion and charge separation. (c) Free charge creation and transport

and subsequent diffusion of tightly coupled electron-hole pairs known as exciton's towards the DA interface. *Stage 2 - Charge generation*: The excitons then separate at the interface to form electrons in the acceptor region and holes in the donor region. *Stage 3 - Charge transport*: Movement of electrons and holes towards the cathode and anode, respectively. Each stage is described in detail as follows:

Stage 1: The electron donor in the active layer of the OSC absorbs the photons reaching it through the transparent electrode. Unlike inorganic photovoltaic devices where the absorbed photons directly create free electron-hole pairs, organic photovoltaic devices give rise to tightly bound electron-hole pairs known as excitons [28] (Fig. 3.3(A)). These excitons, which have a short lifetime of $\sim$ 0.5 nanoseconds [43], must diffuse to the donor-acceptor interface in order to be separated into free charges.

Stage 2: At the interface, [44] the difference in electron affinity of the materials causes the electron in the exciton to jump to the acceptor (Fig. 3.3(B)). The hole remains in the donor region. This transfer of electron causes the electron-hole pair to become loosely bound. The loosely bound electron and hole can be separated by the local electric field at the interface.

Stage 3: Once the exciton has separated into a free electron and a hole in the two regions across the interface, the charges travel to the electrodes through the respective materials. That is, the electron is transported through the acceptor-rich region towards the anode, while the hole is transported through the donor-rich regions towards the cathode (Fig. 3.3(C)). The transport characteristics is affected by the local electric field [28]. The tortuous structure of the pathways (see Fig. 3.1) makes transport of the generated charges towards the electrodes a complex process.

3.2.3 Device Model

The equations describing the charge transport processes in a heterogeneous organic solar cell are given below. The four fields of interest are the electron density n, hole density p, electrostatic potential ϕ and exciton density X.

$$\nabla \cdot (\epsilon \nabla \phi) = q(n - p) \tag{3.1}$$

$$\nabla \cdot \mathbf{J_n} = -qf\mathcal{D}_{[\nabla\phi,X]} + qf\mathcal{R}_{[n,p]} \tag{3.2}$$

$$\nabla \cdot \mathbf{J_p} = +qf\mathcal{D}_{[\nabla\phi,X]} - qf\mathcal{R}_{[n,p]} \tag{3.3}$$

$$\mathbf{J_n} = -qn\mu_n \nabla\phi + qV_t\mu_n \nabla n \tag{3.4}$$

$$\mathbf{J_p} = -qp\mu_p \nabla\phi - qV_t\mu_p \nabla p \tag{3.5}$$

$$\nabla \cdot (V_t\mu_X \nabla X) - f\mathcal{D}_{[\nabla\phi,X]} - \mathcal{R}_{[X]} = -\mathcal{G} - f\mathcal{R}_{[n,p]} \tag{3.6}$$

where the Poisson equation (Eqn. (4.1)) incorporates the effect of electron and hole densities on potential ϕ in the active layer. ϵ is the dielectric constant, and is a spatially varying field. Eqns. (4.2), (4.3) are commonly known as the current continuity equations. The notations for electron and hole current densities are $\mathbf{J_n}$ and $\mathbf{J_p}$, respectively. The exciton generation, diffusion and dissociation are represented by Eqn. (4.6). $\mathcal{G}$ and $\mathcal{D}_{[\nabla\phi,X]}$ denotes rate of exciton generation and dissociation, respectively. Exciton relaxation rate is denoted by $\mathcal{R}_{[X]}$.

Remark 1: Donor-acceptor interface The exciton dissociation $\mathcal{D}_{[\nabla\phi,X]}$ and charge recombination $\mathcal{R}_{[n,p]}$ are confined to a thin region at the DA interface using the factor f. This is similar to the boundary condition for excitons at the interface, used by Martin (2007) [11]. The factor f takes a value of one in the thin region (∼2nm thick) across DA interface which is used to approximate the interfacial region. f is zero elsewhere. This finite interfacial region allows transport of both electron and holes but the electrons are restricted to acceptor regions (and holes to donor regions) by using a mobility value 20 orders of magnitude lower than the mobility in acceptor regions (donor regions in case of holes).

The mobilities for electron, holes and excitons are denoted by μ_n, μ_p and μ_X, respectively. The thermal voltage $V_t = k_B T/q$, where k_B is the Boltzmann constant, T the temperature and q denotes elementary charge. The Onsager dissociation rate [9] $\mathcal{D}$ is given by

$$\mathcal{D}_{[\nabla\phi,X]} = \frac{3\gamma}{4\pi a^3} e^{-E_b/K_B T} \frac{J_1(2\sqrt{-2b})}{\sqrt{-2b}} X \tag{3.7}$$

In this expression $E_b = q^2/(4\pi\epsilon x)$ is the exciton binding energy,
$b = q^3|\nabla\phi|/(8\pi\epsilon k_B^2 T^2)$ is the field parameter and J_1 is the first order Bessel function given by

$$\frac{J_1(2\sqrt{-2b})}{\sqrt{-2b}} = \sum_{m=0}^{\infty} \frac{(2b)^m}{m!(m+1)!} \tag{3.8}$$

The charge recombination $\mathcal{R}_{[n,p]} = \gamma np$, where γ is the Langevin recombination parameter. In the present study, the following form for Langevin parameter $\gamma = \frac{q}{\epsilon}(\mu_n + \mu_p)$ [3] is used. The exciton relaxation $\mathcal{R}_{[X]} = X/\tau_X$ [3], where τ_X is the average lifetime of an exciton. Generation rate of excitons is given by $\mathcal{G}_{[x]} = \alpha_0 \Gamma_0 exp(-\alpha_0 x)$, where α_0 is the absorption coefficient, Γ_0 the photon flux, and x is the distance from the top of the active layer which is in contact with the transparent electrode.

Remark 2: Boundary conditions Assuming the cathode and anode to line up with the conduction and valence band, respectively, the boundary conditions [53, 54] for the charge densities is given by

$$\begin{aligned} n_{[C]} &= N_C \\ p_{[C]} &= N_V exp(\frac{-E_{gap}}{V_t}) \end{aligned} \tag{3.9}$$

for the cathode, and

$$n_{[V]} = N_C exp(\frac{-E_{gap}}{V_t})$$
$$p_{[V]} = N_V \tag{3.10}$$

for the anode. Here, E_{gap} is the band gap and N_C, N_V denote the effective density of states of conduction and valence band, respectively. The built-in potential V_{bi} is given by $qV_{bi} = \varphi_{an} - \varphi_{cat}$, where φ_{an} and φ_{cat} are the work functions for the anode and the cathode, respectively. Alignment of electrodes with the conduction and valence bands gives $V_{bi} = E_{gap}$. Hence, the boundary condition for potential at the electrodes is given by

$$\phi_C - \phi_V = E_{gap} - V_a \tag{3.11}$$

where V_a is the applied voltage.

Remark 3: Current-Voltage plot The solution of the excitonic drift-diffusion equations (4.1-4.6) is used to calculate the electron and hole current density vectors using Eqns. (4.4) and (4.5). [5] The current density available from the device is obtained by integrating the normal component of J_n,J_p at the electrodes. The variation of current density is plotted for a range of applied voltages – zero volts to open circuit voltage – and is popularly known as the current-voltage characteristic plot.

3.3 Methodology

In addition to the numerical instabilities due the drift term in current-continuity equations, the highly coupled nature of the Eqns. (4.1-4.6) makes a computational solution non-trivial. Approximately 20 orders of magnitude variation in the charge distributions (n, and p), and device thickness in nanometers may lead to overflow and underflow errors. Moreover, the large problem size obtained due to the need to resolve the fine morphological details necessitates

[5] As the expressions for current densities involve derivatives of the calculated charge densities and potential, large errors may be introduced while post-processing for current density vectors. We have developed an efficient current calculation strategy [69] to calculate current density in the entire domain, based on replacing the charge densities by their quasi-Fermi level counterparts.

parallelization in order to be able to perform high throughput analysis of different microstructures.

This section details the computational approach used to solve Eqns. (4.1-4.6).

3.3.1 Non-dimensionalized equations

Use of normalized units helps to avoid numerical overflow/underflow and improves the efficiency of the algorithms. Using the scaling strategy of Markowich [55], the basic equations transform into the following.

$$\hat{\nabla} \cdot (\lambda^2 \hat{\nabla} \hat{\phi}) = (\hat{n} - \hat{p}) \tag{3.12}$$

$$\hat{\nabla} \cdot (-\hat{\mu_n} \hat{n} \hat{\nabla} \hat{\phi} + \hat{\mu_n} \hat{\nabla} \hat{n}) = -f\hat{\mathcal{D}} + f\hat{\mathcal{R}}_{[n,p]} \tag{3.13}$$

$$\hat{\nabla} \cdot (\hat{\mu_p} \hat{p} \hat{\nabla} \hat{\phi} + \hat{\mu_p} \hat{\nabla} \hat{p}) = -f\hat{\mathcal{D}} + f\hat{\mathcal{R}}_{[n,p]} \tag{3.14}$$

$$\hat{\nabla} \cdot (\hat{\mu_X} \hat{\nabla} \hat{X}) = f\hat{\mathcal{D}} + \hat{\mathcal{R}}_{[X]} - \hat{\mathcal{G}} - f\hat{\mathcal{R}}_{[n,p]} \tag{3.15}$$

where $\hat{}$ denotes non-dimensionalization. $\hat{}$ will not be used in the sequel for notational convenience.

Finite element formulation We use a finite element formulation to solve this set of Eqns. (3.12-3.15). The numerical instabilities associated with the presence of drift (convective) term in the current-continuity equations is taken care by using the Streamline Upwind Petrov Galerkin (SUPG) formulation [56]. The weak form of the problem defined by Eqns. (3.12-3.15) can be stated as,

Given a domain Ω, with boundary $\partial\Omega$, find $\phi, n, p, X \in H^1(\Omega)$, $\phi = \phi_D$, $n = n_D$, $p = p_D$, $X = X_D$ on $\partial\Omega_D$ such that

$$\int_\Omega \left(\nabla \cdot (\lambda^2 \nabla \phi) - (n - p)\right) w d\Omega = 0 \tag{3.16}$$

$$\int_\Omega \left(\nabla \cdot \mathbf{J_n} - (-f\mathcal{D} + f\mathcal{R}_{[n,p]})\right) (w + q^*) d\Omega = 0 \tag{3.17}$$

$$\int_\Omega \left(\nabla \cdot \mathbf{J_p} - (+f\mathcal{D} - f\mathcal{R}_{[n,p]})\right) (w + q^*) d\Omega = 0 \tag{3.18}$$

$$\int_\Omega \left(\nabla \cdot (\mu_X \nabla X) - f\mathcal{D} - \mathcal{R}_{[X]} + \mathcal{G} + f\mathcal{R}_{[n,p]}\right) w d\Omega = 0 \tag{3.19}$$

for all $w \epsilon H^1(\Omega)$, $w = 0$ on $\partial\Omega_D$, where $H^1(\Omega)$ represents the Sobolev space. ϕ_D, n_D, p_D and X_D represent the Dirichlet boundary values for the potential ϕ, charge densities n and p, and exciton density X, respectively. q^* is the SUPG function which modifies the Galerkin test function w to a Petrov-Galerkin test function $(w + q^*)$ [56]. On the remainder of the domain boundary $\partial\Omega/\partial\Omega_D$, a zero boundary condition for the normal component of $\nabla\phi$, J_n and J_p is implicitly applied.

Discretization In this stage we replace the infinite dimensional solution space $H^1(\Omega)$ with a finite dimensional approximate $H^h(\Omega)$ representing the discrete solution set on a grid. The finite dimensional counterparts of the solution variables ϕ, n, p, X are denoted by ϕ_h, n_h, p_h, X_h. The Galerkin form of equations can be stated as follows:

Find $\phi_h, n_h, p_h, X_h \epsilon H^h(\Omega)$, satisfying the essential boundary conditions such that

$$\int_\Omega \Big(-\lambda^2 \nabla\phi_h \cdot \nabla w_h - (n_h - p_h) w_h\Big) d\Omega = 0 \tag{3.20}$$

$$\int_\Omega \left(n_h \nabla\phi_h \cdot \nabla w_h - \nabla n_h \cdot \nabla w_h - \nabla n_h \cdot \nabla\phi_h q_h^*\right) d\Omega = \int_\Omega (-f\mathcal{D} + f\mathcal{R}_{[n,p]})(w_h + q_h^*)/\mu_n \tag{3.21}$$

$$\int_\Omega \left(p_h \nabla\phi_h \cdot \nabla w_h + \nabla p_h \cdot \nabla w_h - \nabla p_h \cdot \nabla\phi_h q_h^*\right) d\Omega = \int_\Omega (+f\mathcal{D} - f\mathcal{R}_{[n,p]})(w_h + q_h^*)/\mu_p \tag{3.22}$$

$$-\int_\Omega \mu_X \left(\nabla X \cdot \nabla w\right) d\Omega = \int_\Omega \left(f\mathcal{D} + \mathcal{R}_{[X]} - \mathcal{G} - f\mathcal{R}_{[n,p]}\right) w d\Omega \tag{3.23}$$

for all $w_h \epsilon H^h$, where ϕ_h, n_h, p_h and X_h are the Galerkin approximations to the electrostatic potential, electron density, hole density and exciton density, respectively. The discretized equations (3.20-3.23) generates a coupled system of non-linear algebraic equations.

3.3.2 The computational framework

Overview Given the microstructural description of the device, the morphological details are mapped onto a computational mesh. This mesh is used by the excitonic drift-diffusion equation solver to obtain the charge density and potential distribution in the device. The current-voltage characteristic curve is post-processed from the results.

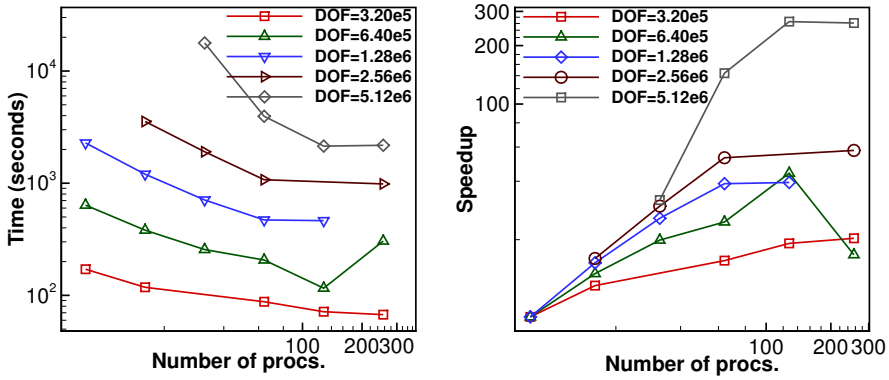

(a) Timing study (b) Speedup

Figure 3.4: Scaling of the parallelized framework.

Framework setup and domain decomposition The drift-diffusion equation solver module is implemented in C++ using an in-house parallelized finite element library which is based on PETSC [64].

Determining the electrical properties of heterogeneous polymer devices with small feature sizes requires fine mesh resolution. Additionally, the relatively large device dimensions (1000nm X 100nm) considered in the present study results in large degrees of freedom. Furthermore, we need to solve the non-linear excitonic drift diffusion equations at different values of applied voltages in order to obtain the current-voltage characteristic curve. This necessitates parallelization of the framework for quick simulations. We utilize domain decomposition strategy to partition the computational mesh among the processors of a cluster using ParMETIS [65].

Solvers The non-linear problem is solved utilizing the 'Scalable Nonlinear Equation Solver' (SNES) module of the PETSC library. The linear system at each iteration of the non-linear problem is solved using the MUMPS [66] library.

Scaling analysis We consider a heterogeneous two dimensional morphology for the timing study. The non-linear excitonic drift-diffusion equations were solved using Newton's method with relative tolerance for convergence set to 10^{-12}. The code was compiled with optimization options for the compiler set on. The timing tests were performed on the 'Cystorm' cluster at

Iowa State University which consists of 3200 computer processor cores and high-speed infiniband interconnection.

Fig. 3.4 (a) and (b) show the results of the scaling study for different number of degrees of freedom. The plots allow us to determine the optimum number of processors to use for a problem with specific number of degrees of freedom. A problem size of 1.28 million degrees of freedom solved on around 60 processors would result in maximum speedup. These plots (Fig. 3.4) show a reduction in solution time with increase in processors used, and this reduction is improved as the problem size increases.

The three dimensional simulations scale similar to their two dimensional counterparts with some deterioration due to increased bandwidth of the stiffness matrix.

3.4 Results and discussion

3.4.1 Realistic heterogeneous morphology

We utilize the computational framework to capture the influence of realistic active layer morphology on the electrical properties of a photovoltaic device. Fig. 3.5 (a) shows the vertical cross-section of the active layer of a heterogeneous organic photovoltaic device composed of donor and acceptor materials. The thickness of the active layer is 100 nm. The top and bottom are connected to the anode and cathode, respectively.

The horizontal length of the microstructure is about 1000nm. This allows analysis of a wide range of morphological feature types on the photovoltaic behavior of the device. The active layer is composed of P3HT as the electron-donating polymer and PCBM as the electron-acceptor (see Fig. 3.1). The P3HT:PCBM system has been extensively investigated due to its optimal HOMO-LUMO gap, good charge mobilities, and ease of manufacturability [1, 70, 71, 4]. In this class of devices light is absorbed by the electron donor to generate excitons. [6] To accurately represent this feature, the exciton generation is limited to the donor region. Light intensity decays with depth due to absorption. The resultant exciton generation rate is shown in Fig. 3.5 (b). As the light is shining through the transparent anode at the top of the active layer, exciton

[6] This is usually the case. However, some electron acceptors can also absorb light to generate excitons, eg., $PC_{71}BM$ [72]

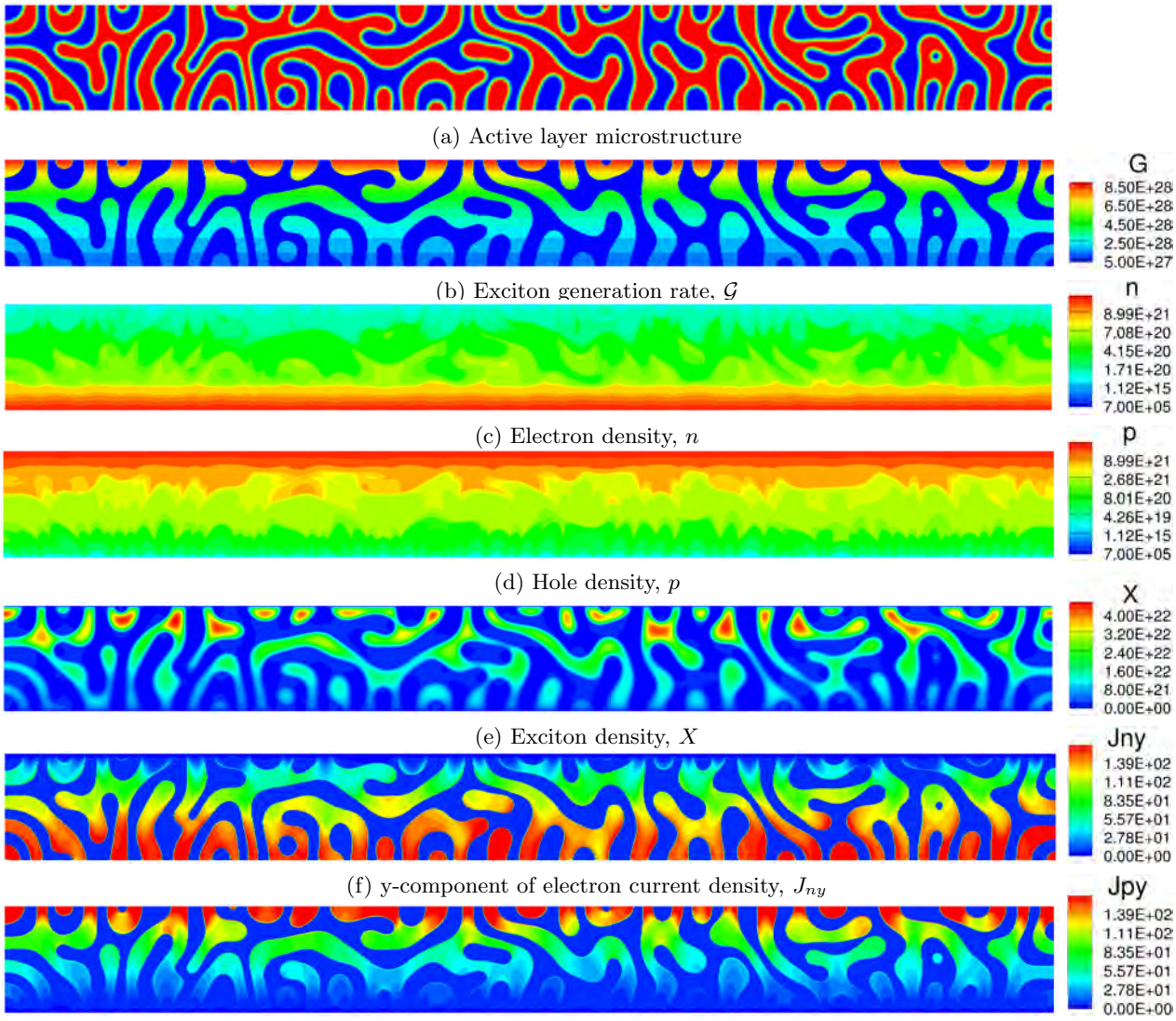

(a) Active layer microstructure

(b) Exciton generation rate, $\mathcal{G}$

(c) Electron density, n

(d) Hole density, p

(e) Exciton density, X

(f) y-component of electron current density, J_{ny}

(g) y-component of hole current density, J_{py}

Figure 3.5: Cross-section of the active layer of realistic polymer photovoltaic device

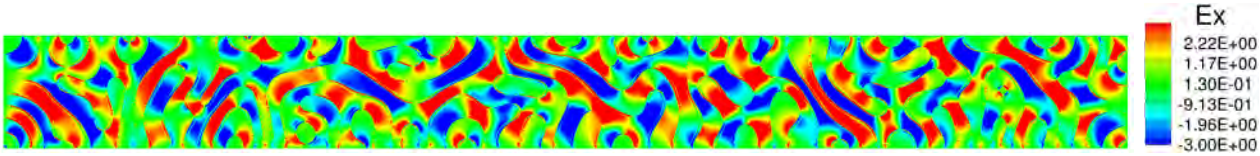

(a) x-component, Ex

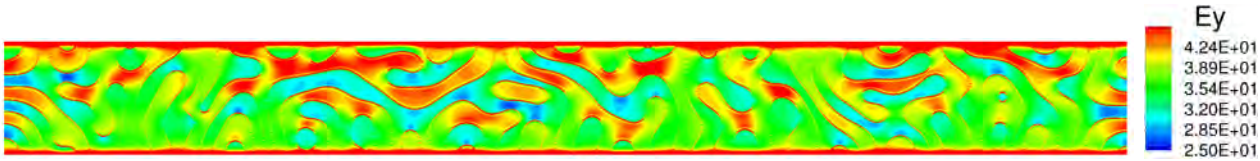

(b) y-component, Ey

Figure 3.6: Electric field distribution

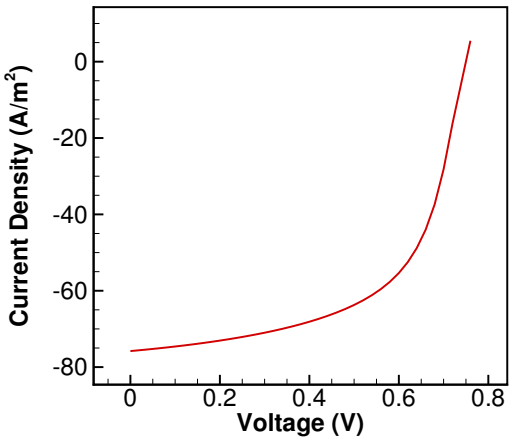

Figure 3.7: Current-voltage characteristic plot.

generation rate $\mathcal{G}$ is maximum near the anode.

We consider the effect of the random and highly inter-penetrating structure of the DA interface on the distribution of excitons, charges and electric field at short circuit conditions.

The ohmic boundary conditions results in maximum electron and hole densities at cathode and anode, respectively (Fig. 3.5 (c) and (d)). The electron density decreases from cathode to anode throughout the domain, but the decrease is much more pronounced in the donor than acceptor region. Similarly, hole density values drops from anode to cathode with a greater rate of decrease in acceptor region.

X is maximum in the inner regions of donor material and its value goes to zero while approaching the interface where the excitons dissociate into free charges. An exponential reduction in the incident light available for absorption along the thickness of the active layer results in higher exciton density near the anode at top.

Figs. 3.5 (f) and (g) show the contour of the electron and hole current densities components normal to the electrodes. The electron current-density (Fig. 3.5 (f)) is negligible in the donor region and increases in the acceptor region while going from anode to cathode. A similar effect is observed with hole current-density (Fig. 3.5 (g)), where maximum values are observed in donor-material close to anode. The electrons are observed to be more dispersed towards the center of the active layer than the holes. This is due to greater likelihood of exciton dissociation near anode at top of the domain. The holes generated at the top of active layer drift upwards towards the anode, while the region in the bottom half remains largely hole free. But electrons created at the top of the domain drift downward towards the cathode and hence are more widely distributed along the thickness.

The spatial variation of electron and hole concentrations results in variation of electric field in the x-direction. Fig. 3.6 (a) shows the x-component of electric field with regions of positive values in acceptor material and negative values in donor material which are the electron and hole transporting media, respectively. The y-component of the electric field (Fig. 3.6 (b)) is an order of magnitude larger than the x-component. The relative variation of the y-component across different materials is less pronounced than the x-component due to the potential created by the difference in work functions of the electrodes. Moreover, a larger value of y-component

of the electric field can be seen in the electron rich acceptor regions compared to donor regions. Hence the spatial variation of charge densities across different materials results in variation in electric field, but the effect is more visible for the x-component than the y-component as the internal potential dominates.

Fig. 3.7 shows the current-voltage characteristic plot obtained by simulating the morphology shown in Fig. 3.5 (a) over a range of applied voltages. Table B.1 in the appendix lists the values used for the various parameters involved in the simulation. The current-voltage curve shown here is similar to typical experimentally obtained curves for P3HT-PCBM based systems [73, 74].

3.4.2 Idealized 2D morphology

This section analyses the electrical properties of a sawtooth morphology with device dimensions, feature size and interface area identical to the realistic morphology analyzed in the previous section. This provides a means to assess the performance of a realistic heterogeneous polymer solar cell against an idealized morphology.

Fig. 3.8 (a) shows a sawtooth morphology with 35 teeth each of donor and acceptor. The device dimensions are maintained same as that of Fig. 3.5 (a). The number and height of teeth is calculated to get an average feature size of 15 nm and the same interface area .The material parameters and simulation settings are same as that for realistic morphology simulation.

The charge densities (Fig. 3.8 (c) and (d)) are observed to be maximum at the respective electrodes (anode for holes and cathode for electrons) and decrease towards the opposite electrode. Away from the electrodes, the maximum values of charge density are found near the DA interface. As shown in Fig. 3.8 (e), maintaining an exciton generation rate distribution similar to realistic morphology case gives an exciton density distribution with maximum values in the donor region lying between the anode and DA interface.

Fig. 3.9 (a) shows the x-component of the electric field calculated at short-circuit conditions. This picture is similar to the results presented by Buxton and Clarke (2007) [3]. Similar to realistic morphology case, the y-component (Fig. 3.9 (b)) of electric field is an order of magnitude larger than the x-component.

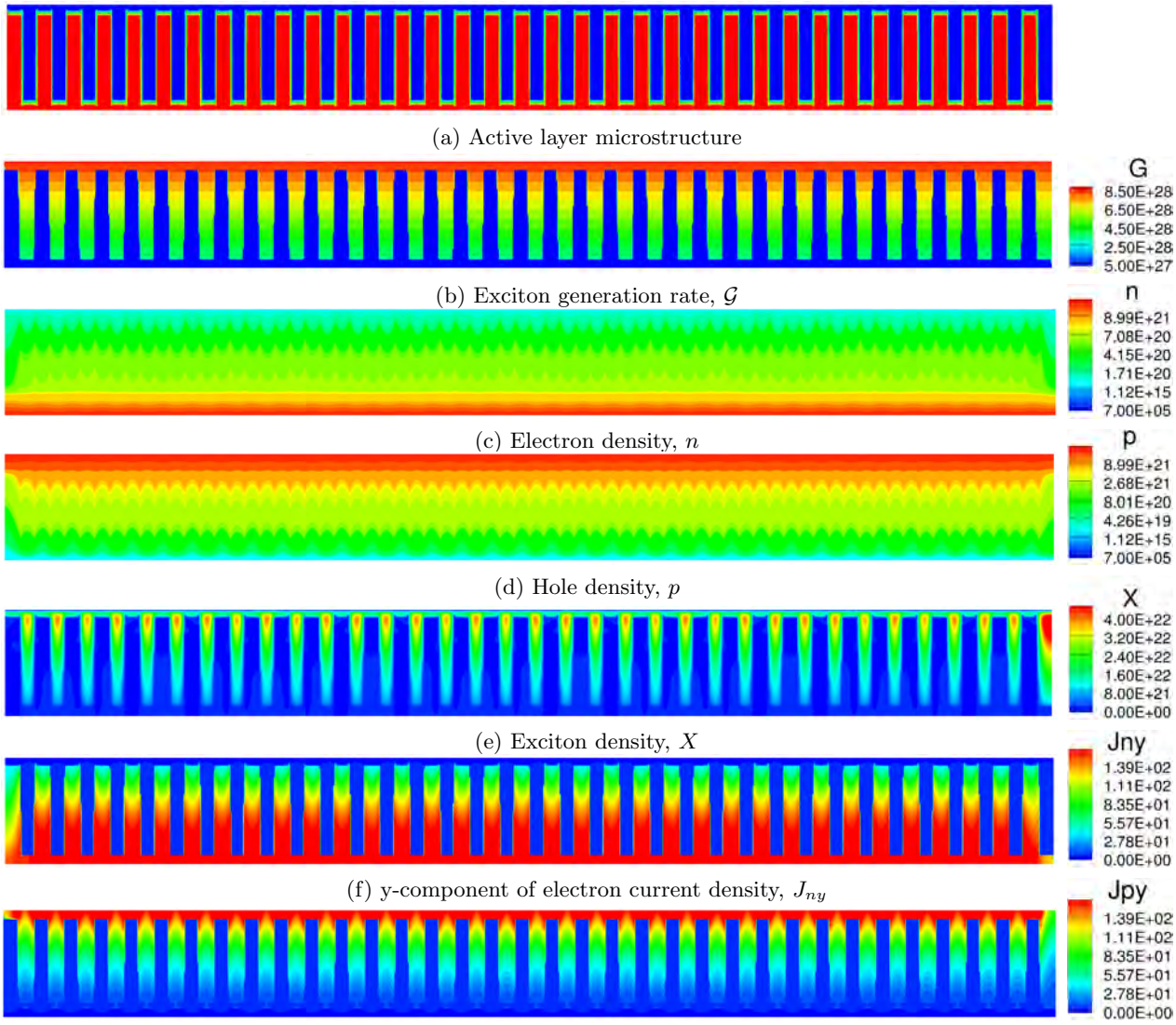

(a) Active layer microstructure

(b) Exciton generation rate, $\mathcal{G}$

(c) Electron density, n

(d) Hole density, p

(e) Exciton density, X

(f) y-component of electron current density, J_{ny}

(g) y-component of hole current density, J_{py}

Figure 3.8: Cross-section of the active layer of an 'idealized' polymer photovoltaic device

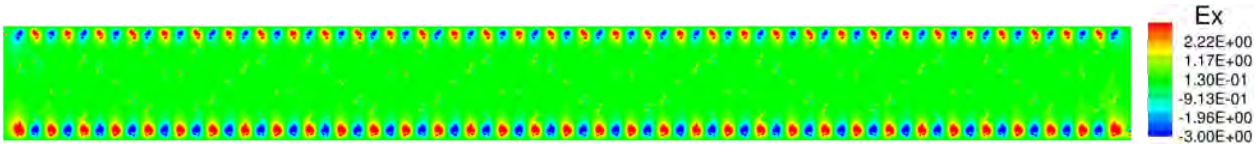

(a) x-component, Ex

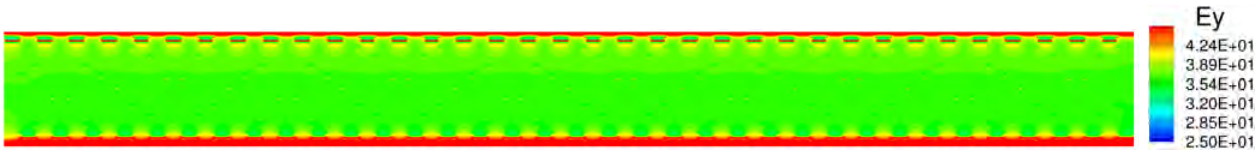

(b) y-component, Ey

Figure 3.9: Electric field distribution

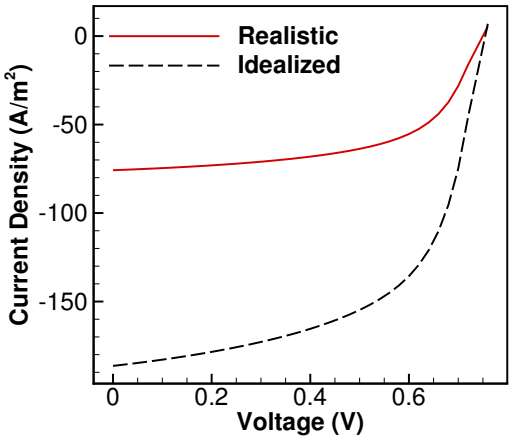

Figure 3.10: Comparison of the current-voltage plot of realistic and idealized morphologies.

The comparison of current density distribution plots for the realistic morphology (Fig. 3.5 (f), (g)) and idealized morphology (Fig. 3.8 (f), (g)) clearly reveals the superiority of the sawtooth structure which, unlike the heterogeneous structure, allows all the charges generated at the DA interface to be collected at the electrodes. Additionally, full contact of donor material with anode and acceptor with cathode augments the charge collection process even more. Fig. 3.10 highlights this difference in performance between sawtooth and realistic device structures.

In order to further tune the realistic device morphologies to obtain high short circuit current densities, we investigate the effect of gradual increase in the feature size while maintaining the same blend volume fraction, on the sub-processes involved in current generation process.

3.4.3 Effect of interfacial area

In this section, we study the effect of systematically changing the interface area and in-turn the feature size of the devices on photovoltaic properties. A similar study delineating the effect of increasing interfacial length on the current density was undertaken by Buxton and Clarke (2007, [3]).[8]

We consider realistic device morphologies as shown in Fig. 3.11 [9] for the present analysis. The different morphologies shown in Fig. 3.11 show variation in a) interfacial area, b) feature size and c) electrode contact area (acceptor with cathode and donor with anode) simultaneously. Increase in interfacial area corresponds to decrease in feature size. The electrode contact area remains relatively unchanged, as the volume fraction of each material in the blend is same. Large interface area would result in greater opportunity for the excitons to dissociate. However, it also deteriorates the charge transport due to high intertwining of pathways and greater number of isolated islands and dead-ends.

The material and simulation parameters are identical to the previous section. Fig. 3.12 shows the current-voltage characteristic curves obtained for the morphologies shown in Fig. 3.11.

[8] This seminal work [3] investigated regular sawtooth morphologies with direct pathways for charges to the electrodes. The present study extends it to include convoluted morphologies with bottlenecks and cul-de-sacs.

[9] These microstructures are obtained by solving the morphology evolution problem using the Cahn-Hilliard equations, corresponding to a DA blend ratio of 1:1 with material parameter χ=2.2. Refer [21, 75] for more details.

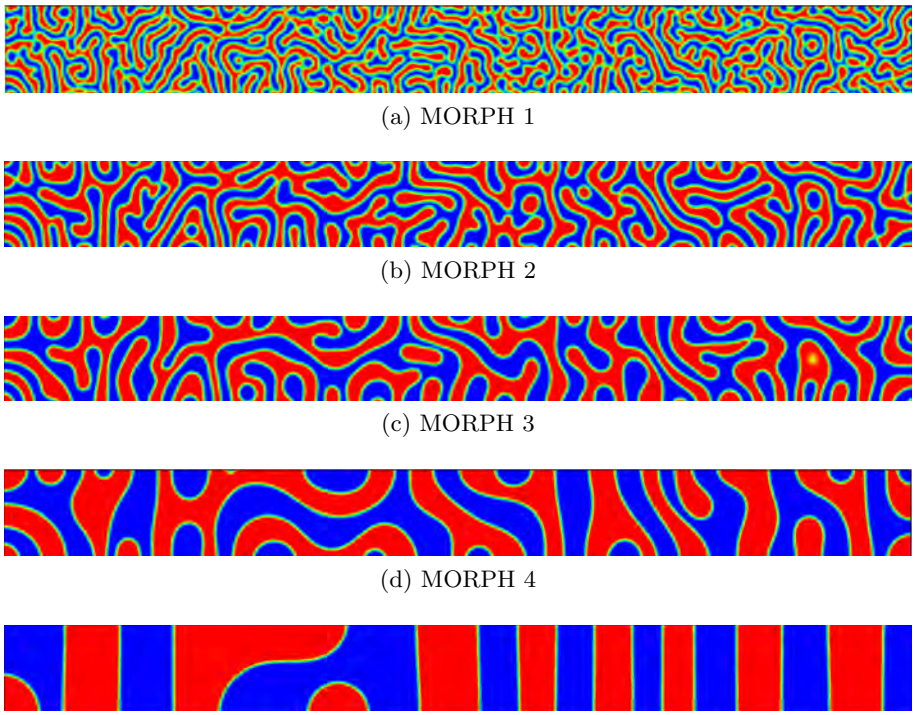

(a) MORPH 1

(b) MORPH 2

(c) MORPH 3

(d) MORPH 4

(e) MORPH 5

Figure 3.11: Morphologies with gradual variation in interfacial area

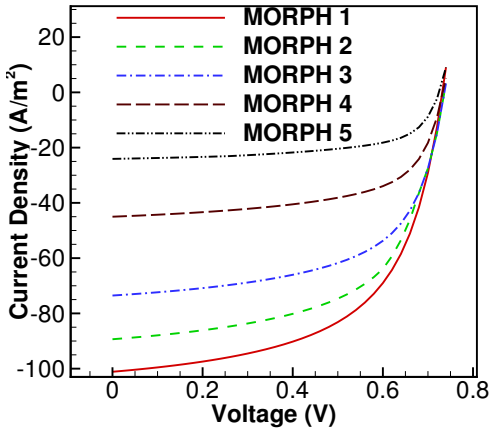

Figure 3.12: Current-voltage characteristic plot for the morphologies shown in Fig. 3.11

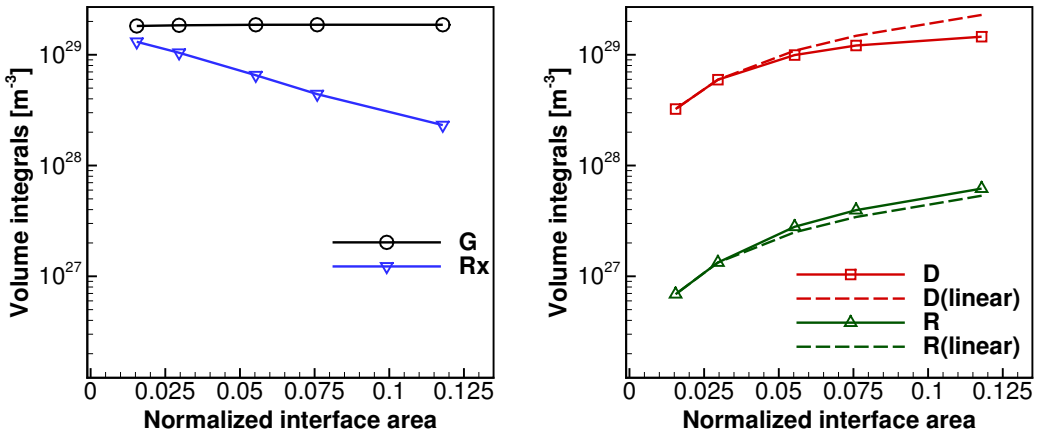

Figure 3.13: Effect of interface area on the integral of (a) exciton generation rate $\mathcal{G}$, exciton relaxation rate $\mathcal{R}_X$, and (b) exciton dissociation rate $\mathcal{D}$, charge recombination rate $\mathcal{R}$, over the domain at short circuit condition. The dashed lines in (b), which represent linear increase, are curved on account of being plotted on a semi-log plot.

This shows that the morphology with highest interfacial area has the best performance suggesting a dominant role played by exciton dissociation rate in deciding the final performance. To further understand the role played by the DA interface, the relative effect of interfacial area on the subprocesses involved in light absorption to charge collection stage (generation,dissociation and relaxation of excitons, charge recombination) is analyzed. Fig. 3.13 shows increasing interfacial area plotted against the integral of $\mathcal{G}$, $\mathcal{R}_X$, $\mathcal{D}$ and $\mathcal{R}$. The overall exciton generation rate $\mathcal{G}$ (Fig. 3.13 (a)) remains relatively unchanged for different interface areas. This is due to using the same device dimensions and material volume-fractions. Fig. 3.13 (b) shows a sublinear increase in exciton dissociation rate with increase in interfacial area suggesting a reduced increase in $\mathcal{D}$ for any further increase in interfacial area. A reverse trend is observed for exciton relaxation rate $\mathcal{R}_X$. The charge recombination $\mathcal{R}$, which limits the device performance, shows an almost linear increase with interface area.

The increase is charge recombination rate $\mathcal{R}$ is overshadowed by increase in exciton dissociation rate and decrease in exciton relaxation rate $\mathcal{R}_X$, thereby resulting in a net increase in device performance. The charge recombination increases super-linearly with interface area, whereas the increase in exciton dissociation is sub-linear, which would lead to diminishing

performance improvements with further increase in interface area.

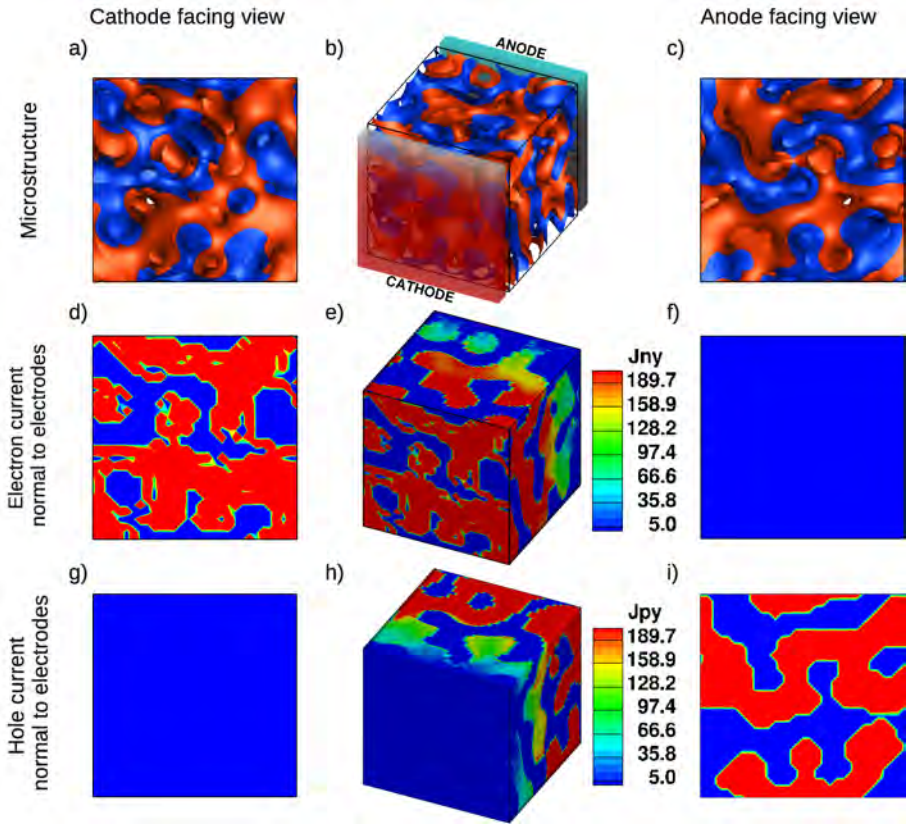

Figure 3.14: Electron and hole current distributions for real morphology. Row 1, 2 and 3 shows various views of the microstructure, electron current density and hole current density respectively.

3.4.4 Three dimensional simulation

We showcase the capability of the framework to simulate 3D realistic morphologies with Figures. 3.14 and 3.15. Figure. 3.14 (b) shows the morphology of the device used in this study. The calculated electron and hole current densities are shown in Figure. 3.14 (e) and (h) respectively. The cathode and anode facing views are also included to aid visualization. Figure. 3.15 shows the corresponding morphology and current density plots for ideal morphology. As can be observed from Figures. 3.14 and 3.15, the current density for ideal morphology is much larger than that for real morphology due to better charge transport pathways and electrode

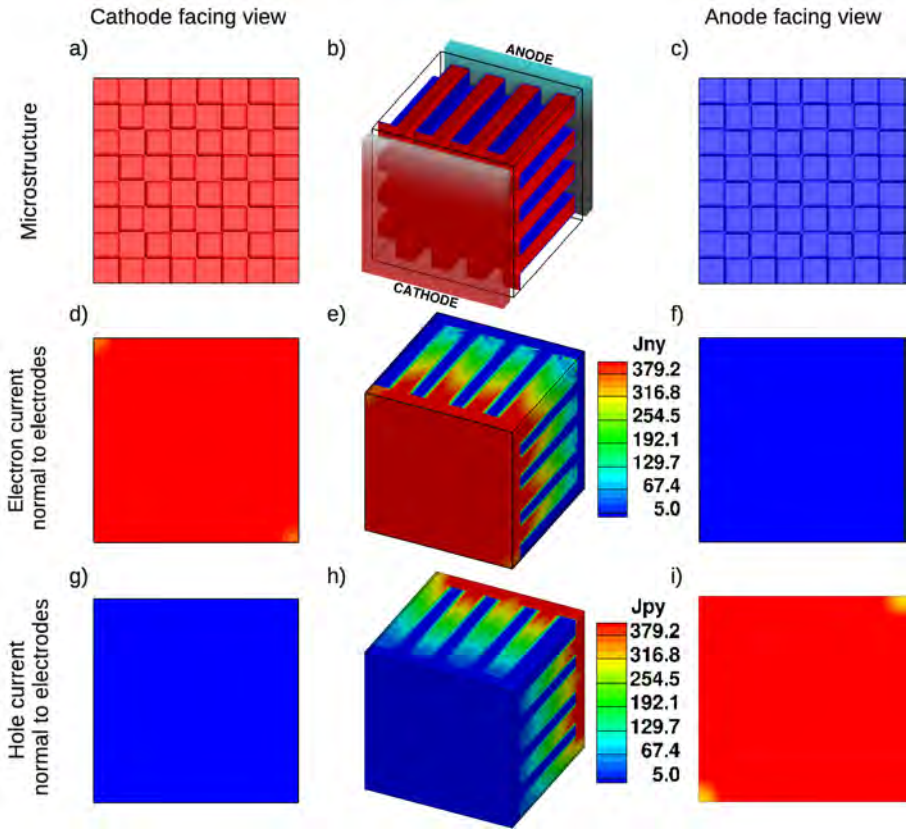

Figure 3.15: Electron and hole current distributions for ideal morphology. Row 1, 2 and 3 shows various views of the microstructure, electron current density and hole current density respectively.

contact area (cathode contact area for acceptor and anode contact area for donor).

For real morphology, some features which appear as isolated 'islands' in two dimensions may have direct pathways to electrode in 3D, and in general, 3D structures may provide more number of pathways from charge generation site to charge collection site than an equivalent 2D device structure. Hence 3D simulation helps visualize and analyze the charge transport properties which are not easily seen to 2D simulations.

3.5 Conclusions and future work

The ability of correlate morphological features with each stage of the current generation process will be immensely helpful to minimize performance losses. Quantification of morpho-

logical effects on performance based on experimental investigation is very time consuming and resource intensive or prohibitively costly in case of a high-throughput study on a range of microstructures. This necessitates development of a computational framework that can be used as a virtual characterization tool for detailed analysis.

We showcase an efficient, dimensionally-independent, finite-element-based framework for high-throughput interrogation of realistic percolating microstructures. **(1)** A parallel implementation of the framework is showcased and results from scalability analysis are shown. **(2)** The modular structure of the framework enables quick evaluation of various quantities (e.g. $\mathcal{D}$, $\mathcal{R}_{[X]}$, J) over the entire domain. **(3)** A comparison of a typical percolating and idealized sawtooth type microstructure revealed a short circuit current gain of more than twice for the later. **(4)** We also investigated the effect of feature size on the photovoltaic properties of heterogeneous interpenetrating microstructures. This helped us understand the relative affect feature sizes on exciton dissociation and charge recombination. The increase in exciton dissociation due to increase in interfacial area tapers of for a feature size of around 10nm at which point charge recombination starts to play a dominant role.

Future work consists of analyzing the charge transport improvement due to electrode surface engineering [76]. Other avenues of work include predicting 3D optimal morphologies for maximized charge generation and transport.

Acknowledgments

B.G. and H.K.K. were supported in part by NSF PHY-0941576, NSF CCF-0917202 and an NSF CAREER Award. We thank Olga Wodo for the images of active layer microstructures and discussions.

CHAPTER 4. SENSITIVITY ANALYSIS OF CURRENT GENERATION IN ORGANIC SOLAR CELLS – COMPARING BILAYER, SAWTOOTH AND BULK HETEROJUCTION MORPHOLOGIES

A paper published in *Solar Energy Materials & Solar Cells*

Hari K. Kodali and Baskar Ganapathysubramanian

Abstract

Organic solar cells (OSC) show great potential as a low-cost energy source. In addition, their mechanical flexibility allows the added advantage of use on a wide variety of surfaces. In recent years, progress in experimental strategies and modeling approaches have enabled enhancing the power conversion efficiencies of OSC. In particular, simulation based analysis have played a significant role in improving our understanding of the charge transport phenomena in the active layer of these devices. The excitonic drift-diffusion (EDD) model has been used widely to simulate the generation and transport properties of bulk heterojunction (BHJ) solar cells. The EDD model – which is derived from Boltzmann transport equations – is dependent on a number of input parameters such as (1) material properties (mobility, permittivity), (2) operating conditions (illumination, device thickness) and (3) active layer morphology.

A comprehensive sensitivity analysis of the short-circuit current, J_{sc}, to the input parameters is performed. This helps in rank ordering the input parameters and operating conditions – by strength and relevance – on their impact on J_{sc}. We particularly focus our investigations on understanding how the active layer morphology affects the sensitivity of J_{sc}. To accomplish this we analyze three classes of morphologies: bilayer, BHJ, and sawtooth. The results show significant differences in sensitivities between BHJ, sawtooth and bilayer morphologies. Short-

circuit current in BHJ structure shows higher sensitivity to material properties than either sawtooth and bilayer structure, suggesting the necessity for finer control of material properties to counteract the increased disorder in the active layer morphology. The electrode current is found to be most sensitive to illumination intensity for all three morphologies. We report some interesting trends that may help choose the most sensitive parameters to vary for designing OSC's with better performance.

4.1 Introduction

Organic solar cells allow the use of low-temperature roll-to-roll, and hence low-cost manufacturing [20]. Mechanical flexibility is the other major advantage of these devices which makes them so attractive. Huge progress has been made in the last few years towards improving the problem of low efficiencies associated with organic solar cells. This advancement (highest reported value under laboratory conditions is 9% [77]) is made possible by experimental and numerical investigations of the operating mechanisms and device structure optimization. Numerical simulations not only help enhance performance through device optimization [78], but also help improve the fundamental understanding of the underlying charge transfer processes in the active layer which is not easily accessible to experimental tools [3, 79, 80, 81, 82].

Monte-Carlo method based microscopic models [45, 46, 47] have been utilized to probe the effect of morphology on the generation, mobility and recombination of charge carriers. But the high computational cost associated with microscopic simulations hampers their use for large scale simulations or in high-throughput analysis of OSC. A computationally efficient alternative in the form of excitonic drift diffusion model [9, 10, 83, 79, 11, 12, 13] has been used successfully for simulating the charge transport properties of organic photovoltaics. With wide use of EDD equations it has become increasingly imperative to do a detailed investigation to understand how the material properties and operating conditions (inputs to EDD model) effect the device performance (output from EDD model). When input variables are not known or can be changed, sensitivity analysis informs us about the effect of a small change in input parameters on the output from EDD model. Sensitivity analysis can also help in ordering the inputs by their effect on performance of organic solar cells. This facilitates decision making

process when one is presented with the option of modifying one among a number of competing input parameters, thus providing guidance on process optimization. Also, it would contribute towards increasing the understanding and credibility of the EDD model and making the results more persuasive. In recent years, such sensitivity analysis has been used extensively for a variety of systems like ecological models [84], chemical models [85], structural systems [86], pharmacokinetic models [87] and fluid flows [88].

For OSC devices, sensitivity analysis of 1D homogeneous model was undertaken by Häusermann et. al. (2009) [89], wherein the sensitivity to input parameters for a range of device thicknesses, input voltages and time during turn-on was studied. The input parameters selected were electron and hole mobilities μ_n, μ_p, recombination efficiency r_{eff}, exciton pair separation a, and decay rate k_f. The pair separation a was found to have the highest influence on the short-circuit current.

However, experimental evidence suggests that the active layer morphology is an important factor determining the performance of organic solar cells [36, 37, 38], which indicates significant effect of morphology on the sensitivity of J_{sc}. This study aims to do an in-depth sensitivity analysis of a morphology dependent EDD model for organic solar cells. We analyze the sensitivity of the short-circuit current to the a) material properties (electron mobility μ_n, hole mobility μ_p, acceptor dielectric constant ϵ_A and donor dielectric constant ϵ_D), b) device thickness (L), and c) operating condition (illumination intensity Γ) under three different morphologies. To investigate the effect of the transition from ordered to disordered morphologies on sensitivity, we study bilayer, sawtooth and BHJ based devices. As the sensitivity to a specific input parameter may be dependent on the values of other input parameters, we compute the sensitivity to the inputs for a range of values of all input parameters.

4.2 Method

4.2.1 Model

In order to determine the short-circuit current density output from the active layer of a BHJ device, we use the EDD model [79] as described below.

$$\nabla \cdot (\epsilon \nabla \phi) = q(n - p) \tag{4.1}$$

$$\nabla \cdot \mathbf{J_n} = -qff'\mathcal{D}_{[\nabla\phi,X]} + qff'\mathcal{R}_{[n,p]} \tag{4.2}$$

$$\nabla \cdot \mathbf{J_p} = +qff'\mathcal{D}_{[\nabla\phi,X]} - qff'\mathcal{R}_{[n,p]} \tag{4.3}$$

$$\mathbf{J_n} = -qn\mu_n \nabla\phi + qV_t\mu_n \nabla n \tag{4.4}$$

$$\mathbf{J_p} = -qp\mu_p \nabla\phi - qV_t\mu_p \nabla p \tag{4.5}$$

$$\nabla \cdot (V_t\mu_X \nabla X) - ff'\mathcal{D}_{[\nabla\phi,X]} - \mathcal{R}_{[X]} = -\mathcal{G} - ff'\mathcal{R}_{[n,p]} \tag{4.6}$$

Equations (4.1-4.6) are solved to obtain the electron (n) and hole (p) densities, and electrostatic potential ϕ. The solution thus obtained is used to determine the electron and hole current densities, $\mathbf{J_n}$ and $\mathbf{J_p}$ respectively. Here, q is the elementary charge.

Morphology dependent parameters: The values of dielectric constant ϵ, electron mobility μ_n and hole mobility μ_p are dependent on morphology, i.e. ϵ, μ_n and μ_p at any location in the active layer depends on the type of material at that location. f and f' denote the parameters which are used to track the donor:acceptor (DA) interfaces. f is 1 at interface, 0 elsewhere. To identify the interfaces with pathways to electrodes – for both electrons and holes – we use parameter f'. f' is 0 at interfaces without direct connection to either cathode (for electrons) or anode (for holes). These interfaces are associated with either of the donor and acceptor regions forming a cul-de-sac. f' is 1 elsewhere.

The exciton generation, diffusion and dissociation are represented by Eqn. (4.6). $\mathcal{G}$ and $\mathcal{D}_{[\nabla\phi,X]}$ denote rate of exciton generation and dissociation, respectively. Exciton relaxation rate is denoted by $\mathcal{R}_{[X]}$. The recombination of charges is given by $\mathcal{R}_{[n,p]}$. The expressions for

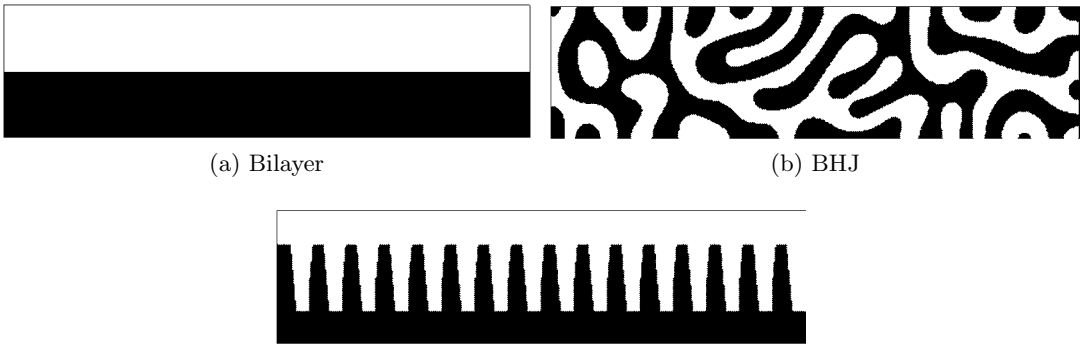

(a) Bilayer (b) BHJ

(c) Sawtooth

Figure 4.1: Morphologies used for the sensitivity analysis. Dark region represents acceptor and lighter region is donor.

$\mathcal{D}_{[\nabla\phi,X]}$, $\mathcal{R}_{[n,p]}$, $\mathcal{G}$, $\mathcal{R}_{[X]}$ are:

$$\mathcal{D}_{[\nabla\phi,X]} = k_d X \tag{4.7}$$

$$\mathcal{R}_{[n,p]} = \gamma_r np \tag{4.8}$$

$$\mathcal{G} = \alpha\Gamma exp(-\alpha x) \tag{4.9}$$

$$\mathcal{R}_{[X]} = X/\tau_X \tag{4.10}$$

where Γ denotes illumination intensity and x is the distance from the illumination site. Here the exciton generation rate $\mathcal{G}$ is approximated using Beer-Lambert Law. The expression for Langevin recombination parameter γ_r used in this study is $\gamma_r = \frac{q}{\epsilon}(\mu_n + \mu_p)$. The dissociation rate constant k_d, absorption coefficient α, average lifetime of exciton τ_X can be found in Kodali and Ganapathysubramanian (2012) [79]. We use ohmic boundary conditions at the electrode boundaries and homogeneous Neumann condition for the rest of the boundaries. The equations (4.1-4.6) are solved using finite element method [79]. We utilized the National Center for Supercomputing Applications (NCSA)-ABE cluster which is part of XSEDE, to analyze the large number of test cases involved with a detailed sensitivity analysis.

4.2.2 Morphologies

The sensitivity analysis is performed on three OPV devices with structures shown in Figure. 4.1. The cross-section of the active layer shown in Figure. 4.1 consists of 1:1 volume

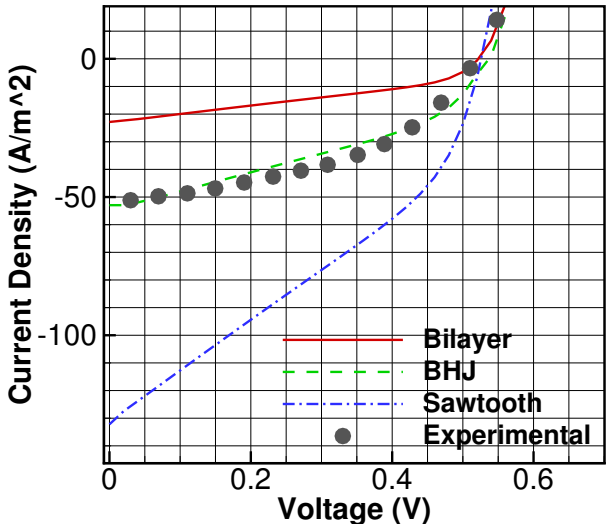

Figure 4.2: Current-voltage characteristic plots for the bilayer, sawtooth and BHJ morphologies compared with result from experiment [7]

ratio of poly(3-hexylthiophene):[6,6]-phenyl-C_{61}-butyric acid-methyl ester (P3HT:PCBM). Figure. 4.1(b) shows a typical BHJ morphology with interpenetrating electron donor (P3HT) and acceptor (PCBM) phases. Figures. 4.1(a) and 4.1(c) show bilayer and sawtooth structures. The bottom of the active layer is connected to cathode and top to anode. Figure. 4.2 shows the current-voltage characteristic curves for the representative values of input parameters P shown in Table. 4.1. We note that the values of the relative dielectric constants (Table. 4.1) in the acceptor and donor region correspond to the real part of the complex permittivity.

4.2.3 Sensitivity analysis

The EDD model described in Section. 4.2.1 is used to determine the dependence of short-circuit current J_{sc} on electron and hole mobilities (μ_n, μ_p), donor and acceptor dielectric constants (ϵ_A, ϵ_D), active layer thickness (L) and photon flux (Γ). We define the sensitivity of J_{sc} to input parameter P, as

$$Sensitivity_{[P]}(J_{sc}) = \frac{\partial J_{sc}}{\partial P} \tag{4.11}$$

where P can be μ_n, μ_p, ϵ_A, ϵ_D, L or Γ. Note that the value of Γ can be $\sim$30 orders of magnitude larger than other parameters (see Table. 4.1). This results in $\sim$30 order of magnitude difference

in the values of $Sensitivity_{[\Gamma]}(J_{sc})$ and sensitivity of J_{sc} to μ_n, μ_p, ϵ_A, ϵ_D, L. Hence we define a normalized form of sensitivity as,

$$\widehat{\delta_P J_{sc}} = \frac{\partial J_{sc}/J_{sc}}{\partial P/P} \tag{4.12}$$

This enables comparison of sensitivity to all the parameters irrespective of the magnitude of the physical values. All subsequent mention of sensitivity refer to normalized sensitivity.

Parameter, P	Symbol	Numerical value	Units
1. Electron mobility	μ_n	1.0×10^{-7}	$m^2V^{-1}s^{-1}$
2. Hole mobility	μ_p	1.0×10^{-7}	$m^2V^{-1}s^{-1}$
3. Donor relative dielectric constant	ϵ_D	3.0	$--$
4. Acceptor relative dielectric constant	ϵ_A	3.0	$--$
5. Active layer thickness	L	1.0×10^{-7}	m
6. Illumination intensity	Γ	4×10^{21}	W/m^2

Table 4.1: Representative values of the input parameters P.

4.3 Results and discussion

We study the response of the three devices as light is incident from the top through the transparent anode onto the active layer. The absorption of photons and consequent exciton generation is restricted to the donor regions, as it is comparatively negligible in the acceptor region for P3HT:PCBM based devices [28]. The absorption depth is taken as 50nm [90]. The electron and hole mobilities are assumed to be independent of the electric field in this study [91, 92].

Figure. 4.3 shows the comparison of the effect of varying parameters P on J_{sc} for the three device morphologies under consideration on a lin-log plot. The mobilities (Figures. 4.3(a),(b)) and dielectric constants (Figures. 4.3(c),4.3(d)) have a comparatively small effect on J_{sc}. Photon flux Γ and active layer thickness L in Figures. 4.3(e) and 4.3(f) show a relatively higher impact. Among the three structures considered, BHJ structures show greatest variation in J_{sc} due to change in the permittivity (Figures. 4.3(c),4.3(d)). *This may be due to increased bending of the electric field lines around the donor:acceptor interfaces, thereby assisting charges*

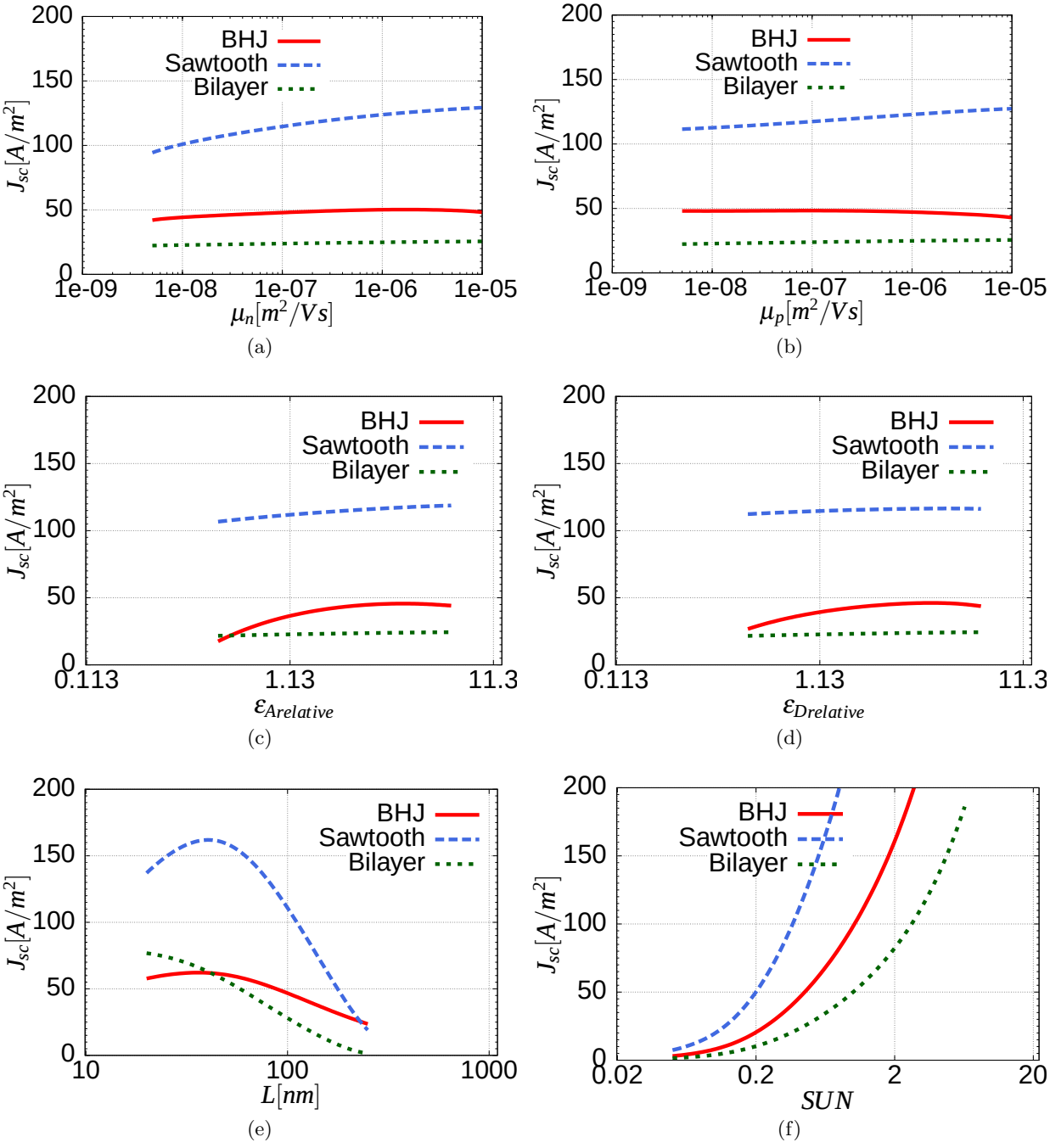

Figure 4.3: J_{sc} plotted against (a) μ_n, (b) μ_p, (c) ϵ_A, (d) ϵ_D, (e) L, and (f) Γ (in terms of number of Suns) for BHJ, Sawtooth and Bilayer morphologies.

to bypass interface recombination while moving towards the electrodes [93]. BHJ and sawtooth structures show maximum J_{sc} when the active layer thickness L is equal to the absorption depth (50nm) and any further increase in thickness leads to negligible increase in charge generation while significant reduction in charge transport and collection (Figure. 4.3 (e)). *Bilayer devices show a monotonic decrease in J_{sc} with increasing L due to change in the distance of the donor:acceptor interface from the location of greatest exciton generation, i.e. the P3HT region closest to anode.* Figure. 4.3 (f) shows a rapid increase in J_{sc} with increase in Γ.

As given in Table. 4.1, the ratio of representative values of electron:hole mobilities as well as donor:acceptor dielectric constant is 1:1. The sensitivity of J_{sc} (Figure. 4.4) to different parameters is calculated for a range of each of the parameter values, while keeping all the other parameters at their representative values shown in Table. 4.1. $\widehat{\delta_P J_{sc}}$ is determined by calculating the relative change in J_{sc} for a 10% variation in each of the input parameter P. From Figure. 4.4, it can be inferred that for the representative values of parameters, the sensitivity for BHJ morphology is highest to Γ. As shown in Figure. 4.4 (a)-(d), *sensitivity of J_{sc} to mobilities and permittivities is higher for BHJ structure compared to sawtooth or bilayer structure.* On the other hand, sensitivity of J_{sc} to device thickness L is lowest for BHJ structure (Figure. 4.4(e)). *This suggests greater performance benefit by optimizing thickness of devices with regular structure compared to those with BHJ structure.* The value of $\widehat{\delta_P J_{sc}}$ for BHJ and sawtooth is lowest (Figure. 4.4(e)) when the device thickness L is equal to the absorption depth of 50nm. All three structures show the same sensitivity to Γ, suggesting that all devices - independent of the morphology - benefit equally from increase in illumination intensity.

After comparing the values of $\widehat{\delta_P J_{sc}}$ to each of the parameters P separately for the three morphologies, we analyze the sensitivity of J_{sc} to multiple parameters simultaneously for a range of values of each parameter (Figure. 4.5). $\widehat{\delta_{\mu_n} J_{sc}}$, $\widehat{\delta_{\mu_p} J_{sc}}$, $\widehat{\delta_{\epsilon_A} J_{sc}}$ and $\widehat{\delta_{\epsilon_D} J_{sc}}$ are plotted for a range of values of μ_p, ϵ_D and L (Figure. 4.5) for a device with BHJ morphology. Plots with sensitivity to all the input parameters for Bilayer, BHJ and Sawtooth morphologies are shown in Figures. C.1, C.2 and C.3 in appendix. Figures. 4.5(a),(b) show that as the sensitivity of J_{sc} to ϵ_A and ϵ_D increases with increase in mobilities. On the other hand, sensitivity of J_{sc} to μ_n and μ_p decreases with increase in the values of permittivities. *Hence it is more difficult*

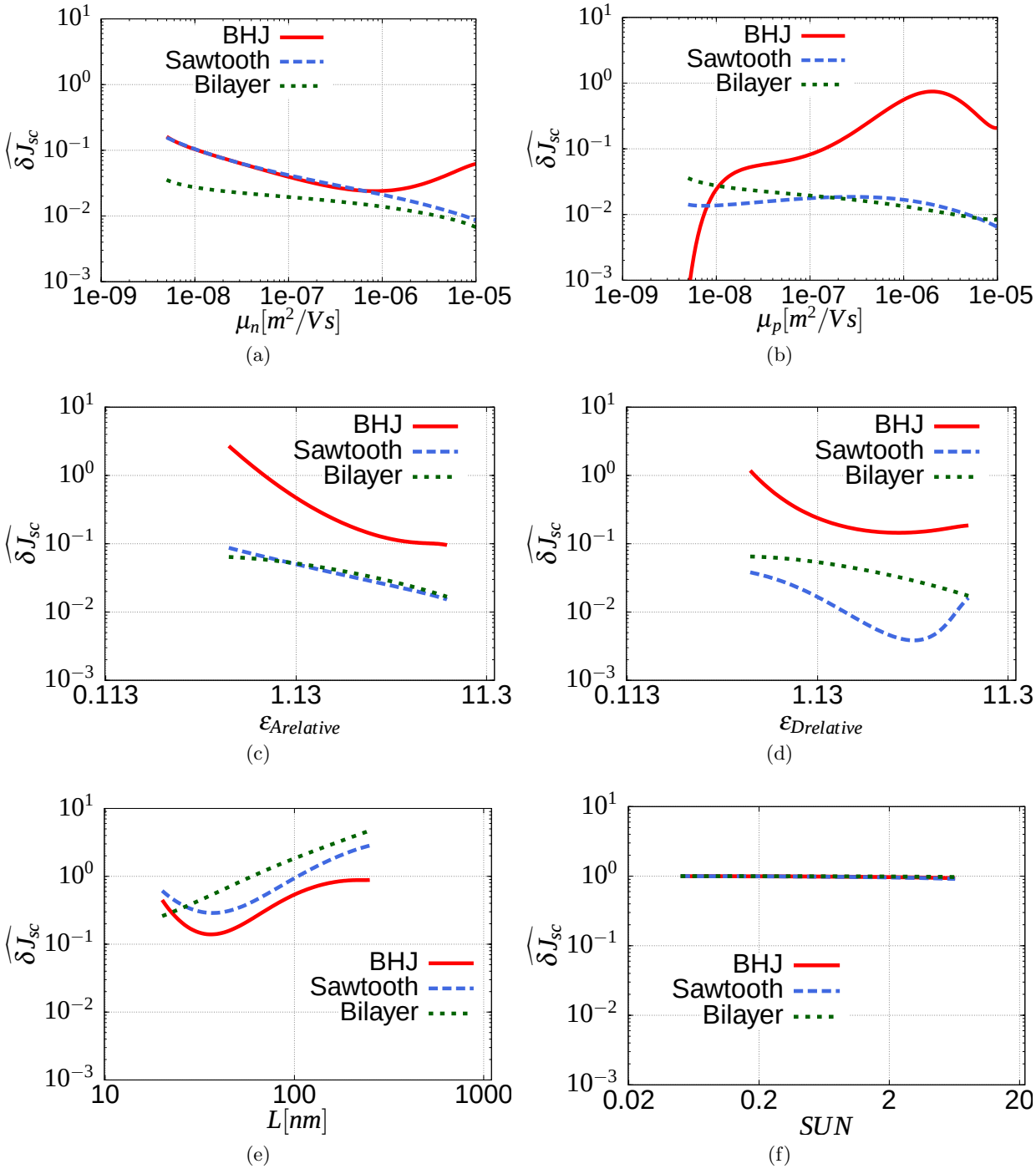

Figure 4.4: Sensitivity of J_{sc} to (a) μ_n, (b) μ_p, (c) ϵ_A, (d) ϵ_D, (e) L, and (f) Γ (in terms of number of Suns) for BHJ, Sawtooth and Bilayer morphologies.

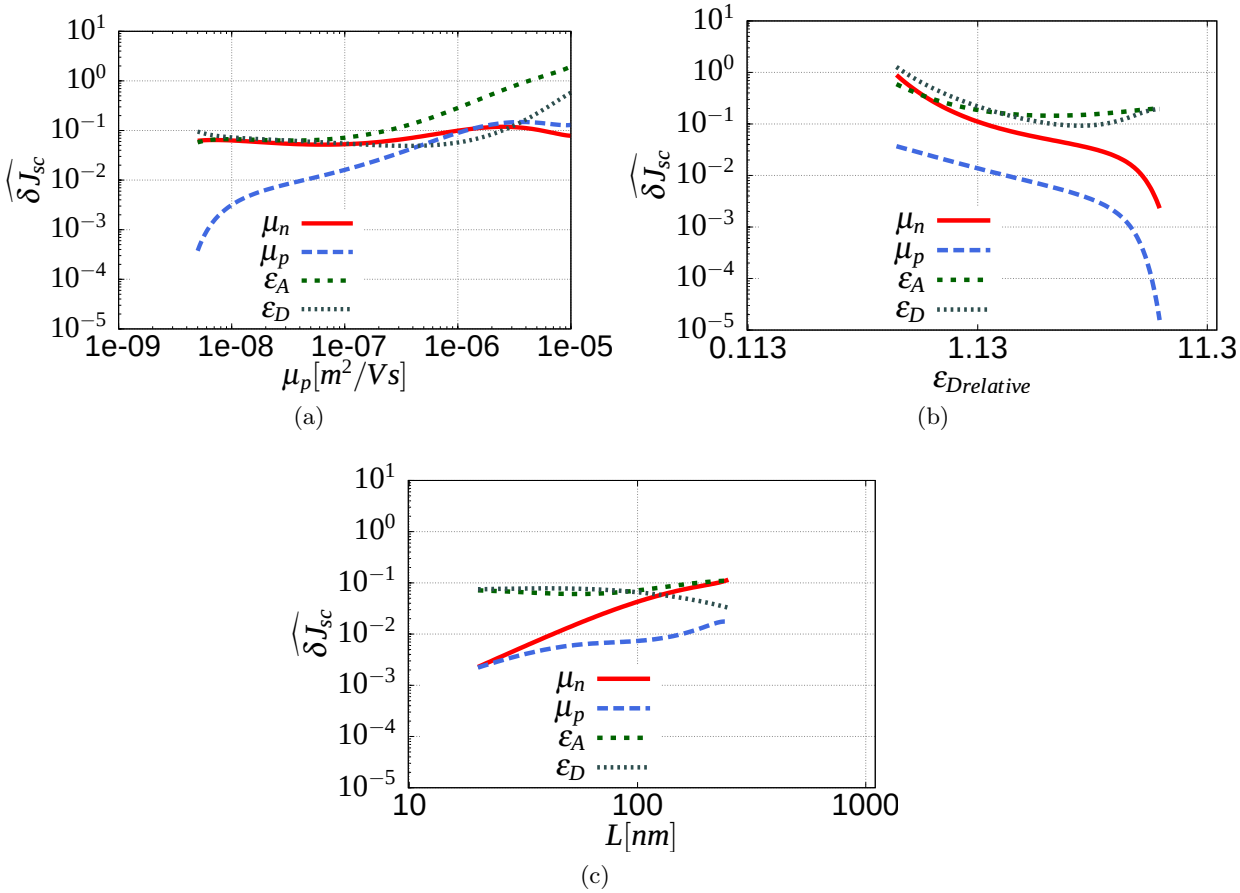

Figure 4.5: Sensitivity of Jsc to different parameters over a range of (b) μ_p, (b) ϵ_D and (c) L for BHJ morphology

to increase the J_{sc} by increasing mobilities of materials with higher dielectric constants. Also, J_{sc} can be increased by making relatively small changes to the permittivities of a material with high carrier mobilities for BHJ devices. $\widehat{\delta_{\mu_n} J_{sc}}$ increases significantly for larger thicknesses. In addition, $\widehat{\delta_{\mu_n} J_{sc}}$ is greater than $\widehat{\delta_{\mu_p} J_{sc}}$ for larger thicknesses, suggesting that the electron mobility, μ_n, becomes a critical factor for thicker devices.

Among $\mu_n, \mu_p, \epsilon_A, \epsilon_D, L, \Gamma$ the short-circuit current is found to be most sensitive to illumination intensity Γ. The values of $\widehat{\delta_\Gamma J_{sc}}$ are closely followed by the sensitivity of short-circuit current to device thickness. $\widehat{\delta_L J_{sc}}$ is also invariant to changes in most of the input parameters, as $\widehat{\delta_\Gamma J_{sc}}$, but shows change when the thickness itself is changed. Short-circuit current plotted against device thickness shows a maximum when L is equal to absorption depth for BHJ and sawtooth structures. At the same thickness, sensitivity to thickness is lowest for these structures. *Hence, optimizing the device thickness (to be close to the absorption depth) is one order more effective in increasing J_{sc} than changing any of the material properties.*

Short-circuit current sensitivity to material properties $\widehat{\delta_{\mu_{n|p}} J_{sc}}$ and $\widehat{\delta_{\epsilon_{A|D}} J_{sc}}$ is higher for BHJ structure compared to sawtooth or bilayer structures. Sensitivity to electron mobility increases significantly for thicker devices and higher illumination intensities. J_{sc} is found to be least sensitive to hole mobility. Sensitivity to electron mobility is shown to be an order of magnitude higher than that to hole mobility for most of the values of the input parameters considered.

4.4 Conclusions

We have performed a morphology dependent sensitivity analysis of the short-circuit current in organic solar cells using the exitonic drift-diffusion equations. Following is an enumeration of some of the insights gained is this study.

1. For materials with higher permittivities, it is difficult to increase J_{sc} by increasing carrier mobilities of devices with BHJ structures (Figure. 4.5(b)).

2. For materials with higher mobilities, J_{sc} can be changed by making relatively small changes to the permittivities of devices with BHJ structures (Figure. 4.5(a)).

3. Greater performance benefit can be achieved by optimizing the thickness of devices with regular (Sawtooth,Bilayer) structure compared to devices with disordered (BHJ) structure (Figure. 4.4(e)).

4. The sensitivity to permittivities is highest for BHJ devices (Figures. 4.4(c), 4.4(d)), which may be due to charge transport assisted by the electric field lines, bent around the donor:acceptor interfaces [79].

5. For relatively thicker devices, electron mobility μ_n is the most critical material property effecting the short-circuit current (Figure. 4.5(c)).

We envision this analysis and the trends reported to be of value to our experimental colleagues for choosing the most sensitive parameters to vary for designing OSC's with better performance.

Acknowledgments

B.G. and H.K.K. were supported in part by NSF PHY-0941576, NSF CCF-0917202 and an NSF CAREER Award. We thank Olga Wodo for the images of BHJ structures. We also thank Prof. Evan Reed (Dept. of Mat. Sci. and Engg., Stanford) for motivating the notion of sensitivity analysis. This work used the Extreme Science and Engineering Discovery Environment (XSEDE), which is supported by National Science Foundation grant number OCI-1053575.

CHAPTER 5. IS A COLUMNAR INTERDIGITATED MORPHOLOHY OPTIMAL FOR ORGANIC SOLAR CELLS ?

Modified from a paper to be submitted to *Physical Review Letters*

Hari K. Kodali and Baskar Ganapathysubramanian

Abstract

Organic solar cells are promising low-cost alternatives [17] to their inorganic counterparts due to lower manufacturing costs [20], higher mechanical flexibility [28], and optical tunability [18]. However, a low power conversion efficiency [94] (PCE) is a bottleneck to their widespread use. It is known that morphology [95] plays a critical role in determining the PCE [37]. Morphology control and tailoring has been the focus of extensive research [38] over the past decade, driven by the hypothesis [6] that morphologies having interdigitated columnar domains will make optimal devices [95]. Here we disprove this hypothesis by computationally discovering a family of morphologies that perform better than the hitherto thought optimal morphology by as much as 25%. This family of morphologies are simply topological perturbations to the interdigitated columnar morphology, thus maintaining most of the features – connectivity and domain sizes – exhibited by the latter. The discovery of a whole class of morphologies with improved performance will have an impact on the field of organic photovoltaic from molecular design and fabrication tailoring to the question of discovering the optimal morphology.

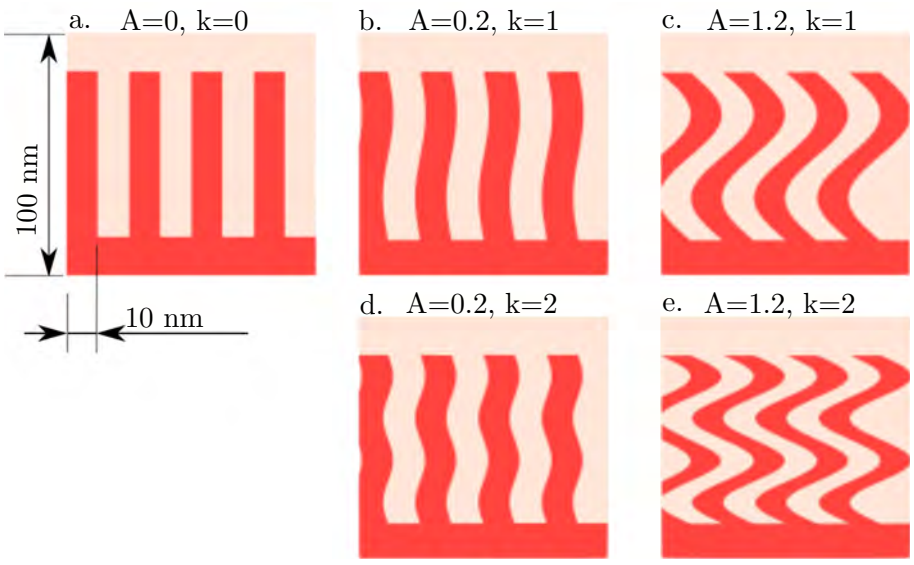

Figure 5.1: A representative set of the family of topological perturbations to the 'standard' columnar morphology (a) with increasing amplitude A (b & c), and wavenumber k (d & e). Here, dark and light colors denote acceptor-rich and donor-rich regions respectively. The value of amplitude A is denoted in terms of the column thickness.

5.1 Introduction

Sustained research over the past decade has improved efficiency of organic solar cells from 1 % to 10.6% [94]. This has been achieved by the development of new materials [30, 31, 32], device designs [33, 34, 35] and morphology control of the active-layer [36, 37, 38]. There is a general consensus that morphologies having interpenetrating columnar domains (Fig. 5.1 a) result in optimal devices [95, 96, 6, 97, 98, 99, 100, 1, 101]. This morphology consists of domains whose characteristic sizes facilitates high exciton diffusion to the interface, fairly large interfacial area that enhances exciton dissociation, as well as straight pathways that promote charge transport. This intuition has been backed by various numerical investigations [3, 83, 13, 79, 47] which compare planar and bulk-heterojunction (BHJ) morphologies with columnar morphologies and make the case for columnar morphologies. Alam et. al. [83] even suggested that no significant gains in performance of BHJ devices may be expected through morphology modification as the numerically calculated efficiency of annealed BHJ devices is already close to devices with the 'optimal' columnar morphology.

We investigate the underlying hypothesis in all these studies that columnar morphology

leads to optimal performance by exploring other structured morphologies. Since the exploration of all arbitrary morphologies is conceptually infeasible, we start from a 'standard' columnar morphology and make systematic topological perturbations to this morphology. Specifically, we perturb the donor-acceptor interface into a sine function $x = Asin(2\pi yk)$, where y is the distance from the top boundary, and x is the interface location. This creates a family of fully-connected, interdigitated 'wavy' columnar morphologies characterized by two parameters: amplitude (A) and wavenumber (k) (Fig. 5.1). Using the sine function also ensures that the total donor-acceptor volume fraction in the active layer is conserved, all domains remain connected to the electrodes, and the domain characteristic sizes remain nearly constant (Fig. 5.1). We evaluate the performance of this family of morphologies by calculating the current-voltage characteristics under 1 sun condition using the excitonic drift-diffusion model [3, 83, 13, 79] with material properties A.1 corresponding to widely studied model system with 1:1 volume ratio of poly(3-hexylthiophene) as donor and [6,6]-phenyl-C_{61}-butyric acid-methyl ester as acceptor (P3HT:PCBM).

Parameter	Symbol	Numerical value	Units
Electron effective density of states	N_C	3.5×10^{25}	m^{-3}
Hole effective density of states	N_V	3.5×10^{25}	m^{-3}
Electron mobility	μ_n	2.5×10^{-7}	$m^2V^{-1}s^{-1}$
Hole mobility	μ_p	1.5×10^{-7}	$m^2V^{-1}s^{-1}$
Band gap	E_g	1.34	eV
Relative dielectric constant	ϵ	3.4	$--$
Average exciton lifetime	τ_X	1×10^{-6}	s
Electron-hole pair distance	a	1.8×10^{-9}	m
Active layer thickness	L	100	nm

Table 5.1: Material parameters used for simulating 'Wavy' morphologies

Fig. 5.2 plots the current-voltage characteristics of three morphologies: a representative bulk-heterojunction morphology, columnar morphology and a representative topological perturbation. The efficiency of each device is a function of the short-circuit current J_{sc}, open-circuit voltage V_{oc} and fill-factor FF. Changes to the V_{oc} and FF are usually negligible when modifying the morphology of a device while keeping the materials, volume fraction and electrode

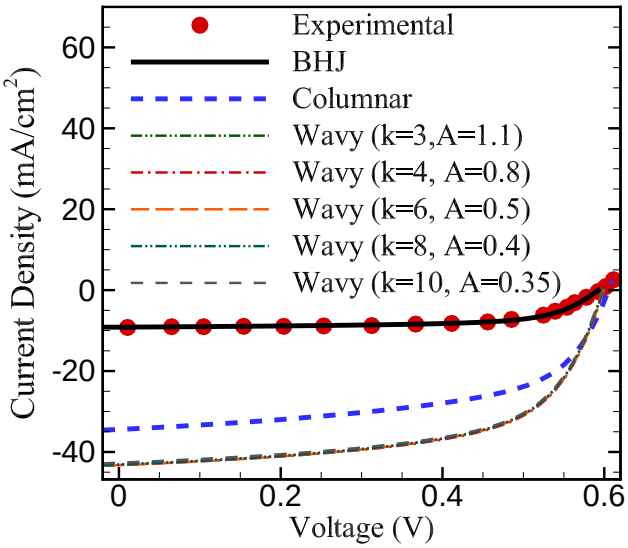

Figure 5.2: Current voltage curves for three morphologies: A representative BHJ morphology whose predicted profile matches experimentally measured values, a 'standard' columnar morphology, and a typical member of the 'wavy' columnar morphology

connectivity invariant (as seen in Fig. 5.2, also [83]). Based on this, we focus on using J_{sc} as the metric for performance comparisons [1]. The J_{sc} for a large set of morphologies corresponding to variations in A from 0.05 to 2.0 and variations in k from 1 to 10 was computed [2].

5.2 Results and discussion

Fig. 5.3 shows variations of the normalized short-circuit current $\tilde{J}_{sc}$ with changing A and k starting from a 'standard' columnar morphology with columns of width 10 nm. $\tilde{J}_{sc}$ is obtained by dividing the short-circuit current computed for a perturbed morphology with the short-circuit current of the 'standard' columnar morphology. For $k = 1$, $\tilde{J}_{sc}$ increases monotonically with increase in amplitude A. For higher values of wavenumber k, $\tilde{J}_{sc}$ initially increases and then decreases. The peak value of $\tilde{J}_{sc}$ for each constant-k curve is nearly identical ($\sim 125\%$ of the 'standard' columnar morphology). Furthermore, these peaks occur on the loci of constant

[1] We utilize our in-house parallel finite element based simulation framework [79] for solving the EDD equations and computing the current-voltage characteristics. Solving for each current-voltage plot requires significant computational effort on a high performance computing cluster

[2] We developed an in-house automation framework that intelligently deploys and tracks each parallel FEM calculation and enables compressive management of large number of simulations. The complete high throughput analysis of the family of morphologies required about 7000 hours of computing.

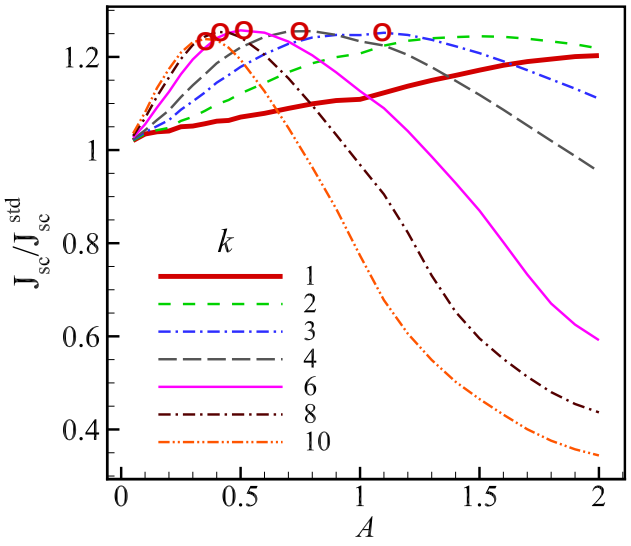

Figure 5.3: Variation of normalized short-circuit current J'_{sc} for a family of 'wavy' morphologies that are topological perturbations of a 'standard' columnar morphology of column width 10 nm.

$k * A$. We attribute the initial rise to the increase in donor-acceptor interface area and hence enhanced exciton dissociation. But any further increase in A is accompanied by a reduction of domain width (see Fig. 5.1). Smaller domain could result in larger non-geminate recombination, and hence, poorer charge transport [102] as shown by drop in $\tilde{J}_{sc}$. This increasing-decreasing behaviour of $\tilde{J}_{sc}$ corroborates well with observation by Shah and Ganesan [13]. The observation of peak $\tilde{J}_{sc}$ occurring at constant $k * A$ suggests that the net effect of increase in both A and k is to increase the donor-acceptor interface area. We assert that 'wavy' morphologies with the same interface area should result in similar $\tilde{J}_{sc}$ even when obtained by topological perturbations of 'standard' morphologies having different column widths.

We test this assertion by analyzing three families of 'wavy' morphologies obtained from three different column widths (10nm, 13.3nm, 20nm). Fig. 5.4 plots the computed J_{sc} purely as a function of the donor-acceptor interface area. All three data sets collapse into a single curve. The curve exhibits three linear regimes, marked as R1, R2, and R3. R1 is due to the exciton dissociation rate being directly proportional to interface area. The drop in short circuit current shown by R2 may be due to the linear decrease in the volume occupied by pure donor

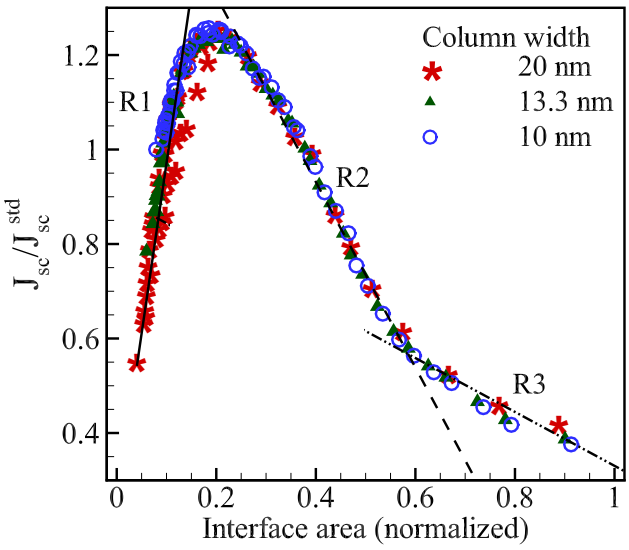

Figure 5.4: Relation between J_{sc} and donor-acceptor interface area. Both are normalized by the J_{sc} and interface-area of a 'standard' columnar morphology with column width of 10nm

and acceptor phases (and hence the charge transport pathways) with increasing interface area. The reduced slope of drop in region R3 could be explained by exhaustion of pure donor and acceptor phases thereby causing less change in short circuit current with increased interface area. The maxima in Fig. 5.4, which is almost identical for morphologies with different column widths, represents a balance between increase in exciton dissociation due to increase in interface area and decrease in charge transport pathways [13].

This – seemingly obvious – observation gives a structured approach to change the morphology so as to enhance the performance of OSCs: increasing the donor-acceptor interface area marginally while ensuring that (a) the total donor-acceptor volume fraction is conserved, (b) all domains remain connected to (appropriate) electrodes, (c) the domain characteristic sizes remain nearly constant. *Our results show that an interdigitated columnar structure is not optimal, and that improvements in performance can be obtained by perturbing this structure.* This has major implications in organic photovoltaics, as significant effort has gone towards achieving a columnar morphology. Fabricating nano-columnar structures is currently still a formidable challenge [103]. However, devices with micro-scale columnar morphologies are relatively straightforward to fabricate [96, 104, 105, 106]. Our results suggest a way to enhance

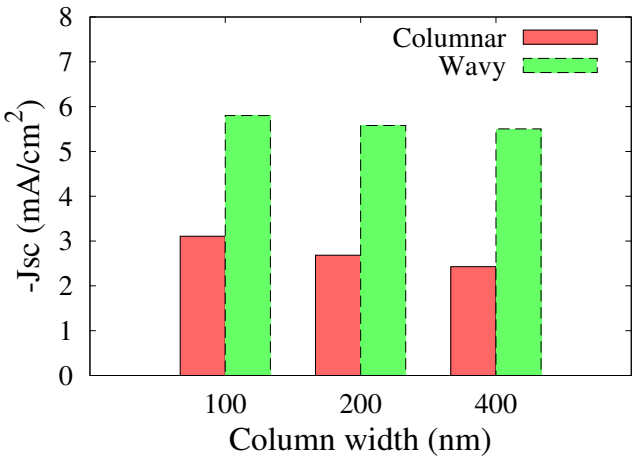

Figure 5.5: Columnar versus wavy morphologies with micro-scale columns

the (usually very poor) performance of such micro-columnar structures by inducing waviness. Waviness can be produced in a variety of ways, for instance, by mechanical deformations via wrinkling in the vertical directions using corona discharge as shown in [107] or via force induced buckling as shown in [108] and references therein. Fig. 5.5 plots the improvement in J_{sc} when waviness is introduced in devices with (sub) micron-scale columnar morphologies. The waviness decreases the average domain size and ensures that excitons are able to reach the donor-acceptor interface to create useful charges. This effect produces a nearly 100% improvement in J_{sc} for a range of column thicknesses.

CHAPTER 6. GENERAL CONCLUSIONS

6.1 General Discussion

An efficient, scalable and dimensionally independent computational framework has been developed which is able to use images of realistic morphologies obtained from TEM, SEM or AFM measurements. This framework enables visualization of the distribution of exciton densities, charge densities, potential and current densities in three dimensional heterogeneous morphology. It also enables differentiation of devices based on performance with different morphologies.

As discussed in chapter four, we presented a detailed analysis of the sensitivity of final electrode current density to material properties (electron/hole mobility, dielectric constant), device thickness and illumination intensity for (a) Bulk-heterojunction, (b) Sawtooth, and (c) Bilayer morphologies. The electrode current was found to be most sensitive to device thickness and illumination intensity. Investigation was performed for the question, if a device with sawtooth morphology is optimum of high efficiency. Wavy morphologies obtained through topological perturbations of columnar (sawtooth) morphologies – while qualitatively maintaining the connectivity to electrodes – give higher performance for certain values of amplitude (A) and wavenumber (k).

6.2 Recommendations for future Research

(1) **Optical simulation of heterogeneous morphologies**. A detailed comparative investigation of effect of bulk-heterojunction, bilayer, columnar and wavy morphologies on photon absorption would influence the morphology enhancement process which is currently focused on maximizing charge generation and transport.

2 **High fidelity OSC simulation**. Incorporation of extra phases in the donor:acceptor active layer blend – as revealed with recent imaging measurements – in the simulation process would increase the fidelity of the numerical results.

3 **Automated device thickness optimization**. Currently, the standard practice for experimentalists is to fabricate a number of devices with different thickness for the same materials and fabrication steps in order to determine the optimum thickness. A computational approach using an optimization framework along with the current framework for OSC simulation would automate and accelerate this process of determining optimum thicknesses.

APPENDIX A. Supplementary material for Chapter 2

A.1 Recombination strength, γ

As the electrons and holes are confined to different phases of the blend, the recombination occurs largely across the material interfaces. Braun [109] first proposed the form of the expression for recombination strength as

$$\gamma = \frac{q}{<\epsilon>} <\mu_n + \mu_p> \tag{A.1}$$

where <> denotes spatial average, to account for the difference in electron and hole mobilities in different components of the blend. A significant deviation was observed in the experimental values for the recombination coefficient [110]. Later the rate of recombination was suggested to be limited by the slowest charge carrier [111].

$$\gamma = \frac{q}{<\epsilon>} min(\mu_n, \mu_p) \tag{A.2}$$

Szmytkowski [112] considered the difference in permittivities of the two materials at the interface. He proposed a model taking the image force effects on the recombination into account.

$$\gamma = \left|\frac{\epsilon_1 - \epsilon_2}{\epsilon_1 + \epsilon_2}\right| \frac{e\mu_1}{\epsilon_0 \epsilon_1} \tag{A.3}$$

Although all three models have been implemented in the present framework, we present results using the simple model given by equation (A.1)

Table. A.1 tabulates the numerical values for the various constants used in this paper.

Parameter	Symbol	Numerical value	Units
Electron effective density of states	N_C	2.5×10^{25}	m^{-3}
Hole effective density of states	N_V	2.5×10^{25}	m^{-3}
Electron zero field mobility	μ_n	2.5×10^{-7}	$m^2V^{-1}s^{-1}$
Hole zero-field mobility	μ_p	3.0×10^{-8}	$m^2V^{-1}s^{-1}$
Band gap	E_g	1.34	eV
Generation rate	G	2.7×10^{27}	$m^{-3}s^{-1}$
Dielectric constant	$\langle\epsilon\rangle$	3.0×10^{-11}	F/m
Boltzmann constant	k_B	$1.3806503 \times 10^{-23}$	$m^2kgs^{-2}K^{-1}$
Room Temperature	T	300	K
Elementary charge	q	$1.60217646 \times 10^{-19}$	As

Table A.1: Parameters used for analysis of charge transport in OSCs

A.2 Newton's Method

Newton's method is a coupled procedure for solving the equations simultaneously. The equations (3.20-3.22) can be written in the residual form as

$$F_\phi(\phi, n, p) = 0 \quad F_n(\phi, n, p) = 0 \quad F_p(\phi, n, p) = 0 \tag{A.4}$$

Applying Taylor expansion on each of the three equations gives the following Jacobian system

$$\begin{bmatrix} \frac{\partial F_\phi}{\partial \phi} & \frac{\partial F_\phi}{\partial n} & \frac{\partial F_\phi}{\partial p} \\ \frac{\partial F_n}{\partial \phi} & \frac{\partial F_n}{\partial n} & \frac{\partial F_n}{\partial p} \\ \frac{\partial F_p}{\partial \phi} & \frac{\partial F_p}{\partial n} & \frac{\partial F_p}{\partial p} \end{bmatrix} \begin{vmatrix} \delta\phi \\ \delta n \\ \delta p \end{vmatrix} = - \begin{pmatrix} F_\phi \\ F_n \\ F_p \end{pmatrix}$$

which is solved for the corrections $\delta\phi$, δn and δp. The solution variables ϕ,n and p are then updated by

$$\begin{aligned} \phi(k+1) &= \phi(k) + \delta\phi(k) \\ n(k+1) &= n(k) + \delta n(k) \\ p(k+1) &= p(k) + \delta p(k) \end{aligned} \tag{A.5}$$

where k indicates the iteration number.

Elements of the Jacobian matrix in Newton's method

$$\begin{aligned}
\frac{\partial F_\phi}{\partial \phi} &= \int_\Omega -\lambda^2 \nabla \delta\phi \cdot \nabla w d\Omega \\
\frac{\partial F_\phi}{\partial n} &= \int_\Omega -w\delta n d\Omega \\
\frac{\partial F_\phi}{\partial p} &= \int_\Omega w\delta p d\Omega
\end{aligned}$$

$$\begin{aligned}
\frac{\partial F_n}{\partial \phi} &= \int_\Omega \left(n\nabla\delta\phi \cdot \nabla w\right) d\Omega - \sum_e \int_{\Omega_e} \nabla n \cdot \nabla\delta\phi[\tau_n \nabla\phi^h \cdot \nabla w_n^h] d\Omega \\
\frac{\partial F_n}{\partial n} &= \int_\Omega \left(\nabla\phi \cdot \nabla w\delta n - \nabla\delta n \cdot \nabla w\right) d\Omega - \sum_e \int_{\Omega_e} \nabla\delta n \cdot \nabla\phi[\tau_n \nabla\phi^h \cdot \nabla w_n^h] d\Omega \\
\frac{\partial F_n}{\partial p} &= 0
\end{aligned}$$

$$\begin{aligned}
\frac{\partial F_p}{\partial \phi} &= \int_\Omega \left(p\nabla\delta\phi \cdot \nabla w\right) d\Omega + \sum_e \int_{\Omega_e} \nabla p \cdot \nabla\delta\phi[\tau_p \nabla\phi^h \cdot \nabla w_p^h] d\Omega \\
\frac{\partial F_p}{\partial n} &= 0 \\
\frac{\partial F_p}{\partial p} &= \int_\Omega \left(\nabla\phi \cdot \nabla w\delta p + \nabla\delta p \cdot \nabla w\right) d\Omega + \sum_e \int_{\Omega_e} \nabla\delta p \cdot \nabla\phi[\tau_p \nabla\phi^h \cdot \nabla w_p^h] d\Omega
\end{aligned}$$

A.3 Probability of electron-hole pair dissociation

Onsager first described the dissociation and recombination kinetics of ion pairs in an applied electric field. This model of geminate recombination was later extended by Braun [109] by introducing the effect of finite lifetimes of electron-hole pairs. In Braun's model, electron-hole pair dissociation probability is given by

$$p(x, F, T) = \frac{k_d(x, F, T)}{k_d(x, F, T) + k_r} \tag{A.6}$$

where x is the electron-hole pair distance, F is the electric field strength, T is the temperature, k_r is the decay rate and k_d is the dissociation rate given by

$$k_d(x, F, T) = \frac{3\gamma}{4\pi x^3} e^{-E_b/K_B T} \frac{J_1(2\sqrt{-2b})}{\sqrt{-2b}} \tag{A.7}$$

In this expression $E_b = q^2/(4\pi\epsilon x)$ is the exciton binding energy, $b = q^3F/(8\pi\epsilon K_B^2T^2)$ is the field parameter and J_1 is the first order Bessel function given by

$$\frac{J_1(2\sqrt{-2b})}{\sqrt{-2b}} = \sum_{m=0}^{\infty} \frac{(2b)^m}{m!(m+1)!} \tag{A.8}$$

Electron-hole pair dissociation probability over all charge-separation distances is

$$P(F,T) = \frac{4}{\sqrt{\pi}a^3} \int_0^{\infty} p(x,F,T)x^2 e^{-(x/a)^2} dx \tag{A.9}$$

where a is the charge-separation distance at which the probability of the Gaussian function is maximum. This expression is evaluated numerically using Simpson's $3/8^{th}$ integration rule. The value of the integrands after first 200 terms drops down significantly and can be safely neglected.

A.4 Analytical solution for the simplified drift-diffusion equations

We consider a 1-D domain with homogeneous material properties at short-circuit conditions. We also consider constant charge generation. This enables us to assume a linear potential distribution across the electrodes [41]. Using these assumptions while neglecting recombination gives a linear uncoupled set of ordinary differential equations

$$\begin{aligned} \nabla.(-n\mu_n\nabla\phi + D_n\nabla n) &= G \\ \nabla.(p\mu_p\nabla\phi + D_p\nabla p) &= G \\ \nabla^2\phi &= 0 \end{aligned} \tag{A.10}$$

which can be solved analytically.

In one dimension the uncoupled electron and hole equations are of the form

$$\begin{aligned} D\frac{d^2\theta}{dx^2} + u\frac{d\theta}{dx} &= G \\ \theta(0) = \theta_1, \theta(d1) &= \theta_2 \end{aligned}$$

where θ is n—p and D and u are the coefficients of diffusion and drift term respectively(D = D_n—D_p, $u = -\mu_n\frac{d\phi}{dx}$—$\mu_p\frac{d\phi}{dx}$). This is a non homogeneous linear ODE. Solution to the corresponding homogeneous equation is given by,

$$\theta_h(x) = c_1 + c_2e^{-\frac{u}{D}x}$$

and the particular solution is,

$$\theta_p(x) = \frac{G}{u}x$$

General solution is,

$$\theta(\mathrm{x}) = \theta_h(x) + \theta_p(x) = c_1 + c_2 e^{-\frac{u}{D}x} + \frac{G}{u}x$$

Applying boundary conditions, we get,

$$\theta(\mathrm{x}) = \theta_1 - (\theta_1 - \theta_2 + \frac{G}{u}x_2)\frac{(1 - e^{-\frac{u}{D}x})}{(1 - e^{-\frac{u}{D}x_2})} + \frac{G}{u}x$$

This is the analytical solution for the uncoupled problem.

Derivative of θ, required for current calculation, is given by

$$\frac{d\theta}{dx} = -\frac{(\theta_1 - \theta_2 + \frac{G}{u}x_2)}{(1 - exp(-\frac{u}{D}x_2))}(\frac{u}{D}exp(-\frac{u}{D}x)) + \frac{G}{u}$$

APPENDIX B. Supplementary material for Chapter 3

B.1 Material parameters and universal constants [1, 2, 3, 4, 5]

Parameter	Symbol	Numerical value	Units
Electron effective density of states	N_C	2.5×10^{25}	m^{-3}
Hole effective density of states	N_V	2.5×10^{25}	m^{-3}
Electron zero field mobility	μ_n	2.5×10^{-7}	$m^2V^{-1}s^{-1}$
Hole zero-field mobility	μ_p	3.0×10^{-8}	$m^2V^{-1}s^{-1}$
Band gap	E_g	1.34	eV
Photon flux	Γ_0	4.31×10^{21}	$m^{-2}s^{-1}$
Donor relative dielectric constant	ϵ_D	6.5	$--$
Acceptor relative dielectric constant	ϵ_A	3.9	$--$
Absorption coefficient	α_0	2×10^7	m^{-1}
Average exciton lifetime	τ_X	1×10^{-6}	s
Boltzmann constant	k_B	$1.3806503 \times 10^{-23}$	$m^2kgs^{-2}K^{-1}$
Room Temperature	T	300	K
Elementary charge	q	$1.60217646 \times 10^{-19}$	As

Table B.1: Sample parameters used for simulation excitonic drift-diffusion equations

The typical parameters and universal constants used in the simulations described here are summarized in Table. B.1. The material properties are typical for annealed P3HT:PCBM based devices. The short-circuit current is highly dependent on the values of charge mobilities $\mu_n and \mu_p$. It also depends on overall exciton generation rate which is inturn dependent on the values of photon flux Γ_0, absorption coefficient α_0 and exciton lifetime τ_X. As the boundary condition for electrostatic potential ϕ is a function of band-gap, the open-circuit voltage V_{OC} is in turn highly dependent on band-gap E_g.

APPENDIX C. Supplementary material for Chapter 4

C.1 Sensitivity of Jsc to parameters P for bilayer, BHJ and sawtooth structures

Figures. C.1, C.2 and C.3 show the sensitivity of J_{sc} to P for bilayer, sawtooth and BHJ morphologies respectively. For regular structures – bilayer and sawtooth – the J_{sc} is most sensitive to device thickness for most of the parameter values considered. Whereas in case of BHJ structure, J_{sc} is more to illumination intensity than device thickness. This is expected as the distribution of the donor phase in the active layer region within the absorption depth governs the exciton generation rate. This donor phase distribution does not change for regular structured devices. $\delta_{\mu_n} J_{sc}$ is observed to be larger than $\delta_{\mu_p} J_{sc}$ for all three device structures, but the difference between $\delta_{\mu_n} J_{sc}$ and $\delta_{\mu_p} J_{sc}$ is larger of BHJ compared to sawtooth, which is in-turn larger than bilayer structure.

Detailed procedure for sensitivity calculation

Initially representative morphologies (Bilayer, Sawtooth and BHJ) are selected. Then we choose the input parameters μ_n,μ_p,ϵ_A,ϵ_D,L and Γ on which the sensitivity of the selected output parameter J_{sc} is calculated. A set of representative values is selected for the input parameters. Each of the input six parameters is investigated over a range at eight discrete values. The first value is from the representative values shown in Table. 4.1. Hence, in stage we have one case with values from Table. 4.1 and seven cases (for seven discrete values) for each the six input parameters, with a total of 43 cases. This is the phase space of parameter values at which sensitivity is calculated.

To calculate the sensitivity each of the six parameters is varied by 10% resulting in 258

simulations for each morphology. The sensitivity of the short circuit current is calculated by taking the difference between the values of short circuit current obtained at the 43 cases and the ones obtained with the input parameters varied by 10%. Thus, the sensitivities to each input parameter is determined for a range of parameter values.

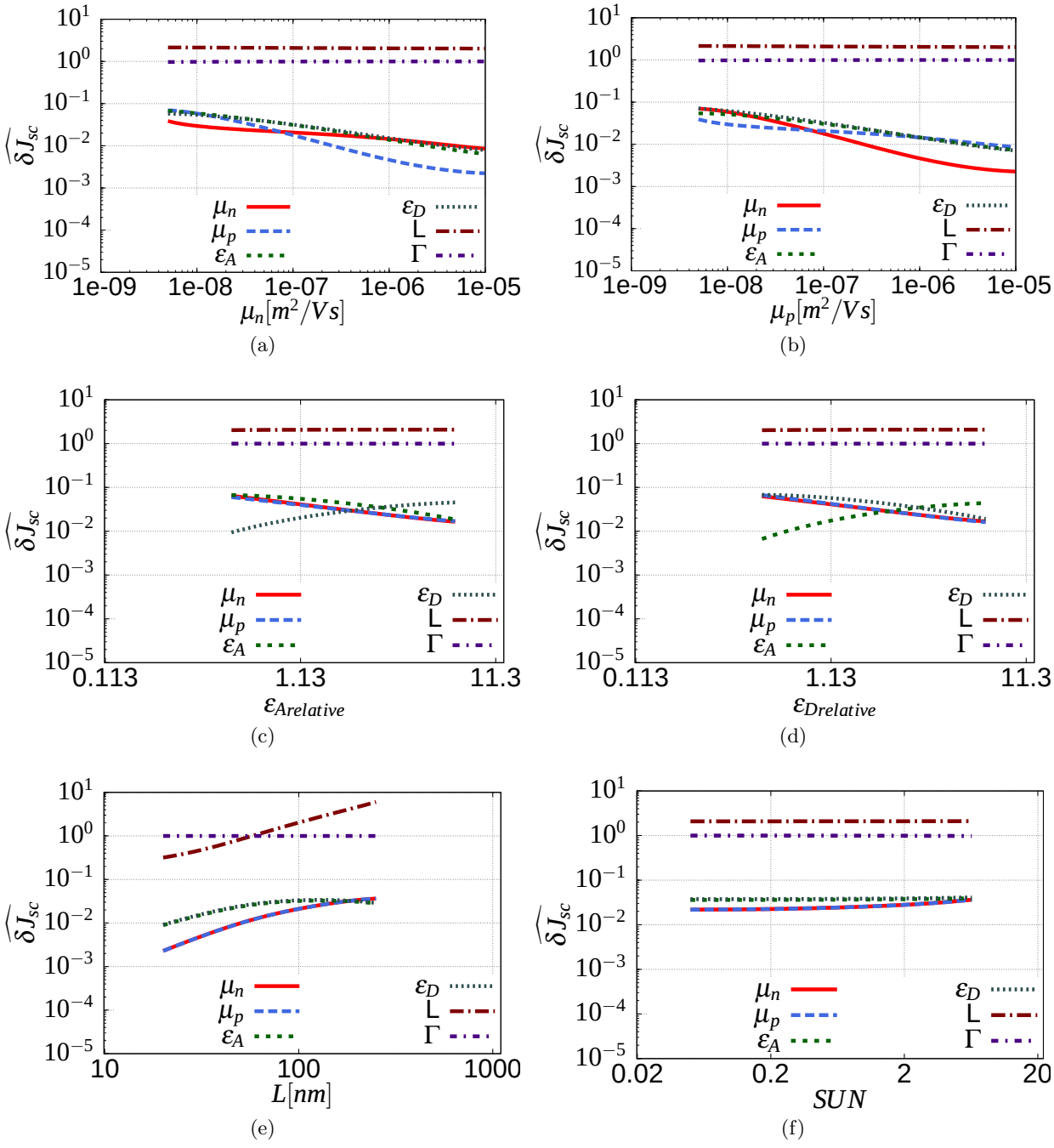

Figure C.1: Sensitivity of Jsc to different parameters over a range of (a) μ_n, (b) ϵ_A, (c) L, and (d) Γ (in terms of number of Suns) for bilayer morphology

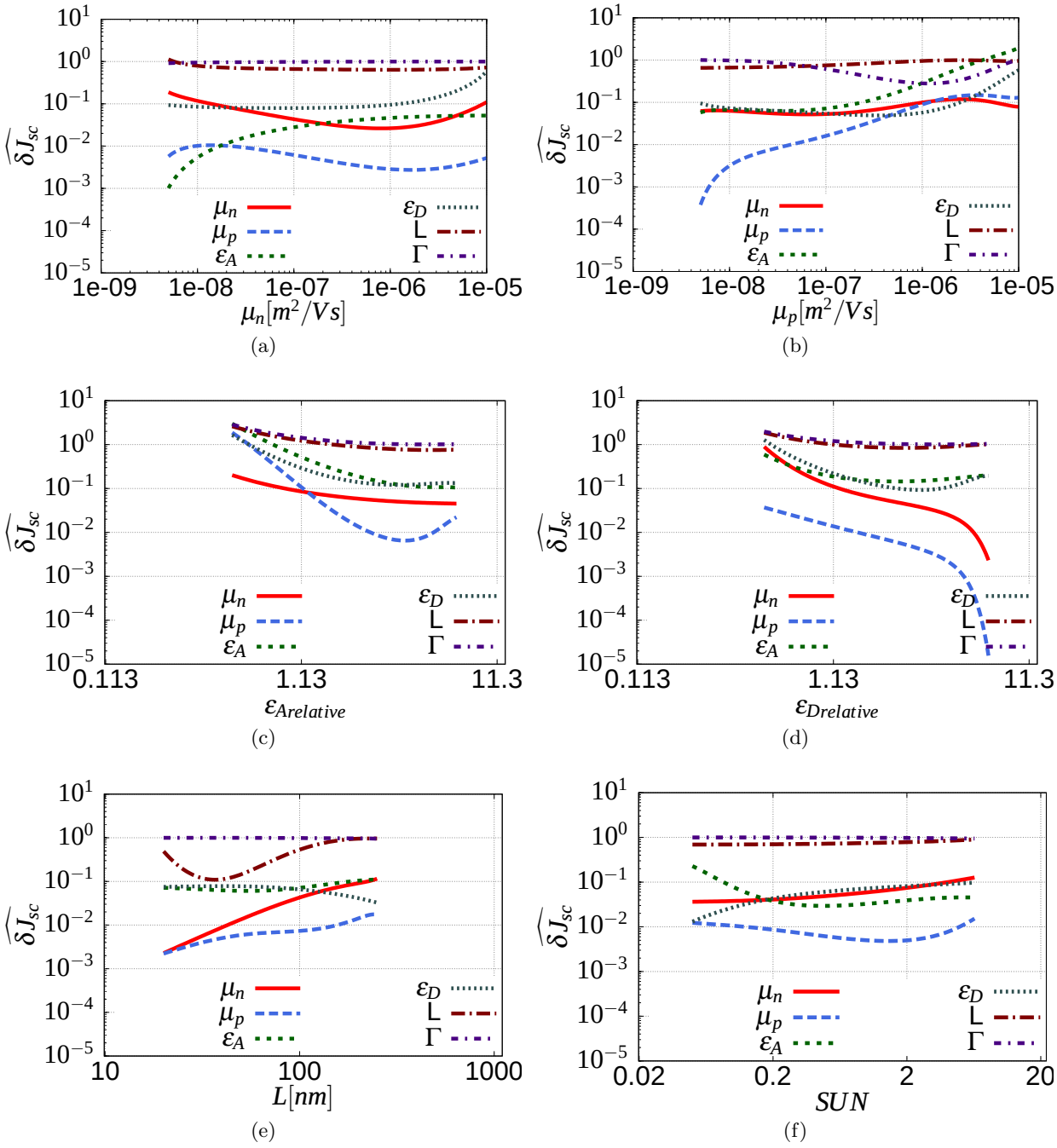

Figure C.2: Sensitivity of Jsc to different parameters over a range of (a) μ_n, (b) ϵ_A, (c) L, and (d) Γ (in terms of number of Suns) for BHJ morphology

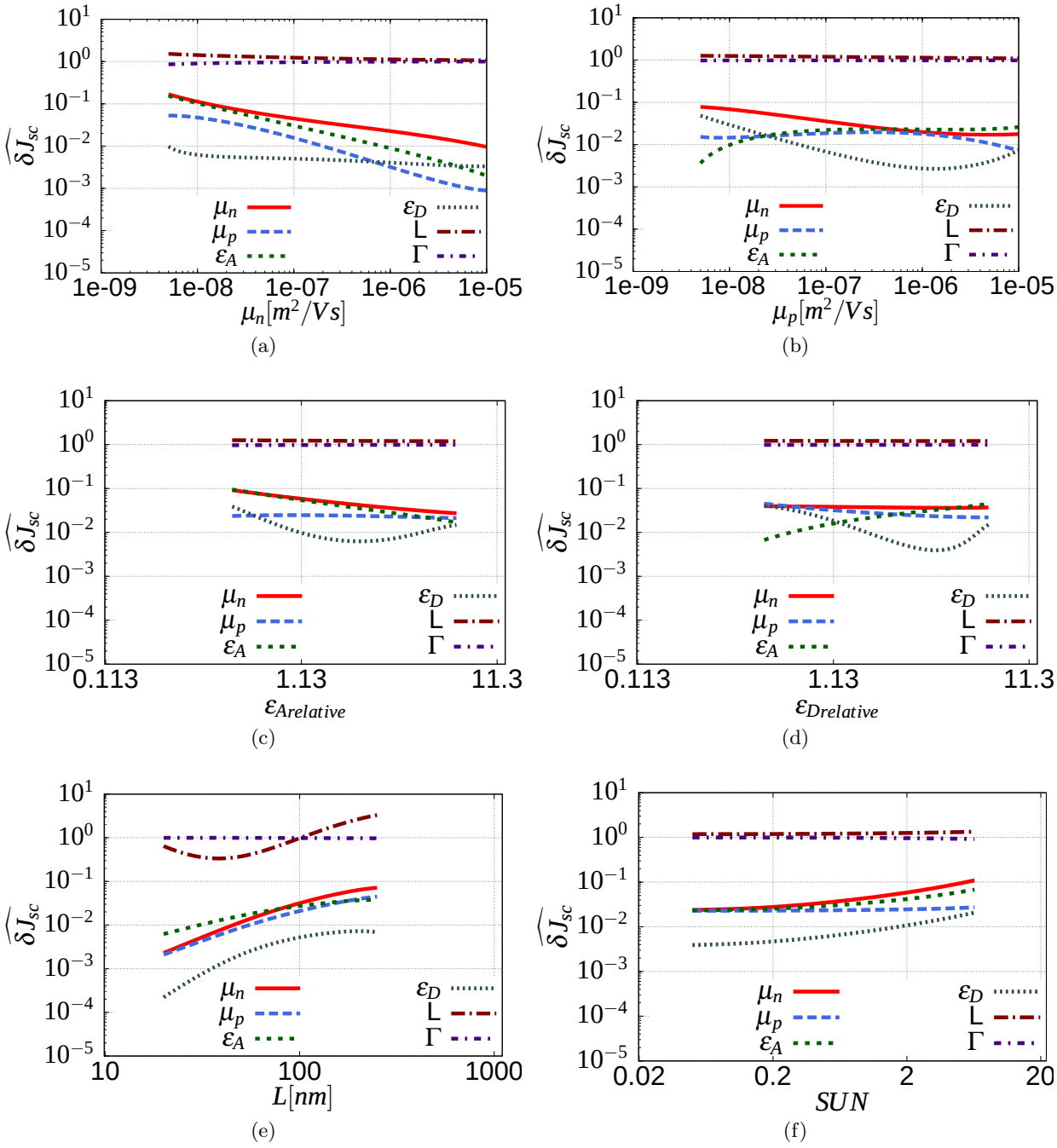

Figure C.3: Sensitivity of Jsc to different parameters over a range of (a) μ_n, (b) ϵ_A, (c) L, and (d) Γ (in terms of number of Suns) for sawtooth morphology

BIBLIOGRAPHY

[1] Y. Yang. High-efficiency solution processable self-organization of polymer blends. *Group*, 4(November):2–6, 2005.

[2] L. J. A. Koster, V. D. Mihailetchi, and P. W. M. Blom. Bimolecular recombination in polymer/fullerene bulk heterojunction solar cells. *Applied Physics Letters*, 88(5):052104, 2006.

[3] G. A. Buxton and N. Clarke. Computer simulation of polymer solar cells. *Modelling and Simulation in Materials Science and Engineering*, 13, 2007.

[4] G. Dennler, M. C. Scharber, and C. J. Brabec. Polymer-Fullerene Bulk-Heterojunction Solar Cells. *Advanced Materials*, 21(13):1323–1338, April 2009.

[5] M. Estrada, A. Cerdeira, I. Mejia, M. Avila, R. Picos, L.F. Marsal, J. Pallares, and B. Iñiguez. Modeling the behavior of charge carrier mobility with temperature in thin-film polymeric transistors. *Microelectronic Engineering*, (July):1–6, July 2010.

[6] J. S. Moon, J. K. Lee, S. Cho, J. Byun, and A. J. Heeger. "Columnlike" structure of the cross-sectional morphology of bulk heterojunction materials. *Nano letters*, 9(1):230–4, January 2009.

[7] Veronique S Gevaerts, L Jan Anton Koster, Martijn M Wienk, and Rene a J Janssen. Discriminating between Bilayer and Bulk Heterojunction Polymer:Fullerene Solar Cells Using the External Quantum Efficiency. *ACS applied materials & interfaces*, pages 12–15, August 2011.

[8] Renewables projected to overtake natural gas as world's second-largest power source. http://www.theverge.com/2013/6/28/4473694/

iea-says-renewable-energy-overtakes-natural-gas-nuclear-by-2016. Accessed on the 03 July 2013.

[9] J. Barker, C. Ramsdale, and N. Greenham. Modeling the current-voltage characteristics of bilayer polymer photovoltaic devices. *Physical Review B*, 67(7):1–9, February 2003.

[10] G. Buxton and N. Clarke. Predicting structure and property relations in polymeric photovoltaic devices. *Physical Review B*, 74(8):1–5, August 2006.

[11] C. M. Martin, V. M. Burlakov, H. E. Assender, and D. A. R. Barkhouse. A numerical model for explaining the role of the interface morphology in composite solar cells. *Journal of Applied Physics*, 102(10):104506, 2007.

[12] J. Williams and A. B. Walker. Two-dimensional simulations of bulk heterojunction solar cell characteristics. *Nanotechnology*, 19(42):424011, October 2008.

[13] M. Shah and V. Ganesan. Correlations between Morphologies and Photovoltaic Properties of RodCoil Block Copolymers. *Macromolecules*, 43(1):543–552, January 2010.

[14] Kanwar S. Nalwa, Hari K. Kodali, Baskar Ganapathysubramanian, and Sumit Chaudhary. Dependence of recombination mechanisms and strength on processing conditions in polymer solar cells. *Applied Physics Letters*, 99(26):263301, 2011.

[15] Kanwar S. Nalwa, John A. Carr, Rakesh C. Mahadevapuram, Hari K. Kodali, Sayantan Bose, Yuqing Chen, Jacob W. Petrich, Baskar Ganapathysubramanian, and Sumit Chaudhary. Enhanced charge separation in organic photovoltaic films doped with ferroelectric dipoles. *Energy Environ. Sci.*, 5:7042–7049, 2012.

[16] Solarmer Energy, Inc. Breaks Psychological Barrier with 8.13 % OPV Efficiency. www.solarmer.com, accessed on the 19 November 2010, 2010.

[17] C. J. Brabec, N. S. Sariciftci, and J. C. Hummelen. Plastic Solar Cells. *Advanced Functional Materials*, 11(1):15–26, February 2001.

[18] W. Y. Wong, X. Z. Wang, Z. He, K. K. Chan, A. B. Djuriic, K. Y. Cheung, C. T. Yip, A. M. C. Ng, Y. Y. Xi, C. S. K. Mak, and W. K. Chan. Tuning the Absorption, Charge Transport Properties, and Solar Cell Efficiency with the Number of Thienyl Rings in Platinum-Containing Poly(aryleneethynylene)s. *Journal of the American Chemical Society*, 129(46):14372–14380, 2007.

[19] Konarka Tech Sheets and Brochures. Konarka Power Plastic Market Overview. http://www.konarka.com, accessed on the 19 November 2010.

[20] F.C. Krebs. Fabrication and processing of polymer solar cells: A review of printing and coating techniques. *Solar Energy Materials and Solar Cells, Processing and Preparation of Polymer and Organic Solar Cells*, 93(4):394–412, 2009.

[21] O. Wodo and B. Ganapathysubramanian. Computationally efficient solution to the Cahn-Hilliard equation: adaptive implicit time schemes, mesh sensitivity analysis and the 3D isoperimetric problem. *Journal of Computational Physics*, preprint.

[22] M. Campoy-Quiles, T. Ferenczi, T. Agostinelli, P.G. Etchegoin, Y. Kim, T.D. Anthopoulos, P.N. Stavrinou, D.D.C. Btadley, and J. Nelson. Morphology evolution via self-organization and lateral and vertical diffusion in polymer:fullerene solar cell blends. *Nature Materials*, 7:158–164, 2008.

[23] C. W. Chu, H. Yang, W. J. Hou, J. Huang, G. Li, and Y. Yang. Control of the nanoscale crystallinity and phase separation in polymer solar cells. *Applied Physics Letters*, 92(10):103306, 2008.

[24] J. Jo, S. S. Kim, S. I. Na, B. K. Yu, and D. Y. Kim. Time-dependent morphology evolution by annealing processes on polymer:fullerene blend solar cells. *Advanced Functional Materials*, 19:866–874, 2009.

[25] Y. Kim, A. M. Ballantyne, J. Nelson, and D.D.C. Bradley. Effects of thickness and thermal annealing of the PEDOT:PSS layer on the performance of polymer solar cells. *Organic Electronics*, 10(1):205–209, 2009.

[26] H. Hoppe and N. S. Sariciftci. Morphology of polymer/fullerene bulk heterojunction solar cells. *Journal of Materials Chemistry*, 16(1):45, 2006.

[27] W. Ma, C. Yang, X. Gong, K. Lee, and A.J. Heeger. Thermally stable, efficient polymer solar cells with nanoscale control of the interpenetrating network morphology. *Advanced Functional Materials*, 15:1617–1622, 2005.

[28] C. Deibel, V. Dyakonov, and C. J. Brabec. Organic Bulk-Heterojunction Solar Cells. *IEEE Journal of Selected Topics in Quantum Electronics*, pages 1–11, 2010.

[29] S. E. Shaheen, C. J. Brabec, and N. S. Sariciftci. 2.5% efficient organic plastic solar cells. *Applied Physics Letters*, 78:841–843, 2001.

[30] Y. Liang, D. Feng, Y. Wu, S. T. Tsai, G. Li, C. Ray, and L. Yu. Highly efficient solar cell polymers developed via fine-tuning of structural and electronic properties. *Journal of the American Chemical Society*, 131(22):7792–7799, 2009.

[31] Z. Wu, B. Fan, F. Xue, C. Adachi, and J. Ouyang. Organic molecules based on dithienyl-2,1,3- benzothiadiazole as new donor materials for solution-processed organic photovoltaic cells. *Solar Energy Materials and Solar Cells*, (In Press, Corrected Proof:), 2010.

[32] Y. He, H. Y. Chen, J. Hou, and Y. Li. Indene-C60 bisadduct:: A new acceptor for high-performance polymer solar cells. *Journal of the American Chemical Society*, 132(4):1377–1382, 2010.

[33] S. K. Hau, H. L. Yip, J. Zou, and A. K. Y. Jen. Indium tin oxide-free semi-transparent inverted polymer solar cells using conducting polymer as both bottom and top electrodes. *Organic Electronics*, 10(7):1401–1407, 2009.

[34] M. S. White, D. C. Olson, S. E. Shaheen, N. Kopidakis, and D. S. Ginley. Inverted bulk-heterojunction organic photovoltaic device using a solution-derived zno underlayer. *Applied Physics Letters*, 89(14):143–517, 2006.

[35] D. Cheyns, B. P. Rand, and P. Heremans. Organic tandem solar cells with complementary absorbing layers and a high open-circuit voltage. *Applied Physics Letters*, 97(3):033301, 2010.

[36] L. Chen, Z. Hong, G. Li, and Y. Yang. Recent progress in polymer solar cells: Manipulation of polymer:fullerene morphology and the formation of efficient inverted polymer solar cells. *Advanced Materials*, 21:1434–1449, 2009.

[37] J. Peet, A. J. Heeger, and G. C. Bazan. "Plastic" solar cells: self-assembly of bulk heterojunction nanomaterials by spontaneous phase separation. *Accounts of Chemical Research*, 42(11):1700–8, November 2009.

[38] C. Groves, O. G. Reid, and D. S. Ginger. Heterogeneity in polymer solar cells: Local morphology and performance in organic photovoltaics studied with scanning probe microscopy. *Accounts of Chemical Research*, 43(5):612–620, 2010. PMID: 20143815.

[39] S. H. Park, A. Roy, S. Beaupre, S. Cho, N. Coates, J. S.Moon, D. Moses, M. Leclerc, K. Lee, and A. J. Heeger. Bulk heterojunction solar cells with internal quantum efficiency approaching 100%. *Nature Photonics*, 3:297–303, 2009.

[40] J. Peet, J. Y. Kim, N. E. Coates, W. L. Ma, D. Moses, A. J. Heeger, and G. C. Bazan. Efficiency enhancement in low-bandgap polymer solar cells by processing with alkane dithiols. *Nature Materials*, 6:497–500, 2007.

[41] L. J. A. Koster, V. D. Mihailetchi, and P. W. M. Blom. Device model for the operation of polymer/fullerene bulk heterojunction solar cells. *Physical Review B*, 72(8):1–9, August 2005.

[42] H. K. Kodali and B. Ganapathysubramanian. A virtual framework for investigating the effect of 3D morphology on charge generation and transport in organic thin film devices. *Journal of Computational Physics*, preprint.

[43] I. W. Hwang, D. Moses, and A. J. Heeger. Photoinduced carrier gener- ation in P3HT/PCBM bulk heterojunction materials. *Journal of Physical Chemistry C*, 112:4350–4354, 2008.

[44] E. V. Emelianova, M. van der Auweraer, and H. Bssler. Hopping approach towards exciton dissociation in conjugated polymers. *Journal of Chemical Physics*, 128:224709–1224709–8, 2008.

[45] P. K. Watkins, A. B. Walker, and G. L. B. Verschoor. Dynamical Monte Carlo Modelling of Organic Solar Cells: The Dependence of Internal Quantum Efficiency on Morphology. *Nano Letters*, 5(9):1814–1818, 2005.

[46] R. A. Marsh, C. Groves, and N. C. Greenham. A microscopic model for the behaviour of nanostructured organic photovoltaic devices. *Journal of Applied Physics*, 101:083509, 2007.

[47] C. R. McNeill, S. Westenhoff, C. Groves, R. H. Friend, and N. C. Greenham. Influence of Nanoscale Phase Separation on the Charge Generation Dynamics and Photovoltaic Performance of Conjugated Polymer Blends:Balancing Charge Generation and Separation. *Journal of Physical Chemistry C*, 111(51):19153–19160, 2007.

[48] C. Groves, R. A. Marsh, and N. C. Greenham. Monte Carlo modeling of geminate recombination in polymer-polymer photovoltaic devices. *The Journal of Chemical Physics*, 129(11):114903, September 2008.

[49] C. Groves, R. G. E. Kimber, and A. B. Walker. Simulation of loss mechanisms in organic solar cells: A description of the mesoscopic Monte Carlo technique and an evaluation of the first reaction method. *The Journal of Chemical Physics*, 133(14):144110, 2010.

[50] F. Assad, K. Banoo, and M. Lundstrom. The drift-diffusion equation revisited. *Solid-State Electronics*, 42(3):283–295, 1998.

[51] Peter Stallinga. *Two-Terminal Devices: DC Current, Electrical Characterization of Organic Electronic Materials and Devices*, pages 45–64. John Wiley & Sons, Ltd, 2009.

[52] S. Selberherr. *Analysis and simulation of semiconductor devices*. Springer-Verlag Wien-New York, 1984.

[53] V. D. Mihailetchi, J. K. J. van Duren, P. W. M. Blom, J. C. Hummelen, R. A. J. Janssen, J. M. Kroon, M. T. Rispens, W. J. H. Verhees, and M. M. Wienk. Electron Transport in a Methanofullerene. *Advanced Functional Materials*, 13:43–46, 2003.

[54] C. Melzer, E. Koop, V. D. Mihailetchi, , and P. W. M. Blom. Hole Transport in Poly(phenylene vinylene)/Methanofullerene Bulk-Heterojunction Solar Cells. *Advanced Functional Materials*, 14(9):865–870, 2004.

[55] P. A. Markowich, C. A. Ringhofer, E. Langer, and S. Selberherr. An asymptotic analysis of single-junction semiconductor devices. Report 2527, University of Wisconsin, 1983.

[56] A. N. Brooks and T. J. R. Hughes. Streamline upwind/petrov- galerkin formulations for convection dominated flows with particular emphasis on the incompressible navier-stokes equation. *Computer Methods in Applied Mechanics and Engineering*, 32:199–259, 1982.

[57] R.E. Bank, W.M. Coughran, and L.C. Cowsar. Analysis of the finite volume Scharfetter-Gummel method for steady convection diffusion equations. *Computing and Visualization in Science*, 1(3):123–136, 1998.

[58] E. Gatti, S. Micheletti, and R. Sacco. A new Galerkin framework for the drift-diffusion equation in semiconductors. *East West Journal of Numerical Mathematics*, 6(2):101–135, 1998.

[59] J. Xu and L. Zikatanov. A monotone finite element scheme for convection-diffusion equations. *Mathematics of Computation*, 68(228):1429–1446, 1999.

[60] R. Lazarov and L. Zikatanov. An exponential fitting scheme for general convection diffusion equations on tetrahedral meshes. *Computational Applied Mathematics*, 1(92):60–69, 2005.

[61] H. K. Gummel and D. L. Scharfetter. Large-signal analysis of a silicon read diode oscillator. *IEEE Transactions on Electronic Devices*, ED-16:64–77, 1969.

[62] F. Brezzi, L. Marini, and P. Pietra. Numerical simulation of semiconductor devices. *Computational Methods in Applied Mechanics and Engineering*, 75:493–514, 1989.

[63] M. Sharma and G. F. Carey. Semiconductor device simulation using daptive refinement and flux upwinding. *IEEE Transactions on Computer-Aided Design*, 8(6):590–598, 1989.

[64] S. Balay, W. D. Gropp, L. C. McInnes, and B. F. Smith. *Efficient management of parallelism in object-oriented numerical software libraries*, pages 163–202. Birkhauser Boston Inc., Cambridge, MA, USA, 1997.

[65] G. Karypis and V. Kumar. Metis - unstructured graph partitioning and sparse matrix ordering system, version 4.0. Technical report, University of Minnesota, Minneapolis, MN, 2009.

[66] P. R. Amestoy, I. S. Duff, J. Koster, and J. Y. L'Excellent. A fully asynchronous multifrontal solver using distributed dynamic scheduling. *SIAM Journal of Matrix Analysis and Applications*, 23(1):15–41, 2001.

[67] J.S. Moon, J.K. Lee, S. Cho, J. Byun, and A.J. Heeger. "Columnlike" structure of the cross-sectional morphology of bulk heterojunction materials. *Nano Letters*, 9:230, 2009.

[68] P. Vanlaeke, A. Swinnen, I. Haeldermans, G. Vanhoyland, T. Aernouts, D. Cheyns, C. Deibel, J. Dhaen, P. Heremans, and J. Poortmans. P3HT/PCBM bulk heterojunction solar cells: Relation between morphology and electro-optical characteristics. *Solar Energy Materials and Solar Cells*, 90(14):2150–2158, September 2006.

[69] H. K. Kodali and B. Ganapathysubramanian. A computational framework to investigate charge transport in heterogeneous organic photovoltaic devices. *Computer Methods in Applied Mechanics and Engineering*, submitted.

[70] V. D. Mihailetchi, H. Xie, B. de Boer, L. M. Popescu, J. C. Hummelen, P. W. M. Blom, and L. J. A. Koster. Origin of the enhanced performance in poly(3-hexylthiophene): [6,6]-phenyl C[sub 61]-butyric acid methyl ester solar cells upon slow drying of the active layer. *Applied Physics Letters*, 89(1):012107, 2006.

[71] A. Mayer, S. Scully, B. Hardin, M. Rowell, and M. Mcgehee. Polymer-based solar cells. *Materials Today*, 10(11):28–33, November 2007.

[72] George F. Burkhard, Eric T. Hoke, Shawn R. Scully, and Michael D. McGehee. Incomplete exciton harvesting from fullerenes in bulk heterojunction solar cells. *Nano Letters*, 9(12):4037–4041, 2009. PMID: 19810728.

[73] L. J. A. Koster, V. D. Mihailetchi, and P. W. M. Blom. Ultimate efficiency of polymer/fullerene bulk heterojunction solar cells. *Applied Physics Letters*, 88(9):093511, 2006.

[74] G. Li, Y. Yao, H. Yang, V. Shrotriya, G. Yang, and Y. Yang. Solvent Annealing Effect in Polymer Solar Cells Based on Poly(3-hexylthiophene) and Methanofullerenes. *Advanced Functional Materials*, 17(10):1636–1644, July 2007.

[75] O. Wodo and B. Ganapathysubramanian. Modeling morphology evolution during solvent-based fabrication of organic solar cells. *Computational Materials Science*, 55(0):113 – 126, 2012.

[76] H. K. Kodali and B. Ganapathysubramanian. Electrode contact engineering for improved charge transport in heterogeneous excitonic solar cells.

[77] Konarka technologies advances award winning power plastic solar cell efficiency with 9% certification. http://www.konarka.com/index.php/site/pressreleasedetail/konarka_technologies_advances_award_winning_power_plastic_solar_cell_efficiency_with_9_certificatio. Accessed on the Feb 28 November 2012.

[78] Patrick Boland, Keejoo Lee, and Gon Namkoong. Device optimization in PCPDTBT:PCBM plastic solar cells. *Solar Energy Materials and Solar Cells*, 94(5):915–920, May 2010.

[79] Hari K. Kodali and Baskar Ganapathysubramanian. Computer simulation of heterogeneous polymer photovoltaic devices. *Modelling and Simulation in Materials Science and Engineering*, 20(3):035015, 2012.

[80] O. Wodo, S. Tirthapura, S. Chaudhary, and B. Ganapathysubramanian. A novel graph based formulation for characterizing morphology with application to organic solar cells. *Organic Electronics*, accepted, arXiv:1106.3536v2.

[81] Kanwar S. Nalwa, John A. Carr, Rakesh C. Mahadevapuram, Hari K. Kodali, Sayantan Bose, Yuqing Chen, Jacob W. Petrich, Baskar Ganapathysubramanian, and Sumit Chaudhary. Enhanced charge separation in organic photovoltaic films doped with ferroelectric dipoles. *Energy & Environmental Science*, 2012.

[82] Kanwar S. Nalwa, Hari K. Kodali, Baskar Ganapathysubramanian, and Sumit Chaudhary. Dependence of recombination mechanisms and strength on processing conditions in polymer solar cells. *Applied Physics Letters*, 99(26):263–301, 2011.

[83] Biswajit Ray and Muhammad A. Alam. Random vs regularized OPV: Limits of performance gain of organic bulk heterojunction solar cells by morphology engineering. *Solar Energy Materials and Solar Cells*, 99:204–212, January 2012.

[84] J. Cariboni, D. Gatelli, R. Liska, and A. Saltelli. The role of sensitivity analysis in ecological modelling. *Ecological Modelling*, 203(12):167–182, 2007.

[85] Andrea Saltelli, Marco Ratto, Stefano Tarantola, and Francesca Campolongo. Sensitivity analysis for chemical models. *Chemical reviews*, 105(7):2811–28, July 2005.

[86] E.J. Haug, K.K. Choi, and V Komkov. *Design sensitivity analysis of structural systems*. 1986.

[87] Ivan A. Nestorov. Sensitivity analysis of pharmacokinetic and pharmacodynamic systems: I. a structural approach to sensitivity analysis of physiologically based pharmacokinetic models. *Journal of Pharmacokinetics and Pharmacodynamics*, 27:577–596, 1999. 10.1023/A:1020926525495.

[88] I. Y. Gejadze and G. J. M. Copeland. Adjoint sensitivity analysis for fluid flow with free surface. *International Journal for Numerical Methods in Fluids*, 47(8-9):1027–1034, 2005.

[89] R. Hausermann, E. Knapp, M. Moos, N. A. Reinke, T. Flatz, and B. Ruhstaller. Coupled optoelectronic simulation of organic bulk-heterojunction solar cells: Parameter extraction and sensitivity analysis. *Journal of Applied Physics*, 106(10):104507, 2009.

[90] A.L. Fahrenbruch and R.H. Bube. *Fundamentals of Solar Cells*. 1983.

[91] L.B. Schein, R.S. Narang, R.W. Anderson, K.E. Meyer, and A.R. McGhie. Electric-field-independent electron mobilities in anthracene. *Chemical Physics Letters*, 100(1):37 – 40, 1983.

[92] Veaceslav Coropceanu, Jrme Cornil, Demetrio A. da Silva Filho, Yoann Olivier, Robert Silbey, and Jean-Luc Brdas. Charge transport in organic semiconductors. *Chemical Reviews*, 107(4):926–952, 2007.

[93] Hari K. Kodali and Baskar Ganapathysubramanian. A computational framework to investigate charge transport in heterogeneous organic photovoltaic devices. *Computer Methods in Applied Mechanics and Engineering*, submitted.

[94] Gang Li, Rui Zhu, and Yang Yang. Polymer solar cells. *Nature Photonics*, 6(3):153–161, February 2012.

[95] M. C. Scharber and N. S. Sariciftci. Efficiency of bulk-heterojunction organic solar cells. *Progress in Polymer Science*, in press, 2013.

[96] Yutaka Matsuo, Yoshiharu Sato, Takaaki Niinomi, Iwao Soga, Hideyuki Tanaka, and Eiichi Nakamura. Columnar structure in bulk heterojunction in solution-processable three-layered p-i-n organic photovoltaic devices using tetrabenzoporphyrin precursor and silylmethyl[60]fullerene. *Journal of the American Chemical Society*, 131(44):16048–16050, 2009. PMID: 19886695.

[97] Michael Graetzel, René a J Janssen, David B Mitzi, and Edward H Sargent. Materials interface engineering for solution-processed photovoltaics. *Nature*, 488(7411):304–12, August 2012.

[98] J. Xue, B.P. Rand, S. Uchida, and S.R. Forrest. A hybrid planarmixed molecular heterojunction photovoltaic cell. *Advanced Materials*, 17(1):66–71, 2005.

[99] M Campoy-Quiles, T Ferenczi, T Agostinelli, P G Etchegoin, Y Kim, T D Anthopoulos, P N Stavrinou, D D C Btadley, and J Nelson. Morphology evolution via self-organization and lateral and vertical diffusion in polymer:fullerene solar cell blends. *Nature Materials*, 7(February):158–164, 2008.

[100] Youngkyoo Kim, Steffan Cook, Sachetan M. Tuladhar, Stelios a. Choulis, Jenny Nelson, James R. Durrant, Donal D. C. Bradley, Mark Giles, Iain McCulloch, Chang-Sik Ha, and Moonhor Ree. A strong regioregularity effect in self-organizing conjugated polymer films and high-efficiency polythiophene:fullerene solar cells. *Nature Materials*, 5(3):197–203, February 2006.

[101] L. Schmidt-Mende, A. Fechtenktter, K. Mllen, E. Moons, R. H. Friend, and J. D. MacKenzie. Self-organized discotic liquid crystals for high-efficiency organic photovoltaics. *Science*, 293(5532):1119–1122, 2001.

[102] B. Lei, Y. Yao, A. Kumar, Y. Yang, and V. Ozolins.

[103] Ziyang Hu, Jianjun Zhang, and Ying Zhao. Efficient polymer solar cells based on light-trapping transparent electrodes. *Applied Physics Letters*, 100(10):103303, 2012.

[104] Taeyong Kim, Hyunsik Yoon, Hyung-Jun Song, Niko Haberkorn, Younghyun Cho, Seung Hyun Sung, Chang Hee Lee, Kookheon Char, and Patrick Theato. Toward mass producible ordered bulk heterojunction organic photovoltaic devices. *Macromolecular Rapid Communications*, 33(23):2035–2040, 2012.

[105] Dian Chen, Wei Zhao, and Thomas P. Russell. P3ht nanopillars for organic photovoltaic devices nanoimprinted by aao templates. *ACS Nano*, 6(2):1479–1485, 2012.

[106] Jianchen Hu, Yasuhiro Shirai, Liyuan Han, and Yutaka Wakayama. Template method for fabricating interdigitate p-n heterojunction for organic solar cell. *Nanoscale research letters*, 7(1):1–5, January 2012.

[107] Soong Ju Oh, Cherie R Kagan, Jong Bok Kim, Pilnam Kim, Nicolas C Pe, Jason W Fleischer, Howard A Stone, and Yueh-lin Loo. Wrinkles and deep folds as photonic structures in photovoltaics. *Nature Photonics*, 6(April):327–332, 2012.

[108] Z. Xu and B. Hu. Photovoltaic Processes of Singlet and Triplet Excited States in Organic Solar Cells. *Advanced Functional Materials*, 18(17):2611–2617, September 2008.

[109] C. L. Braun. Electric field assisted dissociation of charge transfer states as a mechanism of photocarrier production. *Journal of Chemical Physics*, 80:41–57, 1984.

[110] A. Pivrikas, G. Juska, A. J. Mozer, M. Scharber, K. Arlauskas, N. S. Sariciftci, H. Stubb, and R. Österbacka. Bimolecular Recombination Coefficient as a Sensitive Testing Parameter for Low-Mobility Solar-Cell Materials. *Physical Review Letters*, 94:176–806, 2005.

[111] L. J. A. Koster, V. D. Mihailetchi, and P. W. M. Blom. Bimolecular recombination in polymer/fullerene bulk heterojunction solar cells. *Applied Physics Letters*, 88(5):052104, 2006.

[112] J. Szmytkowski. Modeling the electrical characteristics of P3HT:PCBM bulk heterojunction solar cells: Implementing the interface recombination. *Semiconductor Science and Technology*, 25(1):015009, January 2010.